ABSTRACT

Title of dissertation: A Breath of Fresh Air: Study of Reactive Porous Metal Oxides for Chemical Warfare Agent and Simulant Defeat

Matthew Bigler Leonard, Doctor of Philosophy, 2023

Dissertation directed by: Professor Efrain E. Rodriguez
Department of Chemistry and Biochemistry

Organophosphorus molecules are a wide class of compounds that are used commercially as fire retardants, plasticizers, and pesticides. Organophosphorus pesticides were developed to replace environmentally persistent pesticides, such as dichlorodiphenyltrichloroethane, more commonly known as DDT. However, organophosphorus pesticides have been proven to be carcinogenic and to affect neurodevelopment negatively. A sub-class of organophosphorus molecules are highly toxic acetylcholinesterase (AChE) inhibitors, known as nerve agents. Although the Geneva convention banned the use of chemical warfare agents (CWA), the nerve agent sarin has been used as recently as 2013 on Syrian civilians. In 2018, a Novichok nerve agent was used in the attempted assassination of a former Russian spy and his daughter. Current CWA respiratory protection employs bituminous coal (BPL), carbon which is impregnated with a mixture known as ASZM-TEDA. BPL carbon impregnated with ASZM-TEDA has a wide range of reactivity, but has not changed significantly since its inception. The next-generation filtration material will need to have a large surface area to maximize reactive sites and be robust to withstand degradation. Mesoporous and nanoparticle metal oxides are highly active materials that show promise in nerve agent defeat.

Within this dissertation, the goal is to develop and study reactive metal oxides to understand the

factors that are important for the decomposition of CWAs and CWA simulants. In Chapter 1, I introduce the history of CWAs, the downfalls of current filtration technology, and the candidates for the next generation filter. In Chapter 2, the methods and characterization techniques used within this work are presented and discussed. In Chapter 3, to determine the effects of cation selection on methyl paraoxon decomposition, Ce^{4+} was isovalently doped into anatase type TiO_2. Through UV/Vis spectroscopy, the degradation of methyl paraoxon was tracked and fit to pseudo-first-order kinetics, then normalized to the synthesized material's surface area. The rate constant, normalized to the material's surface area (k_{SA}), reveals CeO_2 is 3 to 4.6 times larger than that of TiO_2 and the Ce-doped titanias. The Ce-doped titanias showed little to no change in methyl paraoxon decomposition compared to TiO_2. The lack of change within the Ce-dopant titania revealed that crystal structure is a larger driving factor for methyl paraoxon decomposition than the cation identity (i.e. Ce^{4+} and Ti^{4+}).

Chapter 4 presents a study on the gas surface interaction between sarin and dry CuO nanoparticles (NP) through infrared (IR) spectroscopy. Sarin adsorbs to CuO through the P=O bond, and proceeds to decompose on the surface. Distinct red shifts in the δ_s(P-CH_3) and ρ(P-CH_3) modes indicate the cleavage of the P-F bond, producing isopropyl methyl phosphonic acid (IMPA). Concurrently, a mode attributed to ν_s(O-P-O) begins to grow in, demonstrating that sarin forms a bridging species on the surface. Sarin continues to degrade on the dry CuO surface once the sarin feed is removed. Upon heating above 423 K, all modes associated with IMPA simultaneously decrease, indicating that IMPA desorbs from the surface. These observations were further corroborated through computational methods.

Finally, in Chapter 5, I seek to enhance the reactivity of CuO by placing the cation Cu^{2+} within a Jahn-Teller active geometry. Mesoporous NiO and Cu-doped NiO were synthesized and exposed to diisopropyl fluorophosphate (DFP) in different environments and studied through diffuse reflectance IR Fourier transform spectroscopy (DRIFTS). Ordered mesoporous Cu-doped NiO was successfully synthesized through a hard templating method. Through X-ray diffraction (XRD),

Cu^{2+} was incorporated into the NiO rock-salt lattice without phase separation for $\leq$ 20%. The mesoporous metal oxides (MMO) maintained high surface areas (67.89-94.38 m^2/g), with the main pore size $\sim$2.4 nm. Shifts in the Raman spectra indicate the dopant, Cu^{2+}, reduces nickel vacancies resulting in a decrease in Ni^{3+} defect states. Upon DFP exposure, NiO was highly oxidative producing CO, CO_2, carbonyls, and carbonates due to the active oxygen species formed by the Ni^{2+} vacancies. The mesoporous Cu-doped NiO samples were less reactive to DFP oxidation, due to the Cu^{2+} occupying the nickel vacancies, resulting in a reduction of active oxygen species.

A Breath of Fresh Air: Study of Reactive Porous Metal Oxides for Chemical Warfare Agent and Simulant Defeat

by

Matthew Bigler Leonard

Dissertation submitted to the Faculty of the Graduate School of the
University of Maryland, College Park in partial fulfillment
of the requirements for the degree of
Doctor of Philosophy
2023

Advisory Committee:
Professor Efrain E. Rodriguez, Chair/Advisor
Professor Eric Wachsman, Dean's Representative
Professor John T. Fourkas
Professor Leah G. Dodson
Professor Mercedes Taylor

© Copyright by
Matthew Bigler Leonard
2023

Dedication

This work is dedicated to my friends and family who have served or are still serving in the military. Along with the Warfighters and first responders who put on the uniform every day to protect our freedoms.

Acknowledgments

Completing a Ph.D. is not done alone, it requires the support of a variety of people. I have been lucky to be surrounded by friends and mentors who have supported me throughout this process. I'd first like to thank Dr. John Fourkas, Dr. Leah Dodson, Dr. Mercedes Taylor, Dr. Amy Mullin, Dr. Sang Bok Lee, Dr. Jeff Davis and Dr. Eric Wachsman for serving on my seminar, candidacy, and/or my dissertation committee. Providing guidance, and advice throughout the last 4 years.

I'd like to thank Dr. Efrain Rodriguez for his mentorship and help to develop me into the scientist I am today. This includes the whole Rodriguez group during my time at UMD. Every person provided help within or outside the lab to hone my technical and scientific skills. In particular, my project partner Tianyu Li, who introduced me to mesoporous materials and challenged my scientific knowledge throughout this process.

I was lucky to have joined the Graduate program with a group of very intelligent individuals who consistently helped each other out and ensured everyone had the chance to succeed. This includes Morgan Kramer, Charlotte Wentz, Michael Hitt, Lahari Balisetty, Medha Rath, Siddharth Singh, Robert Martin, Jason Tran, Delaney DiMaggio, and Justin Yu. I'd like to thank Shannon McDonnell and Tim Diethrich who were close personal friends who helped me work through the different hurdles in graduate school.

The surface science team at the chemical biological center (CBC) honestly took a chance when hiring me as a postdoc. Working at CBC for the last nine months has accelerated my knowledge of the chemical filtration field more than I could have imagined. This could not have been done without the mentorship of the entire team, Dr. Erin Durke, Dr. Wes Gordon, Dr. Jason Navin, Dr. Monica McEntee, and Dr. Chris Karwacki.

Of course, I'd like to thank my wife Jamie Leonard who supported me throughout this process. Allowing me to spend all those nights and weekends working instead of spending time with you. To my puppies, Max and Peppa for providing emotional support during the stressful parts of graduate

school. Finally, thank you to my parents Jon and Saralyn Leonard, who taught me the value of hard work and to follow my dreams.

Table of Contents

Dedication ii

Acknowledgements iii

Table of Contents v

List of Figures viii

List of Tables xi

List of Abbreviations xii

1 Introduction and Background 1
- 1.1 Brief History of Chemical Warfare Agents . . . 1
- 1.2 Chemical Warfare Agent Protection . . . 3
- 1.3 Organophosphorus CWAs and their Simulants . . . 5
- 1.4 Next-Generation Filtration Materials . . . 8
  - 1.4.1 Metal Organic Frameworks (MOFs) . . . 9
  - 1.4.2 Zeolites . . . 10
- 1.5 Decomposition of Organophosphorus Molecules on Metal Oxides . . . 11
  - 1.5.1 Titanium (TiO_2) and Cerium Oxide (CeO_2) . . . 14
  - 1.5.2 Copper Oxide (CuO) . . . 16
  - 1.5.3 Nickel Oxide (NiO) and Copper doped NiO . . . 17

2 Materials and Techniques 18
- 2.1 Materials . . . 18
  - 2.1.1 Nanoparticles . . . 18
  - 2.1.2 Order Mesoporous Materials . . . 20
- 2.2 Characterization Techniques . . . 23
  - 2.2.1 Nitrogen Adsorption . . . 23
  - 2.2.2 X-ray Diffraction (XRD) . . . 26

2.2.3 Electron Microscopy . . . 27
Transmission Electron Microscopy (TEM) . . . 28
Scanning Electron Microscopy (SEM) . . . 28
Electron-dispersive X-ray Spectroscopy (EDS) . . . 29
2.2.4 Ultraviolet-Visible Absorption Spectroscopy (UV/Vis) . . . 29
2.2.5 Infrared Spectroscopy (IR) . . . 29
In-Situ DRIFTS Set Up . . . 35
Mid-Infrared Aerosol Chemistry Chamber (MIRACC) . . . 36

3 Spectroscopic Studies of Methyl Paraoxon Decomposition over Mesoporous Ce-doped Titanias for Toxic Chemical Filtration 39
3.1 Introduction . . . 39
3.2 Experimental Section . . . 42
3.2.1 Synthesis of Mesoporous TiO_2 and Ce-doped TiO_2 . . . 42
3.2.2 Synthesis of Mesoporous CeO_2 . . . 42
3.2.3 Bulk and Surface Characterization . . . 43
3.2.4 Methyl Paraoxon Testing Procedures . . . 44
3.2.5 UV-Vis Absorption Measurements . . . 44
3.2.6 *Ex-situ* DRIFTS measurements . . . 45
3.2.7 Mass Spectrometry . . . 45
3.3 Results and Discussion . . . 46
3.3.1 Bulk characterization . . . 46
3.3.2 Surface characterization . . . 48
3.3.3 Methyl Paraoxon Decomposition . . . 51
3.4 Conclusion . . . 59

4 Experimental Study of the Adsorption and Decomposition of Sarin on Dry Copper (II) Oxide 60
4.1 Introduction . . . 60
4.2 Experimental Section . . . 61
4.2.1 Material Characterization . . . 61
4.2.2 Experimental IR Procedures . . . 62
4.3 Results . . . 63
4.3.1 Material Characterization . . . 63
4.3.2 Adsorption and Decomposition of Sarin on Dry CuO Nanoparticles . . . 63
4.3.3 Decomposition of Sarin on Dry CuO Nanoparticles Post Purge . . . 68
4.4 Discussion . . . 72
4.5 Conclusion . . . 74

5 Low Temperature Combustion of Nerve Agent Simulant on Mesoporous Nickel Oxide and Cu-Doped Nickel Oxide 75
5.1 Introduction . . . 75
5.2 Experimental . . . 78

5.2.1 Synthesis of Mesoporous NiO and Cu-Doped NiO . . . 78
5.2.2 DFP *in-situ* Diffuse Reflectance Infrared Fourier Transform Spectroscopy (DRIFTS) Measurements . . . 79
5.3 Results and Discussion . . . 80
5.3.1 Material Characterization . . . 80
5.3.2 Adsorption and Decomposition of DFP On NiO in O_2-Rich and O_2-Free atmospheres. . . . 87
5.3.3 Adsorption and Decomposition of DFP on NiO-250 and $Cu_xNi_{1-x}O$-250 ($x = 0.1, 0.2$) in an O_2-Rich atmosphere. . . . 93
5.3.4 Low Temperature Dosing . . . 95
5.3.5 Effects of the Pretreatment Temperature . . . 96
5.3.6 Proposed Decomposition Pathway . . . 98
5.3.7 Soman Decomposition . . . 101
5.4 Conclusion . . . 101

6 Conclusion 103
6.1 Future Work . . . 105
6.2 Moving Forward . . . 106

Bibliography 108

7 Appendix: Supplemental Figures 123
7.1 Chapter 3 . . . 123
7.2 Chapter 4 . . . 131
7.3 Chapter 5 . . . 132
7.3.1 Materials . . . 132
7.3.2 Bulk and Surface Characterization . . . 132

List of Figures

1.1 Timeline of historical applications of toxic chemicals . . . 2
1.2 Timeline of select gas masks used throughout history . . . 4
1.3 Organophosphorus nerve agents: (a) sarin (GB), (b) soman (GD), (c) cyclosarin (GF), (d) tabun (GA). . . . 6
1.4 Organophosphorus simulants: (a) diisopropyl fluorophosphate (DFP), (b) dimethyl methylphosphonate (DMMP), (c) methyl paraoxon (DMNP). . . . 8
1.5 Commonly studied MOFs for CWA adsorption/decomposition . . . 10
1.6 General adsorption interactions with an organophosphorus molecule and a metal oxide surface. . . . 12
1.7 Acute toxicity of sarin and the common decomposition products . . . 13
1.8 Hydrolysis of methyl paraoxon and GB . . . 14
1.9 Dealkylation of GB and GD . . . 15

2.1 Nanoparticle size versus specific surface area . . . 19
2.2 Mesoporous synthesis techniques . . . 22
2.3 Example adsorption isotherms of Type I, II, and IV and mesoporous hysteresis . . . 24
2.4 Graphical representation of Braggs law. . . . 27
2.5 Example of the decomposition of methyl paraoxon producing 4-nitrophenol which under basic conditions absorbs strongly at 402 nm . . . 30
2.6 Representation of (a) the harmonic and anharmonic oscillator models and (b) common vibrational modes of chemical bonds . . . 32
2.7 Different experimental infrared spectroscopy methods . . . 33
2.8 Diffuse reflectance infrared Fourier transform spectroscopy (DRIFTS) diagram . . . 34
2.9 DRIFTS system and the PIKE accessory . . . 36
2.10 Mid-Infrared Aerosol Chemistry Chamber (MIRACC) . . . 37
2.11 Mid-Infrared Aerosol Chemistry Chamber (MIRACC) instrumental diagram and sample holder . . . 38

3.1 Chemical warfare agents Sarin and Soman compared to the simulant methyl paraoxon . . . 40
3.2 Powder X-ray diffraction patterns of TiO_2, $Ce_xTi_{1-x}O_2$ ($0.05 \leq x \leq 0.15$) and CeO_2 . . . 47
3.3 Transmission electron microscopy and diffraction patterns of TiO_2, $Ce_xTi_{1-x}O_2$ ($0.05 \leq x \leq 0.15$) and CeO_2 . . . 48

3.4 Small angle X-ray scattering (SAXS) data of TiO_2, $Ce_xTi_{1-x}O_2$ ($0.05 \leq x \leq 0.15$) and CeO_2 . . . 49
3.5 Nitrogen adsorption isotherms of TiO_2, $Ce_xTi_{1-x}O_2$ ($0.005 \leq x \leq 0.15$) and CeO_2 50
3.6 Pyridine adsorption on TiO_2, $Ce_xTi_{1-x}O_2$ ($0.05 \leq x \leq 0.15$) and CeO_2 . . . 52
3.7 a) Thermogravimetric analysis curve for TiO_2, $Ce_xTi_{1-x}O_2$ and CeO_2. b) Amount of weight loss divided by surface area . . . 53
3.8 Methyl paraoxon decomposition as (a) total percent decomposed and (b) Surface normalized per surface area . . . 55
3.9 *Ex situ* DRIFTS of the metal oxides after methyl paraoxon exposure . . . 57
3.10 Proposed pathways for the decomposition of methyl paraoxon on metal surface with hydroxyls and solvent . . . 58

4.1 Characterization of the CuO Nanoparticles. . . . 64
4.2 IR difference spectra of dry CuO nanoparticles exposed to GB over 1.75 h with a) raw IR spectrums and b) composite peak fitting spectrum . . . 65
4.3 Infrared spectrum of GB dosed on CuO Nanoparticles . . . 66
4.4 Infrared difference spectrum of CuO NP exposed to pyridine . . . 67
4.5 Infrared spectrum of GB on CuO post purge and prior to purge . . . 69
4.6 Proposed mechanism for the decomposition of sarin on dry CuO. . . . 70
4.7 Progression of the infrared spectrum of GB on CuO during heating . . . 71
4.8 Predicted relative energy profiles associated with GB decomposition on pristine CuO (111) . . . 73

5.1 (a) CWA simulant diisopropyl fluorophosphate (DFP), (b) diisopropyl methylphosphonate (DIMP), (c) CWA sarin and (d) soman. . . . 76
5.2 Illustration of an octahedral molecule with an electron configuration of d^9. The molecular orbitals break degeneracy, resulting in the lengthening of the axial bonds. 77
5.3 Graphical depiction of the synthesis of mesoporous $Cu_xNi_{1-x}O$. . . . 79
5.4 Powder X-ray diffraction patterns, lattice parameters and crystallite size of the synthesized MMOs, including NiO, $Cu_{0.1}Ni_{0.9}O$ and $Cu_{0.2}Ni_{0.8}O$. . . . 81
5.5 TEM and SEM images of synthesized MMOs, including NiO, $Cu_{0.1}Ni_{0.9}O$ and $Cu_{0.2}Ni_{0.8}O$. . . . 82
5.6 SAXS pattern of the synthesised NiO, $Cu_{0.1}Ni_{0.9}O$ and $Cu_{0.2}Ni_{0.8}O$ . . . 83
5.7 Nitrogen adsorption and pore size distribution of synthesized MMOs, including NiO, $Cu_{0.1}Ni_{0.9}O$ and $Cu_{0.2}Ni_{0.8}O$. . . . 84
5.8 Pyridine adsorption DRIFTS difference spectrum of NiO, $Cu_{0.1}Ni_{0.9}O$, $Cu_{0.2}Ni_{0.8}O$ and Sigma CuO Nanoparticles . . . 85
5.9 TGA curves for NiO, $Cu_{0.1}Ni_{0.9}O$ and $Cu_{0.2}Ni_{0.8}$ showing 10% dopant results in increased weight, which is likely due to additional hydroxyl groups that stabilize the surface. . . . 86
5.10 Raman spectra of NiO, $Cu_{0.1}Ni_{0.9}O$ and $Cu_{0.2}Ni_{0.8}O$ . . . 87
5.11 DRIFTS difference spectrum of NiO-250 ZA and NiO-250 He exposed to DFP for 2 hours . . . 88

5.12 Main decomposition peak tracking on NiO-250 ZA and NiO-250 He 92
5.13 DRIFTS difference spectrum of $Cu_{0.1}Ni_{0.9}O$-250 ZA and $Cu_{0.2}Ni_{0.8}O$-250 ZA exposed to DFP for 2 hours 94
5.14 Main decomposition peak tracking of NiO-250 ZA, $Cu_{0.1}Ni_{0.9}O$-250 ZA and $Cu_{0.2}Ni_{0.8}$-250 ZA 95
5.15 DRIFTS difference spectra of NiO-250 exposed to DFP at -50 °C 96
5.16 Surface Characterization of NiO-250 and NiO-500 97
5.17 DRIFTS difference spectra of NiO pretreated at 500 °C (NiO-500) exposed to DFP in ZA over 2 hours. 99
5.18 Main decomposition peak tracking of NiO-500 ZA compared to NiO-250 ZA . . 99
5.19 Proposed decomposition pathway of DFP on mesoporous NiO. 100

7.A1 DRIFTS spectra of MMOs exposed to 2-propanol then filtered and dried 123
7.A2 ATR FTIR spectrum of paraoxon with peaks 124
7.A3 ESI-MS for $Ce_{0.15}Ti_{0.85}O_2$ with paraoxon at a) 5 min and b) 4 h 126
7.A4 Time dependant UV/Vis absorption spectra of TiO_2, $Ce_xTi_{1-x}O_2$ and CeO_2 as paraoxon decomposes. 127
7.A5 Normalized paraoxon decomposition on TiO_2, $Ce_xTi_{1-x}O_2$, CeO_2 after 4 hours. . 128
7.A6 Image of samples TiO_2, $Ce_xTi_{1-x}O_2$, CeO_2. 128
7.A7 Decomposition of paraoxon on each metal oxide with calculated decomposition. . 130
7.A8 Infrared difference spectrum of CuO NP between clean CuO and CuO post GB exposure and heating 131
7.A9 Schematic of DRIFTS reactor. 133
7.A10 DRIFTS difference spectrum of NiO-250 ZA and NiO-250 He in the first 30 min of DFP exposure 133
7.A11 DRIFTS difference spectrum of Acetone adsorbed on NiO-250. 134
7.A12 *Ex-situ* exposure of diisopropyl methylphosphonate (DIMP) on NiO-250 134
7.A13 Main decomposition peak tracking of NiO-500 ZA compared to NiO-250 ZA . . 135

List of Tables

1.1 Composition of the ASZM-TEDA impregnants and its intended protection 5
1.2 Summarized physical properties of "G" series agents 7

3.1 Average crystallite size for the MMOs TiO_2, $Ce_xTi_{1-x}O_2$ and CeO_2 through Rietveld refinement using the Debye-Scherrer formula. 46
3.2 Consolidated table of values calculated from nitrogen adsorption 49
3.3 Methyl paraoxon decomposition (4-nitrophenol) as (a) total percent decomposed. As Ce-dopant increases, kinetics remains similar, but total reactivity increases with dopant. (b) Surface normalized per surface area, over time. CeO_2 is the most reactive, while TiO_2 and $Ce_xTi_{1-x}O_2$ (x = 0.5%, 5%, 10%) display little difference in their reactivity, unlike the x = 15 % sample total decomposition is boosted. . . . 55

4.1 Infrared spectrum modes for GB in liquid and vapor phase, IMPA in the liquid phase and GB on CuO 68

5.1 Consolidation of characteristics for NiO and $Cu_xNi_{1-x}O$ as obtained from nitrogen adsorption measurements. 83
5.2 The Raman shift peaks (cm^{-1}) and the associated full-width at half maximum (FWHM) for the fitted curves. The Ni^{3+}/Ni^{2+} are approximated ratios from the calculated peak area. 86
5.3 Infrared mode assignments (cm^{-1}) of DFP dosed on NiO-250 and NiO-500. 93

7.A1 EDS atomic percentages metal concentrations for $Ce_xTi_{1-x}O_2$. 124
7.A2 *Ex-situ* pyridine absorption peak frequencies with assigned sites. 129
7.A3 Peaks and assigned vibrations from *ex-situ* DRIFTS of each MMO with paraoxon and TiO_2 with 2-propanol in cm^{-1}. 129
7.A4 EDS atomic percentages metal concentrations for $Cu_xNi_{1-x}O_2$. 132

List of Abbreviations

AChE	Acetylcholinesterase
ATR	Attenuated Total Reflectance
$Ce_xTi_{1-x}O_2$	Cerium Doped Titanium Dioxide
CeO_2	Cerium Dioxide
ChE	Cholinesterase
CO	Carbon Monoxide
CO_2	Carbon Dioxide
$Cu_xNi_{1-x}O$	Copper Doped Nickel Oxide
CuO	Copper Oxide
CWA	Chemical Warfare Agent
DDT	Dichlorodiphenyltrichloroethane
DFP	Diisopropyl Fluorophosphate
DFT	Density Functional Theory
DIMP	Diisopropyl Methylphosphonate
DMMP	Dimethyl Methylphosphonate
DMNP (Methyl Paraoxon)	Dimethyl 4-Nitrophenol Phosphonate
DRIFTS	Diffuse Reflectance Infrared Fourier Transform Spectroscopy
EISA	Evaporation Induced Self Assembly
GB	Sarin
GD	Soman
HRMS	High Resolution Mass Spectroscopy
IMPA	Isopropyl Methyl Phosphonic Acid
IPA	Isopropyl Alcohol
IR	Infrared Spectroscopy
MIRACC	Mid Infrared Aerosol Chemistry Chamber
MMO	Mesoporous Metal Oxide
MPFA	Methylphosphonofluoridic Acid
MPA	Methyl Phosphonic Acid
N_2	Nitrogen
NiO	Nickel Oxide
O_2	Oxygen
RGA	Residual Gas Analyzer
SAXS	Small Angle X-Ray Scattering
SEM	Scanning Electron Microscopy
TEM	Transmission Electron Microscopy
TEOS	Tetraethyl Orthosilicate
TGA	Thermogravimetric Analysis
TiO_2	Titanium Dioxide
UV/Vis	Ultraviolet/Visible Spectroscopy
XRD	X-Ray Diffraction

Chapter 1: Introduction and Background

Professor Roscoe Dickinson was head of chemical wartime research at Caltech during WWII. When discussing the work with a graduate student, Professor Dickinson was quoted as saying [1], "We are guarding a bridge that may never be attacked: we hope it will not be. If it is not attacked, our work has succeeded". The bridge being attacked refers to the use of chemical warfare agents (CWAs). Research into CWAs is a strange field, scientists risk their lives and spend countless hours studying new materials to trap and decompose these chemicals of war, with the hope this knowledge is never needed for its intended purpose. That said, CWA decomposition work must continue, because if the "bridge" is ever attacked, we must be prepared. This chapter will focus on the history of CWAs, current protection measures, and the current work conducted on metal oxides with CWAs and their simulants.

1.1 Brief History of Chemical Warfare Agents

When discussing CWAs, we typically associate WWI with the first use of toxic gases in warfare. However, the use of toxic gases dates all the way back to 1000 BC, with the Chinese using arsenical smokes [2]. At the time, what was occurring chemically was not generally understood. A timeline of historical CWA attacks is shown in Figure 1.1. This development of CWA weapons continued to evolve, and even in the 15th century, Leonardo da Vinci proposed mortars be filled with arsenic sulfide and verdigris (copper carbonate) as an anti-ship weapon [2].

As the knowledge of chemistry advanced, so did the knowledge of how to use it destructively.

At the beginning of WWI, the French used ethyl bromoacetate grenades with no noticeable effects. The first successful, large-scale CWA attack occurred in April 1915 at the battle of Ypres. Under the advice of Fritz Haber, 168 tons of chlorine gas canisters were placed on German front lines. The attack successfully broke the British lines, but the Germans were unprepared for this success, and were unable to capitalize upon it before the British troops re-established the front lines [3, 4].

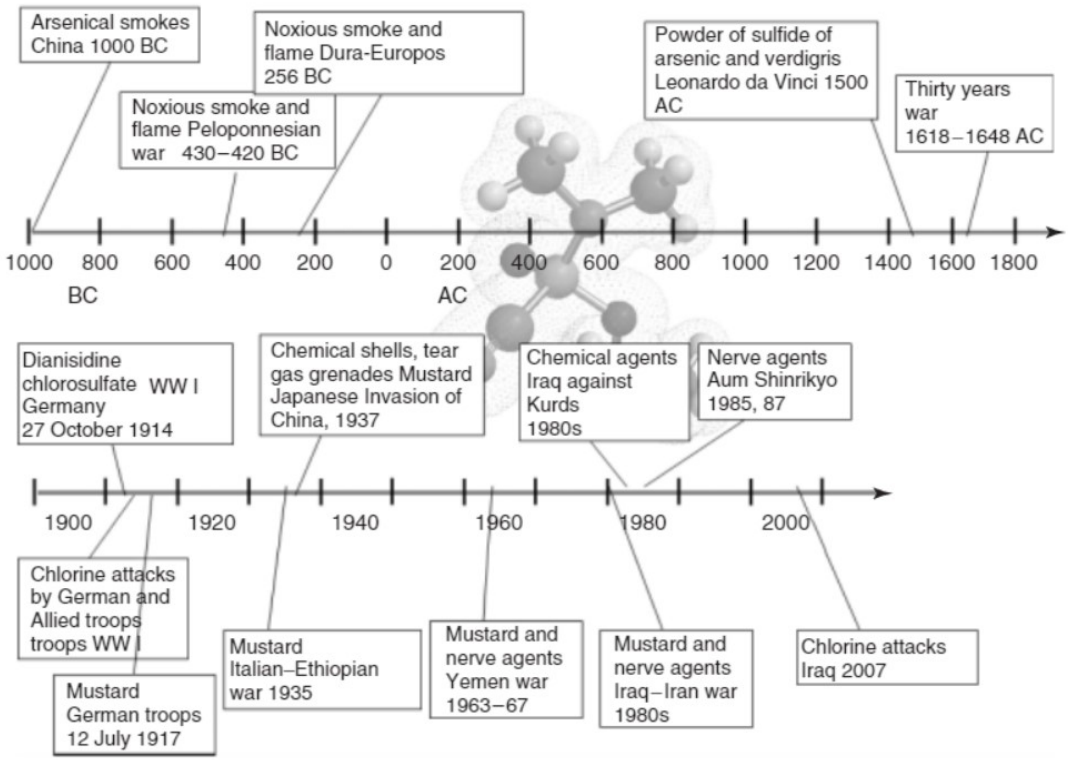


Figure 1.1: Timeline of historical applications of toxic chemicals from reference [2].

By the end of WWI, there were an estimated >1 million nonfatal CWA casualties and 82,000 fatalities. The CWAs' devastating effects prompted the international community to enact the 1925 Geneva Protocol, which outlawed the use of chemical and biological weapons in war [2]. In 1997, the Chemical Weapons Convention was drafted to completely ban the development, stockpiling, and use of CWAs. This convention includes the destruction of existing stockpiles, work that is ongoing. Despite international efforts, we have seen multiple uses of CWAs in the last decade [5].

Therefore, to protect civilians and Warfighters from potential attacks and growing threats, research and development into new protective equipment is a matter of national security.

1.2 Chemical Warfare Agent Protection

After the battle of Ypres, there was a rush to develop individual protection from CWAs. Initially, troops were issued untreated cotton masks that needed to remain moist to be effective against chlorine. Figure 1.2 shows select gas masks developed throughout history. In 1916, the small and large box respirators that were fielded to troops contained a more advanced filtration system than just cotton. The canister consisted of charcoal, soda-lime (NaOH and CaO), permanganate, brimstone (sulfer), and sodium sulfite, which provided better and longer protection from a larger range of chemicals [6, 7]. After WWI, the gas mask continued to evolve, providing a better fit and becoming less burdensome. However, filtration technology has not progressed at the same rate. In 1918, inventors J.C. Whetzel and E. W. Fuller developed the gold standard for military protection named "Whetlerite", a family of activated charcoals impregnated with different reactive chemicals, which provides a high surface area material with reactivate chemicals to protect against a wide range of CWAs. As new CWAs were developed, the impregnated chemicals within the activated carbon changed to meet the threat, leading to today's filters, which consist of activated carbon (bituminous coal (BPL) Carbon) and the mixture of impregnates known as ASZM-TEDA [8, 9].

ASZM-TEDA carbon is a dual-purpose sorbent, exhibiting both physical and chemical adsorption. The activated carbon known as BPL carbon is a microporous (< 2 nm) bituminous coal with a surface area of $\approx$1200 (m^2/g)[10]. The BPL carbon is intended for physisorption, which makes the dominating interaction weak van der Waals forces. Therefore, vapor pressure is an important factor in determining filtration effectiveness. Chemicals with high vapor pressure (> 10 torr) (phosgene, hydrogen cyanide (HCN), Cl_2) are likely to desorb and work their way through a carbon filter, whereas chemicals with lower vapor pressures (< 10 torr) (soman (GD), mustard (HD), tear gas

(CS)) are more likely to remain within the pores [11].

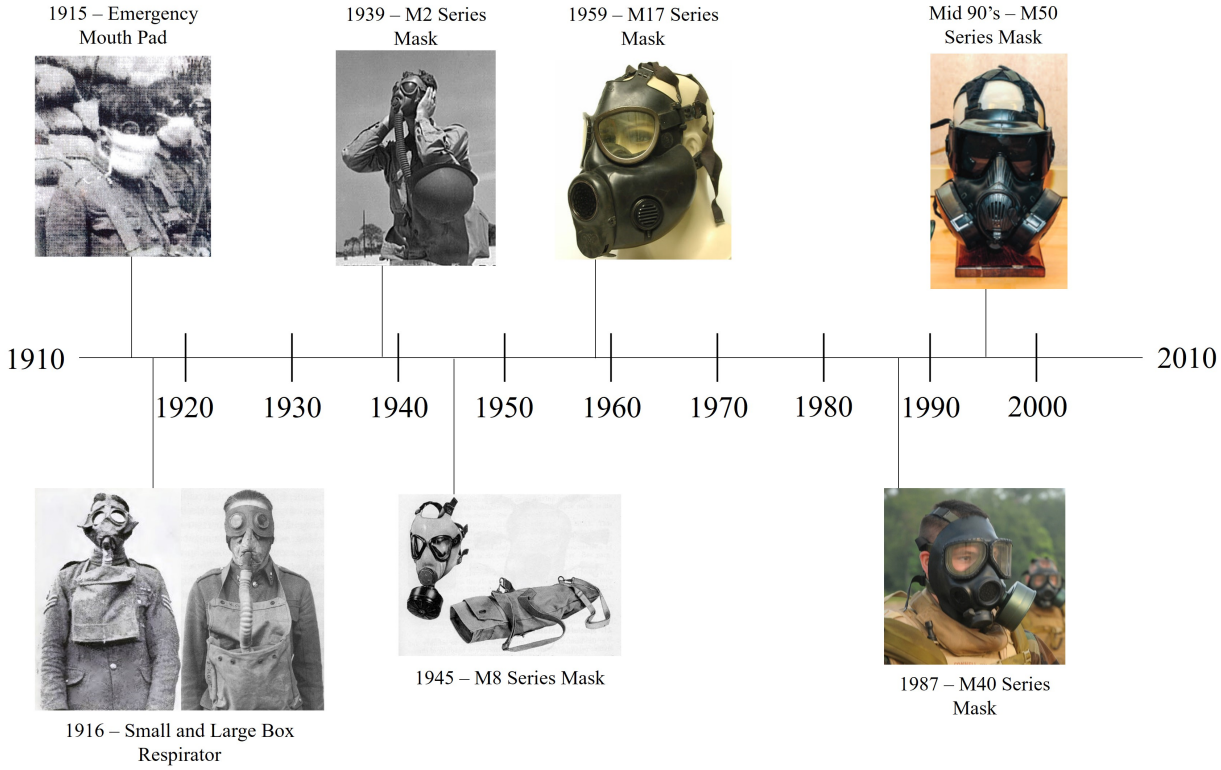


Figure 1.2: Timeline of select gas masks used throughout history [2, 6, 12, 13].

High-vapor-pressure toxins require a chemical reaction to occur, binding the agent to immobilize or degrade it to a less toxic chemical. To accomplish this task, the activated carbon is impregnated with ASZM-TEDA, which consists of (A) copper ($\approx$ 5%), (S) silver ($\approx$ 0.05%), (Z) zinc ($\approx$ 5%), (M) molybdenum ($\approx$ 2%) and (TEDA) triethylenediamine ($\approx$ 3%). The chemical composition and the intended gas protection are shown in Table 1.1 [11]. This combination has a broad range of reactivity, but is subject to degradation over time, adsorbing battlefield and environmental gases such as H_2O, SO_x, NO_x, CO_2, and diesel fuel, reducing the filter's protection capabilities [11, 14]. As this filter was developed using an Edisonian approach (trial and error), the underlying chemical mechanisms are not understood. Therefore, to develop a better filtration system for current threats and emerging threats, a fundamental understanding of the reactions oc-

curring is necessary to develop new design rules. Within this dissertation, several factors were studied to build the fundamental knowledge of the chemistry of organophosphorus molecules on metal oxide surfaces. By isolating specific factors such as crystal structures, cations, and dopant concentrations, and then exposing the metal oxides to different chemical probes including methyl paraoxon, diisopropyl fluorophosphate (DFP), soman and sarin. Decomposition mechanisms were proposed and important factors for reactivity were identified.

Table 1.1: Composition of the ASZM-TEDA impregnants and its intended protection adapted from reference [8, 11, 15]

Impregnant	**Loading Percent**	**Protection**
(A) copper (cupric carbonate)	5%	AsH_3, HCN, CK, Cl_2, PH_3, HF, H_2S, Phosgene
(S) silver	0.05%	AsH_3, PH_3
(Z) zinc (zinc carbonate)	5%	HCN, CK, Phosgene, NH_3
(M) molybdenum (ammonium dimolybdate)	2%	Organophosphate esters
(TEDA) triethylenediamine	3%	CK, CH_3Br, CH_3I, HCN, H_2S and SO_2
*CK = (CNCl), Phosgene ($COCl_2$)		

1.3 Organophosphorus CWAs and their Simulants

Among the most deadly CWAs are a class chemicals known as nerve agents. Nerve agents are organophosphorus molecules that act as cholinesterase (ChE) inhibitors. These agents are classified into several categories: the G-series, the V-series and the Novichocks [3]. Organophosphorus molecules do have a wide range of commercial uses, including in insecticides, hydraulic fluids, fuel additives, lubricants, plasticizers, and flame retardants [16]. However, even the "non-toxic" molecules have been linked to cancer and stunted neurodevelopment in children [17, 18].

Tetraethyl pyrophosphate (TEPP), the first known ChE inhibitor, was synthesized in 1854 by Wurtz. Luckily, when tasted resulted in no immediate ill effects. In the 1900s, the German com-

pany I.G. Farbenindustrie began investing in organophosphorus research, in an effort to develop new insecticides. On December 23, 1936, Gerhard Schrader synthesized the first "G" agent, as tabun (GA Figure 1.3d). He noted discomfort and constriction of his pupils when exposed to the vapors. About a year later, Schrader synthesized sarin, which is named in honor of the individuals who were instrumental in the synthesis **S**chrader, **A**mbros, **R**udriger, and van der L**in**de. During this time, the German government required chemicals to pass certain toxicity tests. This is when the true toxicity was discovered and examined for military use. This class of compounds are known as "G" agents, and allegedly given this classification because they were discovered in Germany [2, 3]. The chemical properties of the "G" series are summarized in Table 1.2.

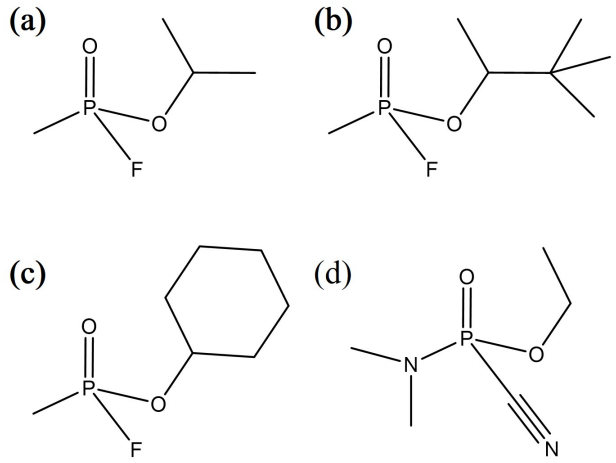


Figure 1.3: Organophosphorus nerve agents: (a) sarin (GB), (b) soman (GD), (c) cyclosarin (GF), (d) tabun (GA).

Nerve agents inhibit chemical communication in our bodies. Within the neuromuscular system, acetylcholine (ACh) binds to receptor sites resulting in muscular contraction. When the body wants to release the muscle, acetylcholinesterase (AChE) hydrolyzes ACh, resulting in the enzyme leaving neurotransmitter. CWAs such as sarin prevent this process. These agents irreversibly bind to AChE, resulting in a build-up of ACh, causing the muscles to tighten continually, eventually leading to suffocation from respiratory paralysis [16, 20].

Within this dissertation, I will specifically focus on the defeat of sarin (GB). Although all

Table 1.2: Summarized physical properties of "G" series agents [19]. LD_{50} Lethal dose for 50% of individuals, LCt_{50} lethal concentration of aerosol agent for 50% of individuals.

	Tabun (GA)	**Sarin (GB)**	**Soman (GD)**	**Cyclosarin (GF)**
Appearance and odor	Colorless to brown	Colorless	Colorless	Colorless
Odor	Faintly fruity; none when pure	None when pure	Fruity: camphor when impure	None when pure
Molecular Weight (g/mol)	162.13	140.09	182.17	180.16
Melting Point (C°)	-50	-56	-42	<-30
Boiling Point (C°)	248	150	198	228
Vapor Toxicity LCt_{50} (min mg/m^3)	70	35	35	35
Skin Toxicity LD_{50} (mg/70 kg man)	1,500	1,700	350	350
Vapor pressure (torr) (25C°)	0.057	2.48	0.40	0.093
Volatility (mg/m^3) (25C°)	497	18,700	3,930	898

CWAs are dangerous, sarin is the most volatile "G" agent, and it is therefore a greater threat to break through current filtration technology [11, 19]. Within an academic setting, it is dangerous and illegal to handle live agents. Therefore, several simulants are used to study the reactivity and surface interactions in a safe manner. The most common simulants are pictured in Figure 1.4b and c. Dimethyl methylphosphonate (DMMP) is the most common simulant used for gas-phase studies in academia. DMMP is stable, has low toxicity, and shares similar functional groups with sarin, but lacks the highly toxic P-F bond or a good leaving group. Research has shown that DMMP has similar heat of adsorption as sarin, making DMMP a good choice to study adsorption mechanisms [21]. Next is dimethyl 4-nitrophenyl phosphonate (DMNP), more commonly known as methyl paraoxon. Methyl paraoxon has the added benefit of having a 4-nitrophenyl group, which is a good leaving group, mimicking the P-F bond in sarin. Typically, methyl paraoxon decomposition is conducted in solution, and the anion of 4-nitrophenol absorbs strongly at 402 nm, making DMNP a great simulant for measuring kinetics [22]. However, gas-phase studies with methyl paraoxon are difficult as the IR spectrum is dominated by 4-nitrophenol. The third simulant in Figure 1.4a, is diisopropyl fluorophosphate (DFP), which is the closest to sarin in molecular structure. DFP shares the P-OC_3H_7 and P-F functional groups, but by replacing sarin's methyl group with an isopropyl group the toxicity is reduced. DFP is the least studied simulant, likely due to it being an

AChE inhibitor. DFP has been shown to be the simulant that is most similar in reactivity to sarin [23]. Common decomposition pathways for these simulants will be discussed in further detail in a Section 1.5.

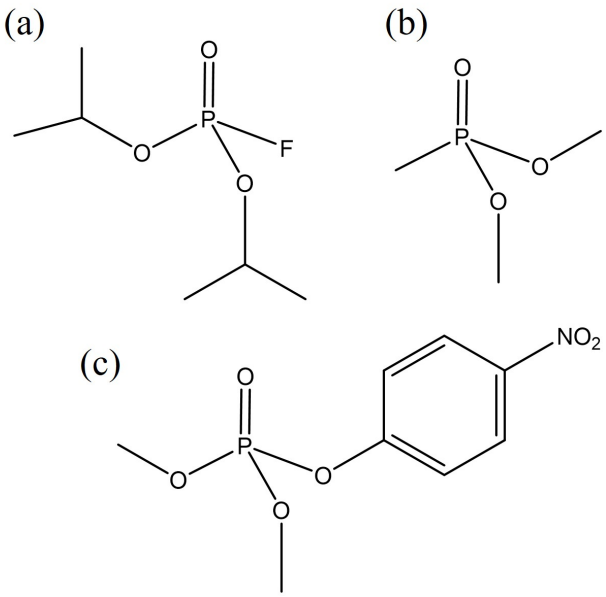


Figure 1.4: Organophosphorus simulants: (a) diisopropyl fluorophosphate (DFP), (b) dimethyl methylphosphonate (DMMP), (c) methyl paraoxon (DMNP).

1.4 Next-Generation Filtration Materials

The replacement for ASZM-TEDA will need to be a material that is rugged, reactive and non-toxic; material that is stable and can withstand environmental gases, extended levels of moisture, and high temperatures; a material with high surface area, with larger pores > 2 nm to facilitate mass transfer of CWAs; a material that is large enough to be packed in a filter, but won't break down to dust resulting in pressure drop across the bed. Several next-generation filtration candidates studied include metal-organic frameworks (MOFs), zeolites, and metal oxides. Section 1.4.1 and 1.4.2 will focus on work studying MOFs and zeolites. Section 1.5 will focus on metal oxides, mostly nanoparticles, and the decomposition of nerve agents and their simulants.

1.4.1 Metal Organic Frameworks (MOFs)

Metal-organic frameworks were first reported in 1995 [24]. Since then, MOFs research has grown exponentially within the chemistry community, with applications including gas storage [25, 26], separations [27, 28], and catalysis [29, 30]. MOFs consist of organic linkers and secondary building units (SBUs) with 3 to 12 points of contact. This combination creates a structure with controllable pore sizes, and reactive centers with surface areas reported up to 7,140 m^2/g [31–33].

Some of the most studied MOFs in CWA filtration are SBUs containing zirconium. The Zr-MOFs contain catalytically active Zr_6 sites, which act as a Lewis acid site and can be combined with different linkers to provide different pore structures. UiO-66, UiO-67, NU-1000 and MOF-808 (Figure 1.5) are the most commonly studied. Typically CWA decomposition experiments are performed in an aqueous buffered solution, allowing free hydroxyls to regenerate the Zr nodes, resulting in highly catalytic materials. MOF-808 and UiO-66 have reported half lives of < 0.5 min and 35 min, respectively for the decomposition of methyl paraoxon [34]. Sarin (GB) and soman (GD) also decompose on Zr-MOFs, with hydrolysis half lives from 2 min to 7 min for GB and 31-47 min for GD [22]. Zr-MOFs can even be combined with polymers, or integrated into fabrics for potential use in chemical-resistant clothing [35–37]

Although MOFs have shown promising results for CWA decomposition, there are many issues that need to be addressed before these materials become a viable option for CWA filtration. MOFs are only catalytic in basic aqueous solutions and have not been thoroughly tested in the gas phase [24]. MOF synthesis requires toxic solvents such as chloroform, dimethylformamide (DMF), dimethyl sulfoxide (DMSO) and diethylene formamide (DEF), which can remain within the pores unless extensive cleaning procedures are employed. In addition, MOF stability is a known issue, with linkers such as carboxylates, phosphonates, sulfonates, imidazolates, phenolates, and amines, which if degraded are toxic as well. Most MOFs are considered microporous, i.e. with pores diameters < 2 nm, which makes access to the full structure difficult for larger molecules.

Sarin is the smallest nerve agent at approximately 0.65 nm, making it larger than the porese of some MOFs, such as UiO-66 [38].

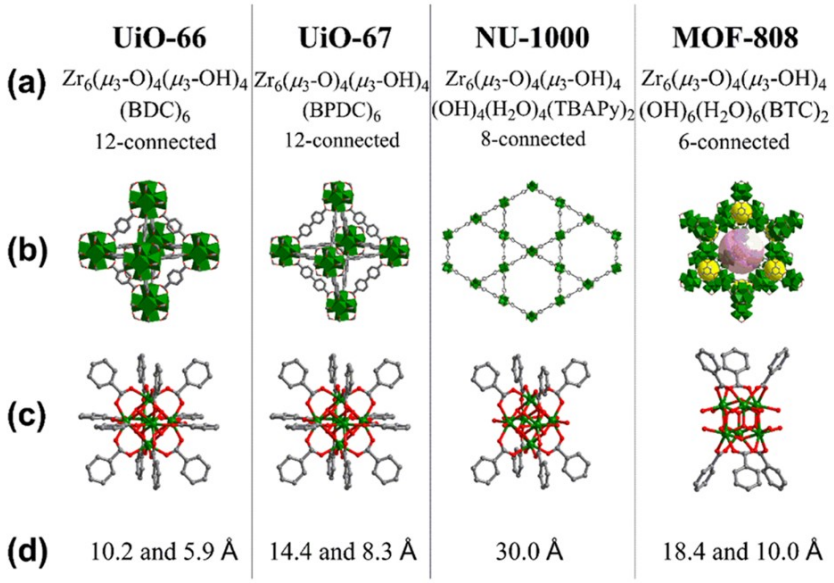


Figure 1.5: Commonly studied MOFs for CWA adsorption/decomposition, (a) chemical formula and node coordination, (b) cage structure, (c) coordination environment of the zirconium nodes, and (d) largest pore/cage diameter of the framework [39]

1.4.2 Zeolites

Zeolites are naturally occurring materials that were discovered over 250 year ago [40, 41]. Since then, approximately 40 more zeolites have been discovered in nature and 140 have been synthesized. Zeolites are generally aluminosilicates that form a rigid porous structure with pores typically ranging from 0.1 nm to 1 nm and high surface areas up to 1000 m^2/g. Zeolites have high thermal stability and possess tuneable acidic sites [38, 42]. Due to this unique porous structure, zeolites have become one of the most widely used catalysts for industrial purposes, with applications in oil cracking (catalysis), gas separation and ion exchange [40, 41].

Bellamy et al. studied the adsorption of blistering agent mustard gas (HD) zeolite 13x. The dried zeolite adsorbed 100% of HD with a capacity of 1.4 mmol of HD per gram of material.

However, with slight moisture (22% RH), the capacity for HD decreased to 52% [43]. Wagner and Bartram studied the adsorption of HD and nerve agent VX (O-ethyl S-2-(diisopropyl amino) ethyl methylphosphonothioate) on NaY and AgY zeolites . HD decomposed faster on NaY through hydrolysis, while VX decomposted faster on AgY through silver-catalyzed hydrolysis. AgY desulfured VX, forming the less toxic ethyl 2-(diisopropyl amino) ethyl methylphosphonate (QB) [44]. Despite the commercial success of zeolites in catalysis, studies of CWA decomposition were not as fuitful [43–47].

1.5 Decomposition of Organophosphorus Molecules on Metal Oxides

Metals and metal oxides have long been studied in the field of heterogeneous catalysis. What makes these materials attractive is their abundance, low cost, and active Lewis or Brønsted acid/basic sites. Transition metals are multivalent, and can perform redox chemistry [48]. The properties of the metals can be tuned to support different types of reactions. For example, NiO is a p-type semiconductor, and naturally forms Ni^{2+} vacancies. To charge balance this vacancy, two of the surrounding sites oxidize creating O^{-} or Ni^{3+} sites. The concentration of Ni^{2+} vacancies can be increased by doping lithium into the lattice, increasing oxidation of CO and volatile organic compounds (VOC). Alternatively, by doping zinc or chromium, the number of the Ni^{2+} vacancies will decrease making the catalyst better for dehydrogenation reactions [49].

For this reason, metal oxides have received significant attention from the scientific community. Binary metal oxides such as Al_2O_3 [50–53], CeO_2 [54–56], CuO [57–59], Cu_2O [59, 60], Fe_2O_3 [53], La_2O_3 [53], MgO [53, 61], MoO_2 [62, 63], MoO_3 [64], TiO_2 [54, 65–69], WO_3 [70], Y_2O_3 [71], ZnO [72, 73] and ZrO_2 [74] have been studied with chemical agents and their simulants. Organophosphorus molecules typically interact with the surface in three different manners (Figure 1.6). The molecule is attracted to the under-coordinated Lewis acid sites or the Brønsted acid sites through the P=O bond. Alternatively, the organophosphorus molecule will interact with the surface

hydroxyl. Interactions directly with the metal centers are significantly stronger than hydrogen bonding interaction [59, 73].

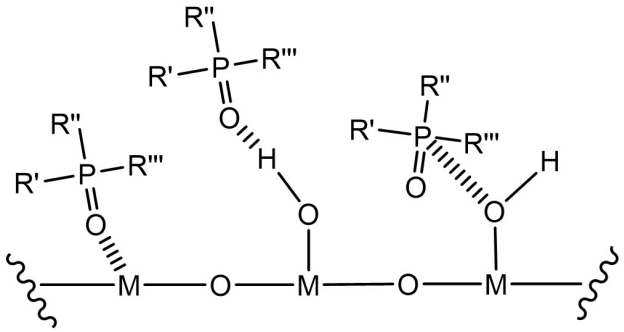


Figure 1.6: General adsorption interactions with an organophosphorus molecule and a metal oxide surface.

A basic metric for evaluating a successful filter material is the extent to which it mitigates both the passing of the CWA and its potentially toxic byproducts to the end user. Sarin's common decomposition products are shown in Figure 1.7 with their realative acute toxicity. For perspective, the LD50 of caffeine is approximately 367 mg/kg in rats [75]. Cleavage of the P-F bond results in a product that is almost 14,000 times less toxic than sarin. Organophosphorus decomposition is typically discussed as proceeding through hydrolysis, dealkylation, and/or oxidation [76]. However, the oxidation state of phosphorus is +5, and will not oxidize further. Oxidation refers to the oxidation of functional groups, but will not be discussed here, as those mechanisms are specific to each experiment. A fourth category, dehalogenation, could be added to the list, as this mechanism is seen on dry metal oxides, which will be discussed in Chapter 4.

The simplest and most common form of decomposition is hydrolysis. Exposure to atmospheric water causes sarin to degrade slowly. Sarin hydrolysis occurs through the P-F bond, and in methyl paraoxon through the P-(4-nitrophenyl). In both cases, water or surface hydroxyls perform nucleophilic substitution (SN_2), releasing water or the HF/4-nitrophenol into the environment, shown in Figure 1.8a. Hydrolysis of methyl paraoxon is seen in different metal oxides including MgO, TiO_2, CeO_2 and ZrO_2 [56, 78]. As methyl paraoxon reactions are conducted in solution, 4-nitrophenol is

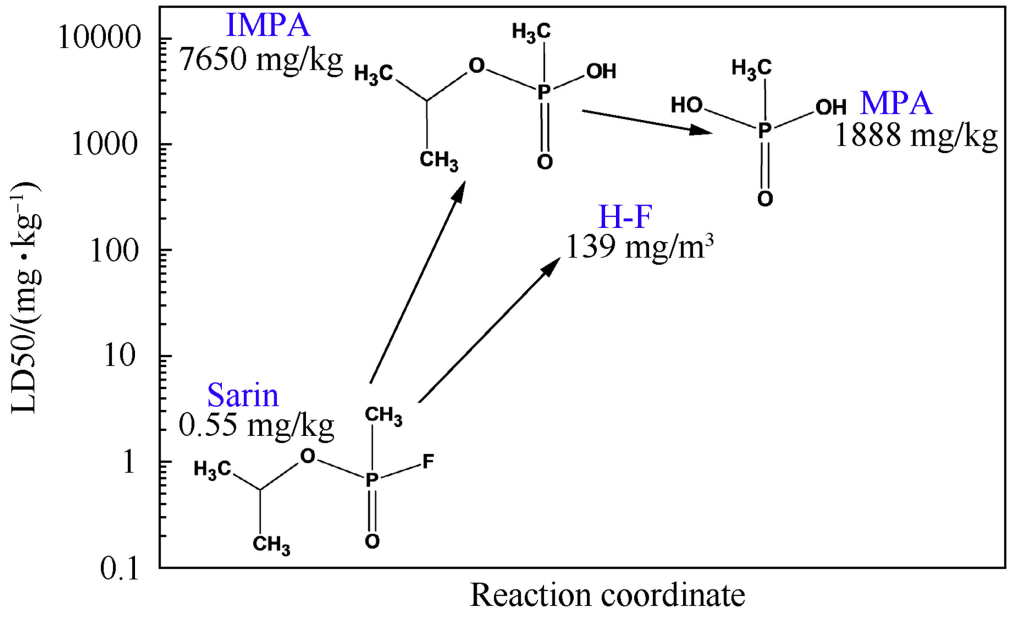


Figure 1.7: Acute toxicity of sarin and the common decomposition products [77].

typically released back into the solvent. Kuiper et al. conducted a detailed study of GB adsorption and decomposition on γ-Al_2O_3. They discovered that after adsorption, GB hydrolyzes with the assistance of surface hydroxyls into isopropyl methyl phosphonic acid (IMPA), creating a bridging species on the surface. The fluorine remains on the surface, poisoning the catalyst and preventing further decomposition [79]. These mechanisms are summarized in Figure 1.8b. In organophosphorus decomposition, the creation of a bridging species and fluorine remaining on the surface is common and requires a lot of energy to remove, which makes catalysis difficult to achieve.

The next type of decomposition is dealkylation. In dealkylation, GB and GD can be cleaved at the PO-C_NH_{2N+1} bond, producing an alkene C_NH_{2N}. Alternatively cleavage of the P-OC_NH_{2N+1} bond produces the respective alcohol. Production of propene has been experimentally shown and computationally predicted on dry TiO_2 [80], and computationally predicted on dry MoO_2 [62]. After adsorption, the electrons from sarin's P=O oxygen interacts with a metal site. Subsequently, hydrogen from the PO-C_3H_7 shifts to a neighboring oxygen, while the P-O forms a new bond with the metal site, ultimately releasing propene, Figure 1.9a. Another alternative, is cleavage through

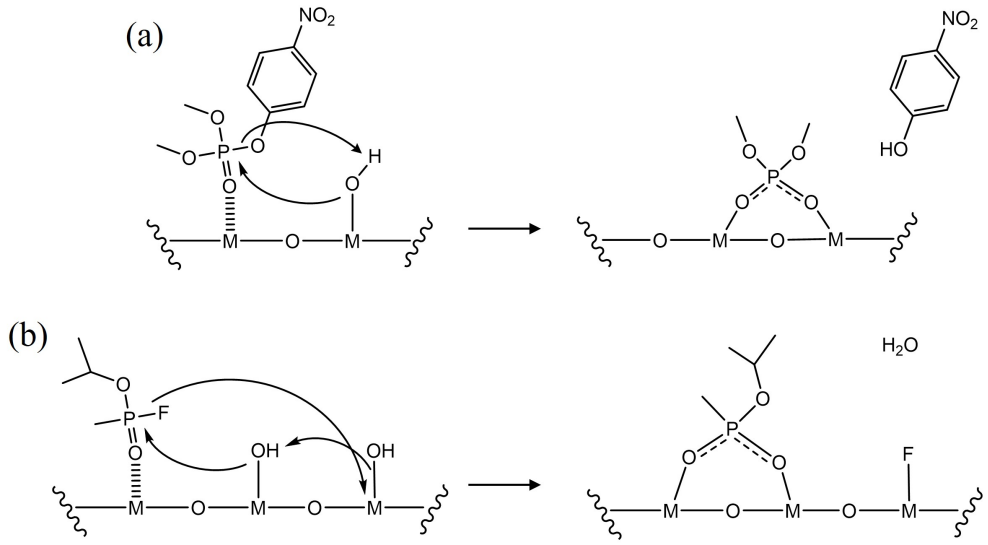


Figure 1.8: Generalized hydrolysis of (a) methyl paraoxon where the leaving group (4-nitrophenol) is released into the environment and (b) sarin where the fluorine remains bound to the surface [56, 79].

the P-$O_N H_{2N+1}$ bond. This elimination has been predicted on dry ZnO [73] and shown experimentally with MgO [61]. On MgO, GD initially adsorbs and hydrolyzes, but will react further, cleaving the pinacolyl alcohol group, which remains bound to the MgO surface. This mechanism is depicted in Figure 1.9b. In dealkylation, the main product is methyl phosphonofluoridic acid, with a lethal dose at 300mg/kg which is less toxic than GB and GD, but is more toxic than the hydrolysis product [81].

1.5.1 Titanium (TiO_2) and Cerium Oxide (CeO_2)

TiO_2 and CeO_2 have drawn a large interest in CWA filtration from their success in heterogeneous catalysis. TiO_2 is a well-known photocatalyst, but has shown low reactivity with organophosphorus molecules without external excitation [54, 65–68]. Dry TiO_2 has been examined for the decomposition of DMMP and sarin within a high-vacuum system. These studies found sarin only physisorbs at room temperature, whereas DMMP exhibits slight decomposition. When the sample is heated, decomposition is observed, and a bridging species is created on the surface [67, 80].

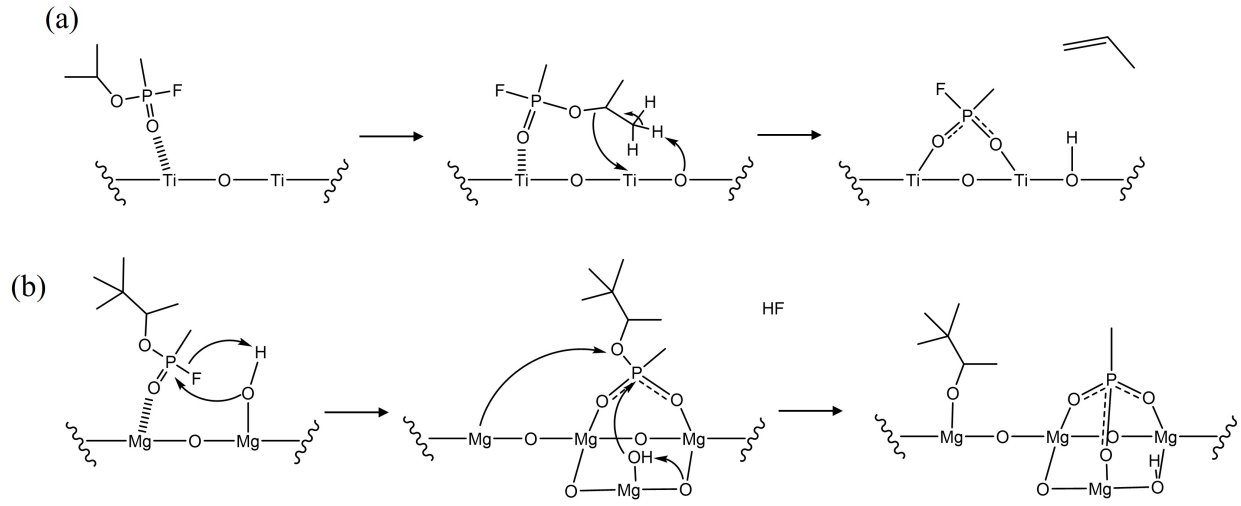


Figure 1.9: (a) Dealkylation mechanism of sarin on TiO_2 producing propene. (b) Soman hydrolyzed followed by cleavage of the P-OC_6H_{14} [61, 80].

CeO_2 is also a well known photocatalyst, but its largest use is in catalytic converters as three-way catalyst, oxidizing CO and reducing NO_x. CeO_2 has shown the potential for heterogeneous decomposition of CWAs at room temperature [55, 82]. With the simulant DMMP, mesoporous CeO_2 can cleave the methoxy group from DMMP, forming a Ce-OCH_3 bond. Through DFT calculations, the importance of crystallographic planes for decomposition was investigated. The (111) plane has a low activation barrier [55]. Trenque and colleagues synthetically controlled the surface facets of CeO_2, finding that methyl paraoxon (DMNP) was most active on nanoparticles with the (111) as the primary surface [56].

Therefore, we asked the question, **can the activity of TiO_2 increase through isovalent substitution of Ce^{4+} into the anatase crystal structure?** This idea led to the study discussed in Chapter 3. In this work, we synthesized and characterized ordered mesoporous $Ce_xTi_{1-x}O_2$ ($x \leq 15\%$), TiO_2 and CeO_2. We showed that Ce is incorporated into the anatase crystal structure with no phase separation up to 15% dopant. The ordered mesoporous structure was maintained, resulting in MMOs with high surface areas. The MMOs were exposed to methyl paraoxon in a propanol environment to measure the decomposition kinetics. Pure CeO_2, is the most reactive with the fastest

kinetics when normalized to surface area. TiO_2 and $Ce_xTi_{1-x}O_2$ ($x \leq 15\%$) had little to no effect in kinetics or reactivity, showing that the Lewis acid site (Ce^{4+} or Ti^{4+}) is less important for methyl paraoxon decomposition than the crystallographic structure.

1.5.2 Copper Oxide (CuO)

The adsorption and decomposition of DMMP on CuO was studied by Lena Trotochaud and colleagues through diffuse reflectance infrared spectroscopy (DRIFTS), near ambient pressure x-ray photoelectron spectroscopy (NAP-XPS) and density functional theory (DFT) [57]. Their study revealed that CuO is highly active in the decomposition of DMMP at room temperature. In their DRIFTS measurements, a new peak formed at 1108 cm^{-1}. Using DFT calculations, the authors were able to attribute this peak to a Cu-OCH_3 and O-P-O mode. In addition, the intensity of peaks associated with P-CH_3 modes decreased as the exposure time increased, showing CuO decomposes DMMP the question of what was being cleaved and how was addressed using NAP-XPS and DFT.

With the NAP-XPS, the phosphorus signal was fit to 2 peaks, corresponding to 2 different environments.There were 3 peaks in the oxygen region corresponding to P-OCH_3, oxygen within the lattice and to Cu-O-X. Where X is used as a generic term, as the specific moiety cannot be determined directly through NAP-XPS. With the addition of DFT calculations, the authors showed the cleavage of the P-OCH_3, P-CH_3 and PO-CH_3 bonds are all thermodynamically favorable. The cleavage of the P-CH_3 has not been shown at room temperature on any other metal oxide.

That study laid the ground work, showing that CuO is highly reactive with a CWA simulant, which lead to the inspiration for my work in Chapter 4. **To determine if DMMP decomposition translates to sarin decomposition, CuO nanoparticles were exposed to sarin and studied through IR spectroscopy.** The CuO NPs were heated to remove all contaminants and hydroxyls from the surface, and then exposed to sarin. The dry CuO nanoparticles were highly reactive, primarily cleaving the P-F bond and producing a bridging species on the surface.

1.5.3 Nickel Oxide (NiO) and Copper doped NiO

In Chapter 4, I demonstrate the high activity for sarin decomposition on CuO. However, can we increase the reactivity? Cu^{2+} has an electronic configuration of d^9, and under specific geometries the coordination will distort to break degeneracy of the crystal field energy levels. This phenomenon is known as the Jahn-Teller distortion, which has been linked to increased catalysis in the oxygen-reduction reaction [83]. One of the Jahn-Teller active geometries is octahedral. NiO adopts a rock-salt crystal structure, with a local octahedral geometry. **Therefore, Cu^{2+} was isovalently substituted within the NiO lattice to probe the effects of Cu^{2+} within a Jahn-Teller active geometry on CWA decomposition.**

Pure nickel oxide has yet to be explored for the decomposition of CWAs and CWA simulants. NiO is used in a variety of scientific fields, including VOCs combustion [84] and CO oxidation [85]. As mentioned previously, NiO is a known p-type semiconductor, and naturally contains nickel vacancies. Nickel vacancies have been linked to increased oxygen activity, which in turn increases the material's oxidative capabilities [49].

These factors provided the motivation for Chapter 5. In this chapter, a solid solution of mesoporous $Cu_xNi_{1-x}O$ (x = 0.1, 0.2) and NiO was synthesized through a hard templating method. The resultant MMOs were fully characterized, demonstrating that Cu^{2+} was successfully incorporated into the NiO lattice. While maintaining high surface areas. However, the Cu^{2+} reduced Ni^{2+} vacancies. NiO was discovered to be highly reactive to DFP, producing primarily CO, CO_2, carbonyls and carbonates on the surface. Not only did this process occur at room temperature, but also at temperatures as low as -50 °C. Testing the sample under an oxygen-rich (zero air) and oxygen-poor (He) atmospheres, we demonstrate the importance of surface oxygen on the material's reactivity. $Cu_xNi_{1-x}O$ produced similar results, with reduced activity, this is due to the filling of the Ni^{2+} vacancies and subsequently, active oxygen.

Chapter 2: Materials and Techniques

Heterogeneous reactions occur on the surface of a material. Therefore, special attention must go towards designing a material that has a large surface area to maximize the number of active sites. Within this dissertation, both nanoparticles and mesoporous metal oxides were studied due to their large surface areas and high reactivity. To understand the bulk and surface properties of a material, multiple characterization techniques are required. The basics of the main techniques, such as nitrogen adsorption, X-ray diffraction, and electron microscopy, are discussed in this section. For surface sensitive characterization, infrared (IR) spectroscopy is used to not only characterize the material's surface, but also to study the decomposition of chemical warfare agents (CWA) and stimulants. For measuring the decomposition kinetics of CWA simulant in a solvent, ultraviolet-visible spectroscopy (UV-Vis) is employed. The combination of techniques allows for investigation into the material and what properties are important for surface interactions.

2.1 Materials

2.1.1 Nanoparticles

As particle size decreases, the specific surface area increases, leading to unique surface chemistry. One of the best known examples is gold nanoparticles. Gold in the bulk is valued for its inertness characteristics. When reduced to the nanometer dimensions, gold on a metal oxide support becomes highly active for the low-temperature oxidation of CO, the partial oxidation of hydrocarbons, and the reduction of nitrogen oxides [86]. Nanoparticles have a diameter between 1 and

100 nm. By decreasing the particle size, the fraction of bulk atoms decrease, therefore increasing the surface area of the material. Figure 2.1 depicts how decreasing the particle size increases a material's ratio of surface to bulk atoms and the resultant increasing in the specific surface area [87].

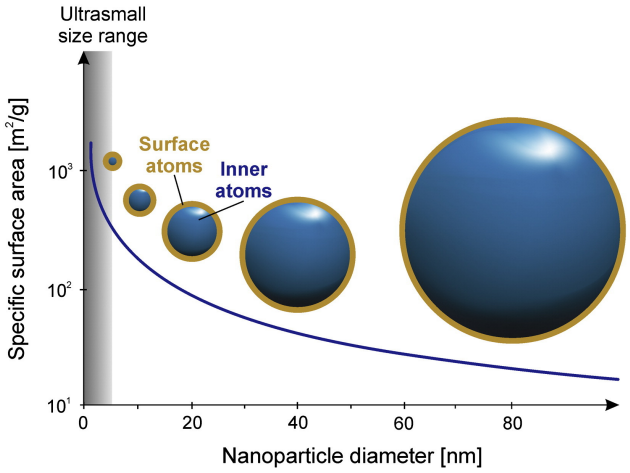


Figure 2.1: Plot depicting a nanoparticles surface area versus particle size. Image used with permission from reference [88]

An important feature of metals and metal oxides is that these materials are commonly crystalline, which means that they are composed of discrete building blocks. Therefore smaller particles will resemble more a sphere made of Legos, instead of a smooth sphere. Sharp edges and steps result in defects and under coordinated sites increasing reactivity [89]. Although the synthesis of nanoparticles is outside the scope of this dissertation, decades of research have gone into controlling nano particle size [87, 90]. From a practical standpoint, nanoparticles in a gas mask would be difficult to contain and would pack tightly, causing a large pressure drop behind the filter. By providing a structure for the metal oxides to form around, we can create a macroscopic structure that maintains high surface curvature, large surface area, and increased reactivity, all while preventing a large pressure drop. This strategy is the basis for the next section and the field of ordered mesoporous materials.

2.1.2 Order Mesoporous Materials

Porous materials are defined by the pore size which are separated into three categories: microporous (< 2 nm), mesoporous (2 nm to 50 nm) and macroporous (> 50 nm). For a molecule to react, it needs to find an open site on the surface. In small pores, large molecules are not able to diffuse into the material, or react at the entrance of a pore, closing off access to the interior sites. Large pores allow for full access to the surface, at the cost of decreased surface area. Mesoporous materials therefore lie within an interesting regime that maximizes surface area and molecular mobility [91]. Ordered mesoporous materials were first discovered in the late 1960s, but did not gain attention from the scientific community as the patent lacked crystallographic data and microscopy images [92]. Ordered mesoporous materials became well known in 1992, when Mobil scientists synthesized ordered mesoporous silicas, now known as the Mobil crystalline materials (MCM) series [93]. Since then, mesoporous materials have found uses in a variety of fields, including gas adsorption, drug delivery, sensors and heterogeneous catalysis [91].

There are two main approaches for synthesizing ordered mesoporous materials: soft and hard templating (Figure 2.2). Soft templating, relies on the self assembly nature of surfactants. A surfactant is a polymer that contains a non-polar and polar portion, shown in Figure 2.2. When surfactants are added to a solution at a concentration above the critical micelle concentration, the surfactants naturally self assemble into a structure that has the lowest Gibbs free energy. These structures are known as micelles. By changing the concentration, polymer components, and synthetic conditions, these micelles can assemble into a variety of different structures [91, 94].

In soft templating, the surfactants are referred to as structure-directing agents (SDAs). SDAs provide the structure about which the materials form. Within soft templating there are two synthesis approaches: surfactant/inorganic self-assembly as seen in materials such as SBA-15, and liquid crystal-templating, as used in the synthesis of FDU-15. In the surfactant/inorganic self-assembly of SBA-15, the SDA (P123) and an inorganic precursor tetraethyl orthosilicate (TEOS), are stirred

in an acidic aqueous solution at a slightly elevated temperature. Although the exact formation mechanism is not entirely understood, the community tends to believe that the self-assembly process follows the cooperative formation mechanism. The charged portion of the surfactant interacts and bonds with the inorganic precursor, changing the overall charge density. This cooperative interaction continues between the surfactant and the inorganic species, leading to the formation of the ordered mesoporous material. Making charge matching more important for structure formation than SDA concentration, allowing multiple structures to be synthesized with the same surfactant [91, 94].

In the synthesis of SBA-15, a simple aging process controls the highly ordered pore sizes between 4.6 nm to 11 nm. By placing the formed particles and mother liquor in an oven, the surfactants swell, increasing the pore sizes, allowing for these materials to be tailored to a variety of situations and environments [95]. To obtain the final mesoporous material, the surfactant needs to be removed. There are a variety of different techniques to remove the surfactant, but the most common are heating and solvent extraction. By refluxing the particles in ethanol, the surfactant dissolves into the solution, opening up the main mesopores. What makes SBA-15 unique is micropores form between the mesopores, which will not be opened with just solvent. By heating the material to higher temperatures, the surfactant decomposes opening up both the mesopores and the smaller micropores. Yielding a material with a surface area of 700 to 1000 m^2/g [91].

Liquid-crystal templating also relies on the use of an SDA. However not all precursors polymerize as easily as TEOS. Synthesis of materials such as FDU-15 relies on this type of templating for formation. The SDA (F127) is mixed with a low-molecular-weight phenolic resin. In contrast to the synthesis of SBA-15, the phenolic resin and SDA do not bond to form the macro structure. By pouring the solution into a dish and allowing the solvent to evaporate slowly, the SDAs will form the macro structure, with the phenolic resin forming around the micelles. This technique is known as evaporation-induced self-assembly (EISA). Upon gentle heating, the phenolic resin polymerizes around the SDA. With higher heating under inert gas, the phenolic resin continues to

carbonize and the SDA evaporates, resulting in the mesoporous carbon [96].

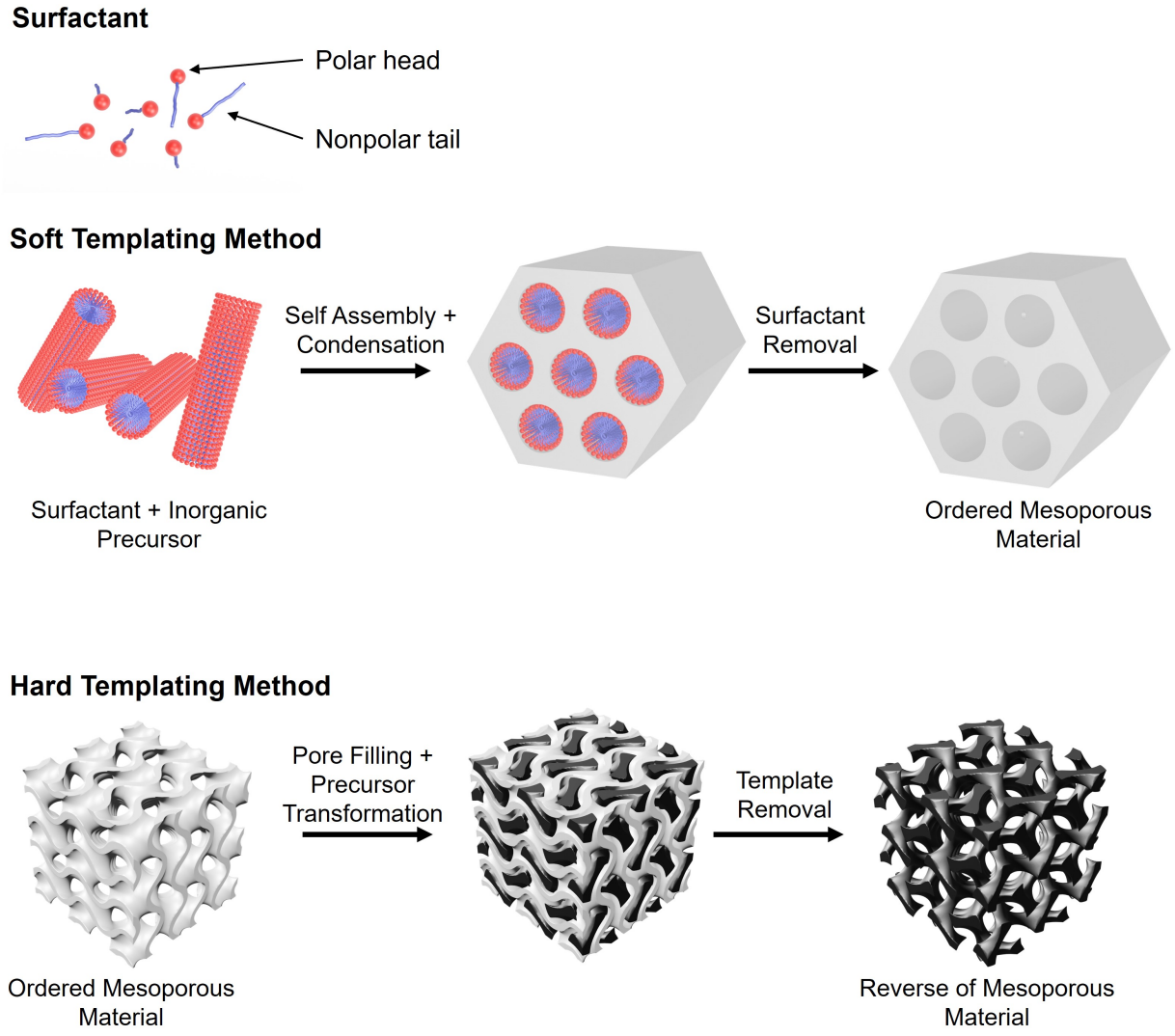


Figure 2.2: Graphical representation of a surfactant (top) and the main methods for the synthesis of ordered mesoporous materials. (middle) Soft templating or (bottom) hard templating/nanocasting method.

For the synthesis of mesoporous metal oxides, a hard templating approach is typically used. Metal salts are often used as a precursor that does not polymerize and will affect the self-assembly of the micelles. Therefore, the resultant product will not be ordered, and will not have a uniform pore size. However, using a sacrificial template the metal oxides can form within the pores, when the template is removed, the reverse internal structure remains. Typically, a silica or carbon meso-

porous material is used as the template. The metal salt is dissolved in a solvent with the template, where the solvent evaporates and the salt fills in and around the pores. Heating the mixture slowly causes the salt to melt further infiltrating the pores [94, 97]. With enough heat, the salt decomposes into the desired metal oxide. The strong template allows for high enough heat to create a crystalline surface. The template is then removed chemically, by etching away the silica with NaOH, or heat to burn away the carbon template. This method creates an ordered structure with a crystalline surface and a specific surface area of 70 to 300 m^2/g [98].

2.2 Characterization Techniques

2.2.1 Nitrogen Adsorption

An important characteristic of mesoporous materials are their large specific surface areas and their tunable pore sizes. Gas sorption is the primary characterization technique to quantify these properties. When gas is introduced into a material, the gas will either physisorb to the surface or remain in the gas phase. By precisely measuring the pressure and quantity of gas introduced into a material, an isotherm can be constructed. Through several methods discussed below, properties such as surface area and pore size can be measured. Any gas can be used for creating an isotherm, typically inert gases such as N_2, krypton, or argon are used. Throughout this dissertation N_2 is exclusively used for sorption experiments [99].

The International Union of Pure and Applied Chemistry (IUPAC) has classified six sorption isotherms[100]. For this work, we will only discuss Types I, II and IV (Figure 2.3). Type I isotherms are typical of monolayer adsorption, as seen in microporous materials and with chemisorption. The surface becomes saturated at low partial pressures. Type II and IV isotherms rapidly adsorb at low pressure creating primarily a monolayer. Multilayer adsorption then becomes dominant. The beginning of multilayer adsorption is seen from an inflection point in the data, marked with a B in Figure 2.3. Type II isotherm is typical with macroporous or non-porous materials, in

which multilayer adsorption is unrestricted. Type IV isotherm is typical of mesoporous materials, as is evident by the hysteresis loop and sharp increase in gas adsorption from pore condensation [100].

During the adoption of gas in mesoporous material, multilayers build on the walls slowly making the pore smaller. This process continues until the pore condensation pressure is attained, after which where there is a quick uptake of gas. Upon desorption, the gases within the pores require more energy (a lower partial pressure) to exit the pores. This phenomenon is due to the meniscus formed, which increases the adhesion forces. IUPAC defines 4 types of hysteresis for porous materials. H1 is characteristic of uniform cylindrical type pores, and H2 is characteristic of ink well-type pores. H3 is characteristic of nanoparticles, including aggregates, and H4 is characteristic of slit-like pores (Figure 2.3) [100].

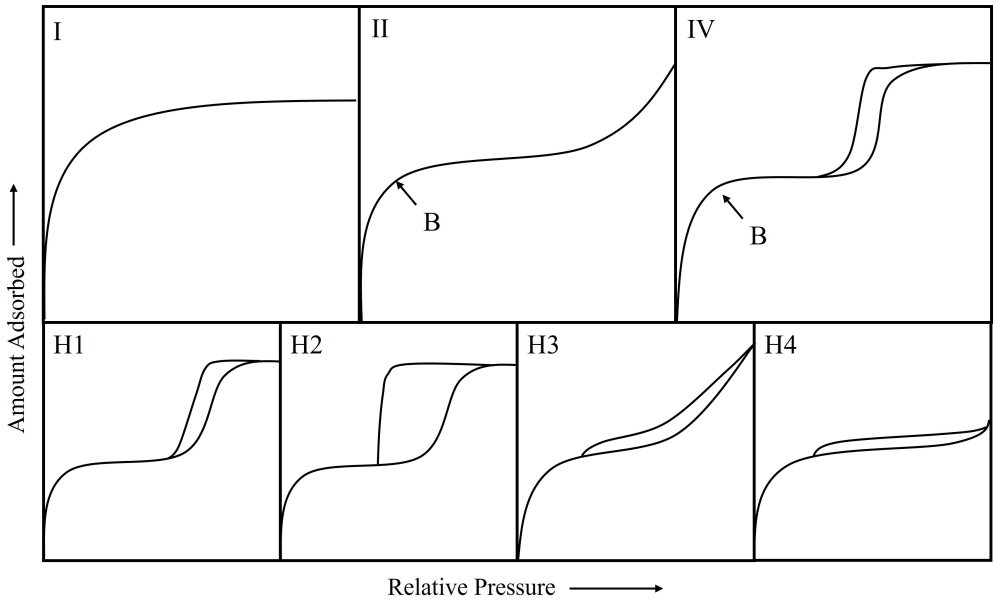


Figure 2.3: Example adsorption isotherms of Type I, II, and IV and the common mesoporous hysteresis. Point B represents the transition to multilayer adsorption.

Calculation of the surface area requires an understanding of the mechanism and thermodynamics of gas adsorption. When a gas is introduced to a material at low partial pressures (P/P_o), where P is the measured pressure and P_o is the saturation pressure. The gas will physisorb to most ener-

getic sites which lie on the surface, to minimize Gibbs free energy. In theory, gases will physisorb to a surface until a single monolayer is achieved, however in real systems gases form multilayers before a full monolayer is achieved. The researchers Brunauer, Emmett, and Teller developed an extension of Langmuir theory to better model real materials. In their theory, molecules in the monolayers and subsequent layers remain in equilibrium between the adsorbed phase and the gas phase. This assumption allowed them to derive what is known as the BET surface area shown in the linearized form in Equation 2.1.

$$\frac{1}{\nu[1-(P_o/P)]} = \frac{c-1}{\nu_m c}\left(\frac{P}{P_o}\right) + \frac{1}{\nu_m c} \tag{2.1}$$

Where ν is the quantity of the adsorbed gas, ν_m is the monolayer of the adsorbed gas and c is the BET constant [99]. When the measured data is plotted with Equation 2.1, the data is linearized allowing for the calculation of the slope and y-intercept. These parameters can be used to calculate ν_m and c. Rearranging equation 2.1, we get equations 2.2.

$$\nu_m = \frac{1}{A+I} \qquad c = 1 + \frac{A}{I} \tag{2.2}$$

Where A is the slope and I is the y-intercept. Knowledge of the molecular diameter of the probe gas and the monolayer coverage ν_m, allows one to determine the BET surface area. For most experiments, determining the BET surface area at partial pressures between 0.05 - 0.30 (P/P_o) is the most accurate. For small pores ($< \sim 3.5$ nm), using a smaller range of partial pressures 0.05 - 0.20 (P/P_o) is necessary to be below the pore condensation pressure, keeping the calculations linear [99].

To calculate a mesoporous materials pore size, the first method developed is shown in Equation

2.3, known as the Kelvin equation.

$$ln\left(\frac{P}{P_o}\right) = \frac{-2\gamma\bar{V}}{rRT} \tag{2.3}$$

Where, $\bar{V}$ is the molar volume of the condensed liquid, r is the cylindrical pore radius, T is temperature, R is the universal gas constant and γ is surface tension. The Kelvin equation relates pore diameter to the pore condensation pressure. This equation assumes a uniform pore geometry and width [99]. However, in real systems, not all pores are uniform or cylindrical. Additional techniques have been developed, modifying the Kelvin equation to account for more complex situations. The most commonly used technique in mesoporous material is the Barrett-Joyner-Halenda method (BJH). This method accounts for preadsorbed multilayer films not included for in the Kelvin equation [101].

2.2.2 X-ray Diffraction (XRD)

X-ray diffraction (XRD) is one of the most powerful techniques for the characterization of crystalline materials. Crystalline materials are made up of simple building blocks known as unit cells. When the wavelength of the incoming plane wave is close to the interatomic distances, diffraction can be used to measure the distance between the crystallographic planes. If the outgoing waves leave the material with the same phase they will constructively interfere resulting in the amplification of the waves. However, waves that are out of phase destructively interfere canceling each other out. Constructive interference will only occur at specific angles which are defined by Bragg's law, graphically depicted in Figure 2.4 and mathematically in Equation 2.4. Here, d is the distance between crystallographic planes, θ is the incident angle of the X-rays, λ is the wavelength of the x-ray source and n is a positive integer [102].

$$2dsin(\theta) = n\lambda \tag{2.4}$$

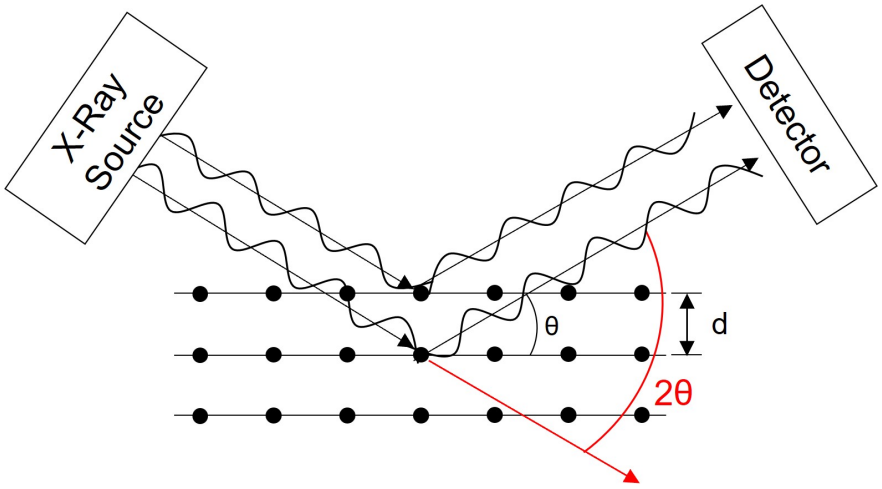


Figure 2.4: Graphical representation of Braggs law.

Because the geometry and dimensions of the unit cell are unique to each metal oxide, phase determination and purity are quickly accomplished with XRD. Quantitative analysis of XRD patterns are typically handled through Rietveld refinements. Rietveld refinement is a least-squares technique that fits a crystallographic structural model to the observed powder pattern. Unit cell parameters, crystallite size, and structural parameters can be refined and calculated through the Rietveld refinement [102].

2.2.3 Electron Microscopy

Optical microscopy does not have sufficient resolution to image mesopores. When electrons are accelerated under high voltages, the wavelengths can be 100,000 shorter than that of visible light, offering superior the magnification and resolution. Electron microscopy is a powerful tool that can capture a material's porous structure, bulk structure, local crystal facets, chemical composition, and much more [103].

Transmission Electron Microscopy (TEM)

In transmission electron microscopy, accelerated electrons are focused onto a sample suspended on a support, transmitted through the sample, and captured on the opposite side. Common accelerating voltages range from 40 to 200 kV. Higher voltages create a finer image but can damage the sample. The high magnification of TEM makes it the simplest technique for directly studying the pore structures. Direct imaging of the lattice fringe is possible within TEM, showing whether the material's surface is crystalline. Because the beam must transmit through the sample, the material must be less than $\sim$ 200 nm thick. Making bulk samples thin enough for TEM can require expensive and complicated techniques including focused ion beam milling, ultramicrotomy, and atom milling [103]. For mesoporous metal oxides, the preparation for TEM is fairly simple. The MMOs are ground and dispersed in a volatile solvent such as ethanol. The solvent is agitated and drop cast onto the TEM grid. With TEM, only a 2D image is visible, to see the structure in three dimensions scanning electron microscopy is required [103].

Scanning Electron Microscopy (SEM)

In scanning electron microscopy, electrons are also accelerated but at a lower accelerating voltage typically between 1 and 30 kV. The sample emits secondary and backscattered electrons which come only from the surface. The electrons are collected by detectors above the sample, and are compiled to create an image. The image will appear 3D and shows details of the surface topography. SEM sample preparation is less complicated than TEM. For conductive materials, the material is deposited on carbon tape and put onto the sample stage. For non-conductive materials, a thin layer of gold or carbon is sputtered on the surface to prevent charging [103].

Electron-dispersive X-ray Spectroscopy (EDS)

A technique often paired with TEM and SEM is electron-dispersive X-ray spectroscopy (EDS). High-energy electrons can excite inner shell electrons, ejecting them from the atom, leaving a vacancy. The higher shell electrons can relax and fill the core energy shell, emitting x-rays. The emitted X-rays are characteristic for each element, allowing for quick identification, quantification and mapping of elements in a material. EDS mapping will show where there is a density of atoms within a structure [103].

2.2.4 Ultraviolet-Visible Absorption Spectroscopy (UV/Vis)

Ultraviolet-visible absorption spectroscopy (UV/Vis) is a qualitative and quantitative technique that studies the electronic transitions within a molecule [104]. In CWA research, methyl paraoxon is a common simulant used to study the decomposition kinetics within a solvent. Decomposition of methyl paraoxon typically produces 4-nitrophenol and dimethyl phosphonate. Under basic conditions, 4-nitrophenol absorbs strongly, with a peak at 402 nm, and the concentration is easily calculated through Beer's Law. By removing aliquots at timed intervals, the reaction kinetics can be back calculated. An example of the data is shown in Figure 2.5. UV/Vis is a simple method for quickly and effectively comparing and quantifying the kinetics between different materials.

2.2.5 Infrared Spectroscopy (IR)

Infrared (IR) spectroscopy is a powerful characterization technique that can be used to identify a sample in any state, gas, liquid and solid. IR spectroscopy probes the vibrational energies of a molecule. Because vibrational energy transitions are quantized, each bond will have a unique absorption wavelength allowing for the identification of molecules and interactions. Within this dissertation, IR was primarily used to study the interactions between the CWA/simulant gases and

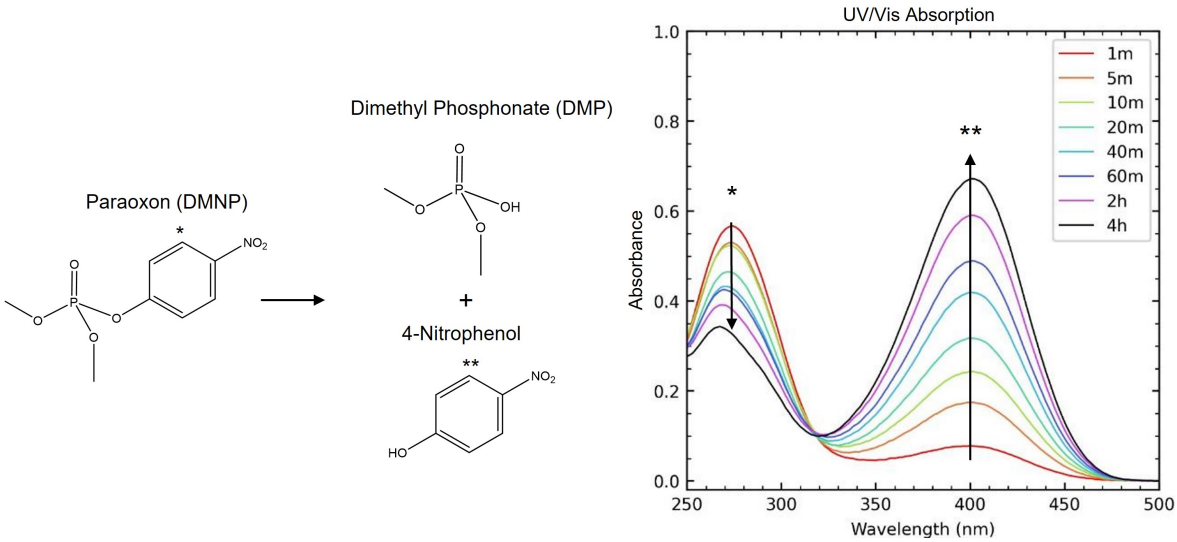


Figure 2.5: Example of the decomposition of methyl paraoxon producing 4-nitrophenol which under basic conditions absorbs strongly at 402 nm

the filtration solid. This section will discuss the basics of IR spectroscopy, and IR techniques including, transmission, attenuated total reflectance (ATR), and diffuse reflectance (Figure 2.8).

Vibrational spectroscopy in the simplest terms can be seen as two masses attached together by a spring. When the molecule vibrates, the spring is stretched and compressed which moves in and out of equilibrium with a certain force constant, defined by Hooke's law in classical mechanics. However, according to quantum mechanics, energy levels are discrete. This behavior led to the development of the harmonic oscillator equation, shown in Equation 2.5.

$$E_v = \frac{h}{2\pi}\sqrt{\frac{k}{\mu}}\left(v+\frac{1}{2}\right) \tag{2.5}$$

However, the internuclear potential energy is not properly modeled with a simple parabola, as the potential energy becomes large at short interatomic distances and closer to zero at large interatomic distances. This leads to Equation 2.6, which is known the anharmonic oscillator.

$$E_v = \omega\left(v+\frac{1}{2}\right) - \omega\chi\left(v+\frac{1}{2}\right)^2 \tag{2.6}$$

Where h is Planck's constant, k is the force constant, μ is the reduced mass, ν is the vibrational energy level. Constants ω and χ are the first and second anharmonicity constants. These two models are shown in Figure 2.6(a). The harmonic oscillator model predicts the energy difference between adjacent states remains equal as you increase vibrational energy levels. In the anharmonic model, energy levels decrease in distance as vibrational energy levels increase which more accurately models a diatomic molecule's vibrational states [105].

Determining the number of possible vibrational modes, each form of molecular movements need to be accounted for. Each atom in a molecule has 3 degrees of freedom within the x, y, z cartesian coordinates, which include vibrations, translations, and rotational movements. Molecules will translate in 3 directions and rotate in 3 directions, which accounts for 6 molecular movements. While linear molecules only contain 2 rotational, as rotating along the primary axis results in no net change. Therefore, there 3N-6 (3N-5 for linear molecules) vibrational modes in a molecule where N is the number of atoms. Although these are the possible vibrations, not all are IR active. A vibration is only IR active if there is a change in dipole moment. For example, the symmetric stretch of carbon dioxide is not IR active, while the asymmetric stretching will be visible in the IR. There are 6 main types of molecular vibrations which are depicted in Figure 2.6(b) [105].

When a molecule becomes adsorbed onto a surface, it is restricted from translational motions and some rotational motions depending on the surface interactions. The restriction of movement is easily seen with the adsorption of carbon monoxide. Gas-phase CO shows rotational energy levels, whereas an adsorbed only has one peak associated with the C≡O vibrations (2143 cm^{-1}). The vibrational mode is affected by the nature of the adsorption. Specifically, the HOMO electrons of CO fill a roughly non-bonding orbital, which are positioned on the carbon. If CO is adsorbed onto an electron poor metal, by accepting of the high energy HOMO electrons, CO will be stabilized resulting in a blue shift in the IR spectrum. Conversely, if the surface is electron rich, the electrons back donate to the π antibonding orbitals decreasing the bond order [106]. CO physisorbed to Cu(II), Cu(I), and Cu(0) has vibrational modes at 2195, 2125 and 2058 cm^{-1} respectively [107].

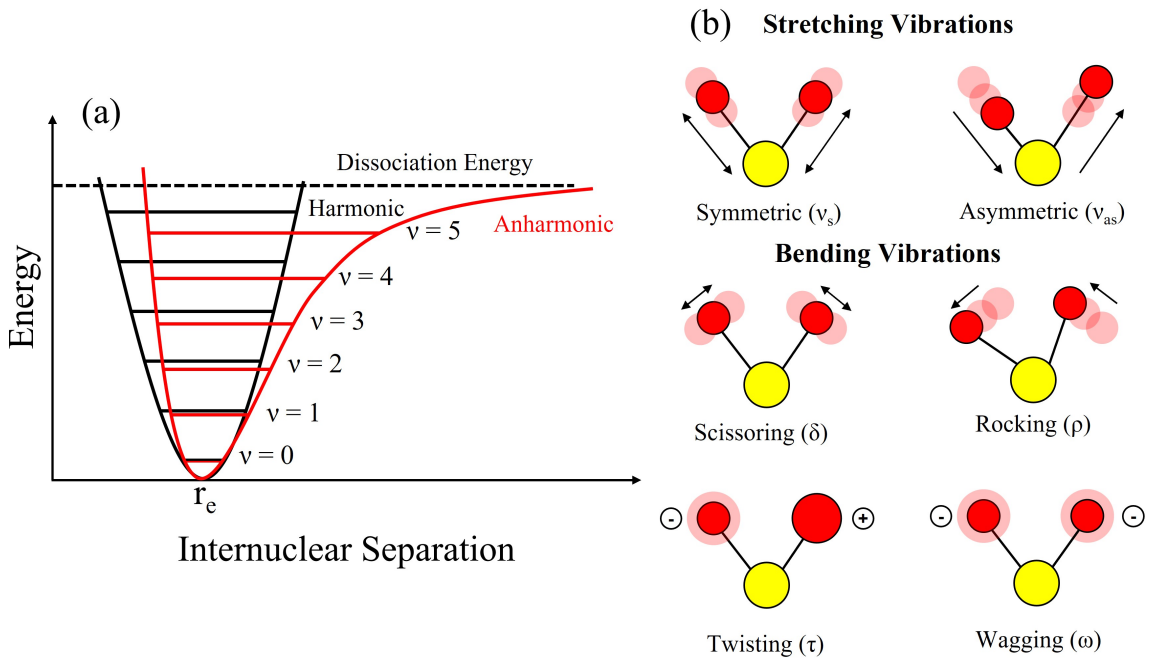


Figure 2.6: Representation of (a) the harmonic and anharmonic oscillator models and (b) common vibrational modes of chemical bonds

The blue shift in vibrational frequencies indicates a strengthening of the bond whereas red shifts indicate a weakening of the bond. With some materials such as CeO_2, CO can be used to distinguish between the crystallographic surfaces (110) and (111) based on the spectral shifts [108]. Shifts in the adsorbed molecules' spectrum provide information about the surface and the molecule.

With organophosphorus molecules, shifts in the spectrum and new modes indicate the adsorption strength and decomposition products. The P=O bond red shifts to a degree that is dependant on the adsorption strength [109]. The larger the red shift, the stronger the adsorption strength. With sarin, the highly electronegative fluorine leaving affects the surrounding bonds. For example, the δ_s(P-CH_3) mode red shifts $\sim$7 cm^{-1} after the fluorine leaves [110]. IR spectroscopy is a powerful tool to study the fundamental interactions in heterogeneous catalysis/reaction studies, to build that molecular understanding to develop better filtration materials.

To study vibrational modes experimentally, the oldest and most simple example is IR transmission spectroscopy. A sample is placed directly in the IR beam, being adsorbed, reflected, and

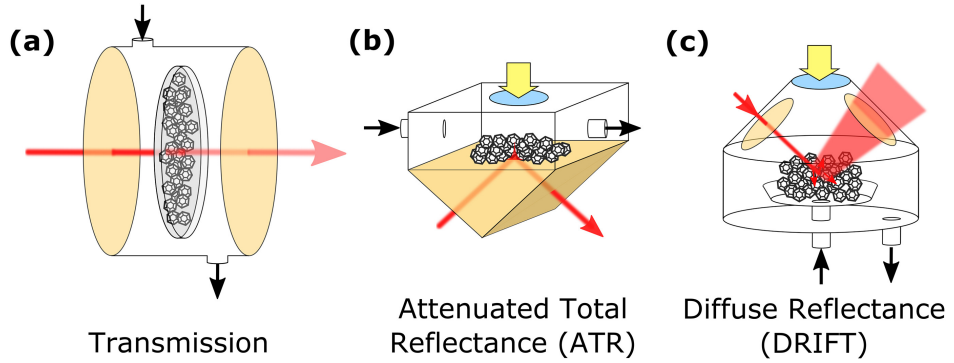


Figure 2.7: Different experimental IR spectroscopy methods (a) transmission, (b) ATR and (c) DRIFTS [111].

transmitted. The light that does not make it to the detector is used for characterization. For studying heterogeneous reactions, a solid sample is mixed in an optically neutral powder, such as KBr, pressed into a pellet and then mounted into a reaction vessel which allows for gas flow, similar to the diagram shown in Figure 2.8(a). In another method, the sample is pressed into a tungsten grid and placed within a high vacuum chamber, discussed further in Section 2.2.5. Transmission IR is beneficial, as the quantification of analyte concentration is typically linear with the concentration. However, transmission IR requires the material to be altered to be held within the beam. Mixing agents such as KBr will physisorb organophosphorus making analysis more difficult [112]. However, the level of control gained with a transmission IR and a high-vacuum system cannot be achieved with the other techniques. Transmission IR was used to study dry CuO nanoparticles with sarin discussed in Chapter 4.

Attenuated total reflectance (ATR), shown in Figure 2.8(b) is a simple method, and can be found in most labs. The sample is pressed onto a reflective crystal, such as ZnSe, Ge or diamond. The IR beam is reflected within the crystal. If the material cannot absorb the light, then the light will continue to reflect. If the beam can interact with the sample, it will be absorbed. The reflected light is known as attenuated or reduced in intensity at the frequencies absorbed by the material [104]. ATR is beneficial as the material does not need to be prepared or altered to be studied. Bulk solvents can easily be incorporated. However, the technique is not surface sensitive, and the IR

beam only interacts with materials that are touching the crystal surface [112].

Diffuse reflectance infrared Fourier transform spectroscopy (DRIFTS) is another common technique to study a material properties and molecular interactions. In DRIFTS, the IR beam is directed to a cup containing the material of interest. When the IR beam reaches the sample, one of two interactions can occur, which is depicted in Figure 2.8. First, the IR beam can reflect off the surface, which is referred to as specular reflection, which carries little to no information about the surface. Different mirror geometries are employed by companies to reduce the specular reflection. Alternatively, the beam enters into the powder, and reflects diffusely throughout the sample. Then, the light will interact with the particles, adsorbing or reflecting internally. The beam will leave the sample and can be collected by mirrors and directed to a detector [113].

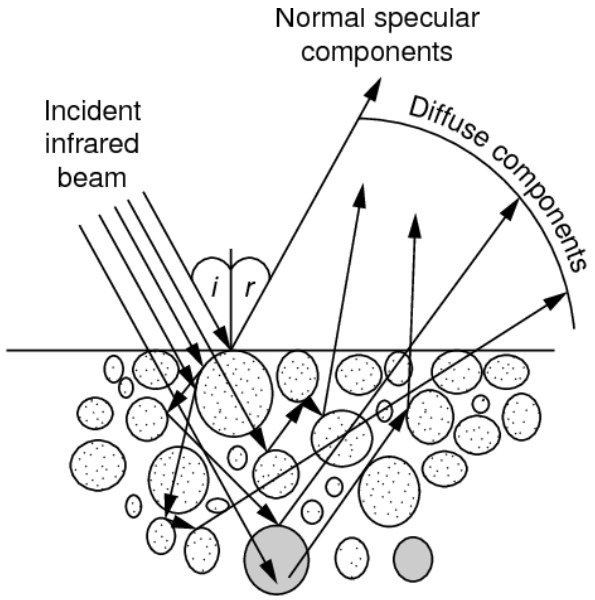


Figure 2.8: Diffuse reflectance infrared Fourier transform spectroscopy (DRIFTS) diagram. The IR will either reflect as specular reflection with little to no surface information or reflect diffusely throughout the sample, adsorbing and giving information on surface species [114].

Companies sell DRIFTS cells that are configured for gas exposure, making DRIFTS a powerful for studying solid gas surface interactions. The technique is surface sensitive and requires little material preparation. Although powerful, since the technique relies on diffuse reflectance. The

path length is unknown, therefore making quantification difficult. Mathematical techniques such as Kubelka-Munk equation are used to quantify molecular concentrations, but have reproducibility issues. DRIFTS also suffers from background drift making analysis difficult [104, 113]. Even with these shortcomings, DRIFTS is a powerful tool in studying the interactions of CWAs and their simulants with metal surfaces. DRIFTS cells can be configured in a variety of ways to probe realistic conditions in a systematic fashion. DRIFTS was used to study mesoporous NiO with the simulant DFP discussed in Chapter 5.

In-Situ DRIFTS Set Up

CAUTION!! CWA simulants are still toxic and carcinogenic. Small exposures can result in health issues or death. Therefore all experiments should be performed with proper safety measures in place including appropriate training, personal protective equipment (PPE), and proper safety equipment. As part of this project, an *in-situ* DRIFTS was built to study the interactions between gas phase molecules and a solid substrate. A picture of the constructed apparatus is shown in Figure 2.9 with a schematic in Chapter 7 in Figure 7.A13. The *in-situ* DRIFTS accessory was purchased from PIKE technologies and mounted on a Thermo Nicolet iS50 FTIR. The optics are gold coated and are constantly purged with dry nitrogen purge to prevent CO_2 and water. The DRIFTS cell used is capable of heating to 500 °C and cooling to -150 °C. The samples within the PIKE DRIFTS cell are held within a porous alumina cup that allows gas to be introduced from either the bottom or the top of the sample.

The carrier gas system was constructed using 1/8" tubing and Swagelok connections. All tubing past the saturator was polyetheretherketone (PEEK) to minimize any interactions between the tubing and the analyte. The carrier gases, He or zero air ($\sim$80% N_2, $\sim$20% O_2), are routed through hydrocarbon and water sieves and controlled with mass flow controllers. The carrier gas is then directed by a bypass valve that allows gases to be directed toward the saturator or bypassed.

The carrier gas can then be directed to the DRIFTS cell or out the rear of the fume hood. This system gives us the control to equilibrate the sample to the carrier gas without risking contamination and to purge the saturator cell prior to exposure. The micro saturator was purchased from glassblowers.com, and allows for a minimal amount of agent or simulant to be handled during experiments. To ensure cleanliness after each experiment the cell and dosing lines are brought to reduced pressures with the attached turbo pump station. The dosing lines are warmed slightly using an incandescent light bulb and the cell is heated to 85 °C through the temperature-controlled water bath.

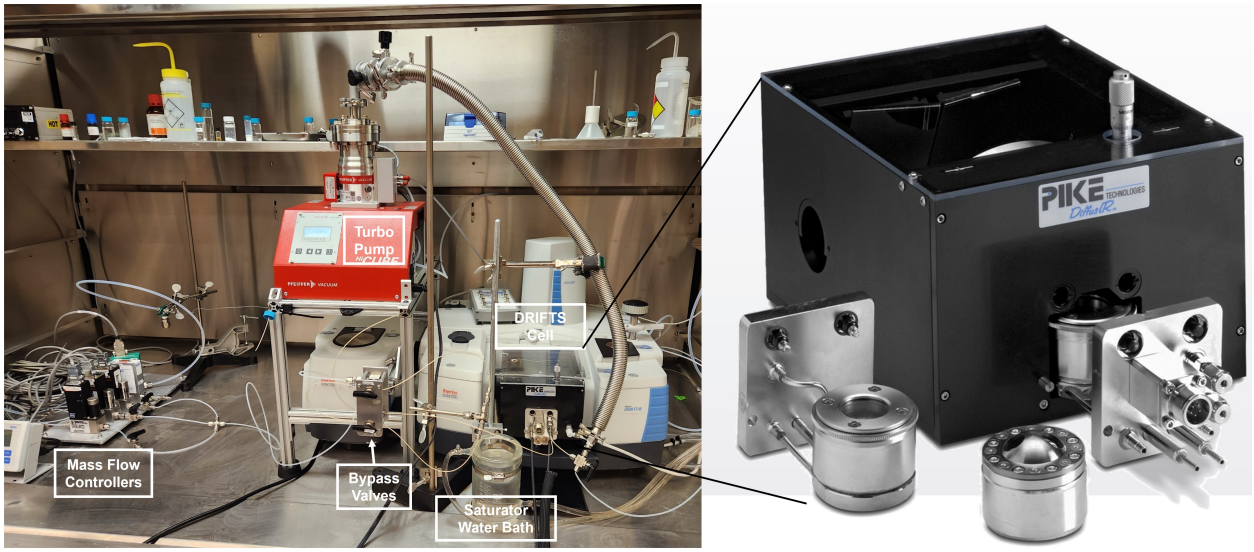


Figure 2.9: DRIFTS system and the PIKE accessory. Image taken from the PIKE DRIFTS accessory brochure.

Mid-Infrared Aerosol Chemistry Chamber (MIRACC)

Developing the next generation filtration materials requires a fundamental knowledge of how the gas molecules interact with the material's surface. By taking a complex chemical environment and breaking it down into individual components, we can begin to understand the important factors in CWA decomposition. Ultra-high vacuum (UHV) chambers have revolutionized the field of

surface science allowing for the complete control of a material's environment. As part of a separate Defense Threat Reduction Agency (DTRA) project, the mid-infrared aerosol chemistry chamber (MIRACC) was constructed at the Chemical Biological Center (CBC) specifically to perform these fundamental studies with CWAs and their simulants, shown in Figure 2.10 [115].

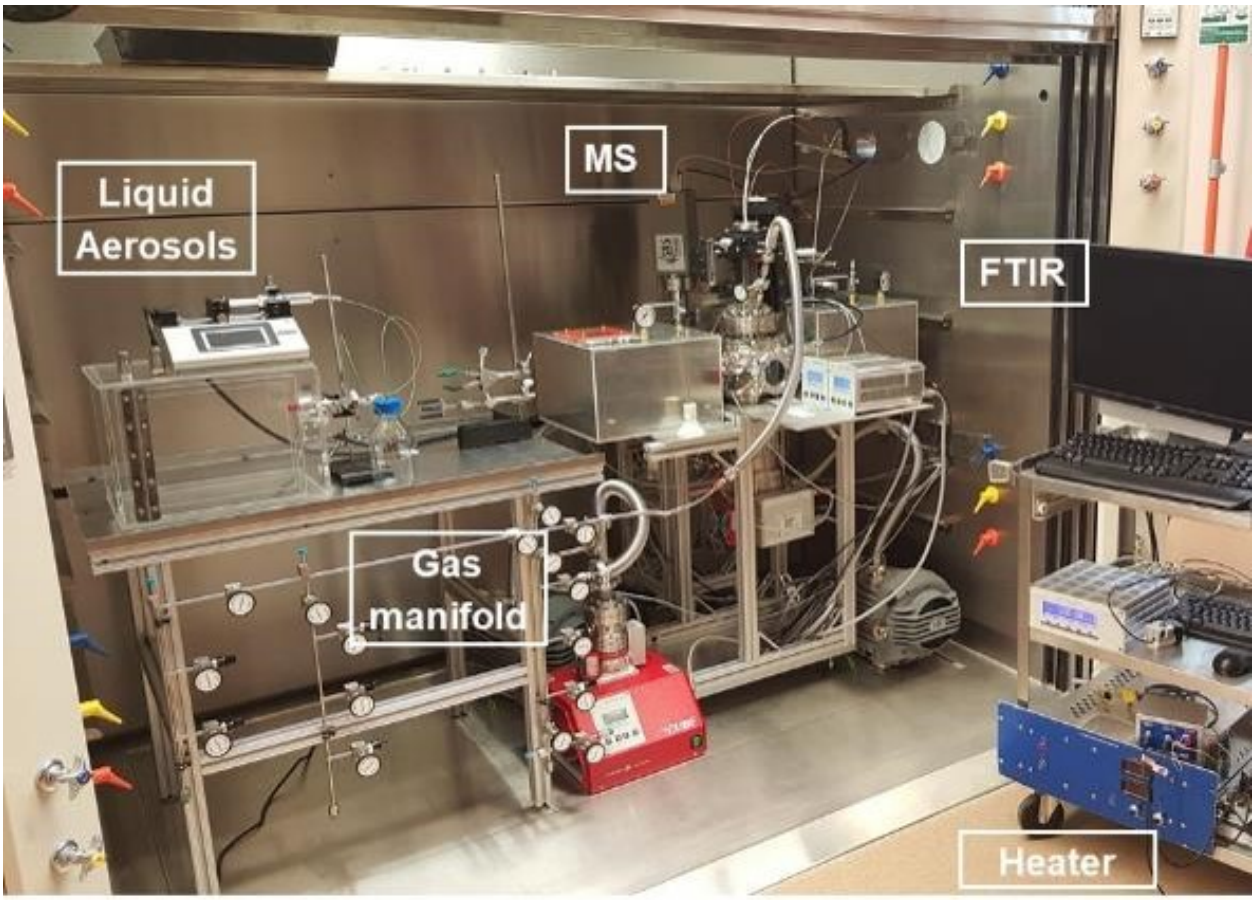


Figure 2.10: Mid-infrared aerosol chemistry chamber (MIRACC)

The MIRACC is discussed in greater detail in Reference [115]. Briefly the chamber is equipped with two characterization instruments: transmission IR spectrometer and a residual gas analyzer (RGA). The main chamber and RGA chamber are equipped with a magnetically levitated molecular pump (400 L/s Pfeiffer vacuum) with a manual gate valve separating the main chamber. This setup allows the main chamber to operate at pressures from 1×10^{-9} Torr to 100 Torr. The introduction of gases is controlled through two manifolds. The main manifold controls the introduction

of non-toxic gases, and the secondary manifold handles all CWAs. The main manifold has multiple Swagelok and VCR connections, all isolated by Swagelok needle valves and backed by an Edwards scroll pump. This set up allows for the controlled release of any desired gases, e.g. N_2, O_2, H_2O, CO, CO_2. The second dosing line has one VCR connection, with two Swagelok needle valves on both sides. This line is connected to the main chamber through a high-precision leak valve.

Samples are pressed into a tungsten grid and held by a custom stainless steel mount depicted in Figure 2.11. The temperature is controlled through the copper wires attached to the sample holder and is monitored through a K-type thermocouple welded directly to the tungsten grid. The copper rods are attached to a 50 amp power supply, which is used for restive heating up to $\sim$1000 K. The sample is cooled to $\sim$100 K using inductive colling with liquid nitrogen. Within the chamber, the sample is controlled by a manipulator capable of moving in the x, y and z directions for precise alignment with the IR beam.

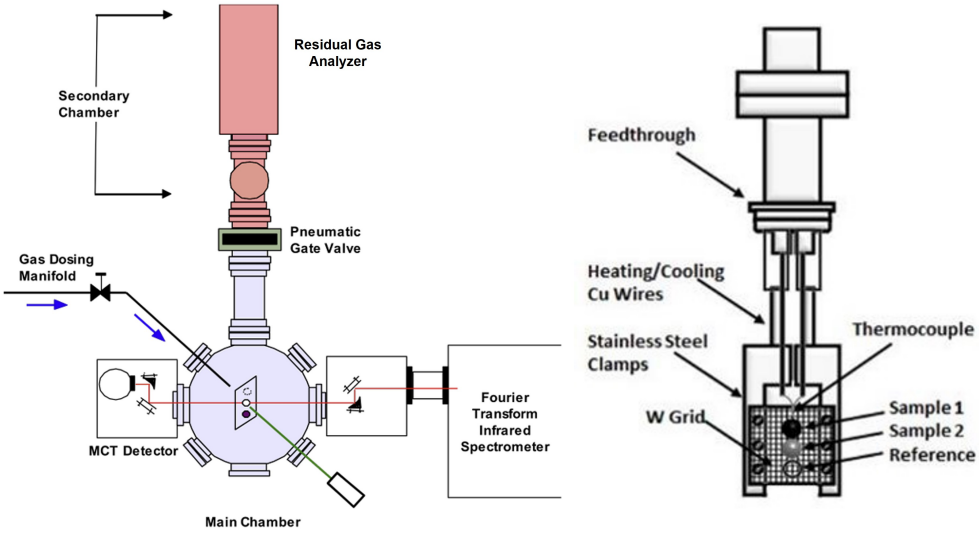


Figure 2.11: Mid-infrared aerosol chemistry chamber (MIRACC) instrumental diagram (left) and sample holder (right).

Chapter 3: Spectroscopic Studies of Methyl Paraoxon Decomposition over Mesoporous Ce-doped Titanias for Toxic Chemical Filtration

The results presented in this chapter have been previously published in: Leonard, M. B.; Li, T.; Kramer, M. J.; McDonnell, S. M.; Vedernikov, A. N.; Rodriguez, E. E. Spectroscopic Studies of Methyl Paraoxon Decomposition over Mesoporous Ce-Doped Titanias for Toxic Chemical Filtration. Journal of Hazardous Materials 2022, 438, 129536. Tianyu Li was responsible for sample synthesis. Matthew Leonard was responsible for materials characterization, decomposition kinetic measurements, analysis and the manuscript draft. Morgan Kramer contributed to the manuscript and collected mass spectrometry data. Shannon McDonnell contributed to the manuscript and assisted in the development of the testing plan. Andrei Vedernikov contributed to the manuscript and Efrain Rodriguez is the corresponding author.

3.1 Introduction

Chemical warfare agents (CWAs) first arose as a major threat during World War I, and remain a prevalent threat today. The Geneva Convention has prohibited the use of CWAs since 1925, because these chemical are indiscriminate and lethal. Sadly, various terrorist organizations do not adhere to these laws. CWAs have been used as recently as 2013 with a single attack killing more than 1,000 civilians [8, 116]. Some of the deadliest CWAs are organophosphorus molecules, such as sarin (GB) and soman (GD), shown in Figure 3.1, which disrupt the nervous system by covalently bonding to the enzyme acetylcholinesterase [117]. Over the years, organophosphorus

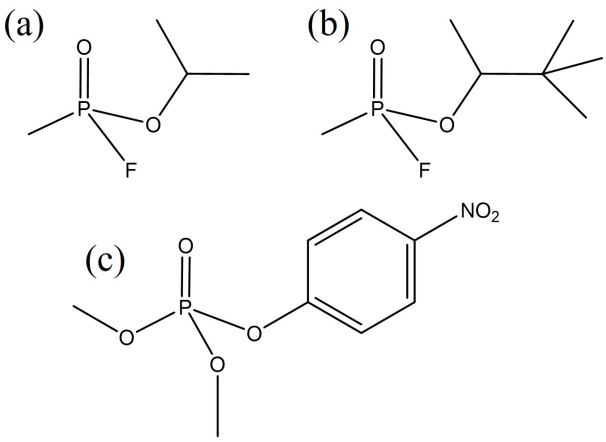


Figure 3.1: Molecular structures of various chemical warfare agents (CWAs) plus that of a simulant molecule. The CWA a) Sarin (GB), b) Soman (GD) and c) the simulant used in the present study, methyl paraoxon.

molecules that are less toxic have also been used as plasticizers, flame retardants and pesticides. However, serious health effects were later linked to the use of these less toxic compounds[11, 61, 118]. Research into the adsorption and decomposition of organophosphorus molecules are pivotal for both public health and environmental safety.

Composite solid materials, such as carbon/metal oxides, can be integrated into chemically resistant suits and mask filters to protect from CWA exposure. The carbon support's primary function is to physisorb CWAs and bind them weakly. The metal oxides perform the chemistry to either chemisorb or degrade the CWAs. A key component of such composite structures is bituminous coal based (BPL) carbon, which is a microporous material with a pore size less than 1.7 nm and a high specific surface area ($\approx$850 m^2/g). The loaded metals, known as ASZM-T, consist of a mixture that includes copper (A), silver (S), zinc (Z), and molybdenum (M), along with the ligand triethylenediamine (T). Although BPL ASZM-T has a wide range of reactivity, the basic components of this composite have not significantly changed over the last 50 years [11, 116].

In an effort to improve CWA filtration, metal oxides have been studied over the years with various CWAs and simulants [50, 57, 60, 61, 64, 67, 72, 73, 118–121], showing reactivity in different

forms and environments. To maintain the high surface area of BPL and increase reactivity, these filtration materials can be formed as mesoporous metal oxides (MMOs). Since their inception, mesoporous materials have shown benefits across many fields [98, 122]. However, when studying CWA decomposition, it is not practical to work with live agents such as sarin and soman in an academic setting. Therefore, a common simulant to study similar reactivity and decomposition is dimethyl 4-nitrophenyl phosphate (DMNP), commonly referred to as methyl paraoxon Figure 3.1c. Methyl paraoxon shares multiple similarities to sarin and soman but lacks the highly toxic P-F bond, and have shown in literature to have similar kinetics and reactivity [21, 22]. Metal oxides such as CeO_2 [56, 78, 123, 124], MgO [78, 125, 126], TiO_2 [37, 78], ZrO_2 [78] and ZnO [78], typically in the form of nanoparticles, have been previously tested with methyl paraoxon. Because CeO_2 and TiO_2 have previously demonstrated high reactivity [78], we have therefore selected these materials for our study.

Cerium and titanium oxide have attractive properties for CWA defeat including the presence of Lewis and Brønsted acid sites and a low redox potential between their +4 and +3 states. To charge balance the potential multivalent states, oxygen vacancies form in the lattice, resulting in potential high reactivity in catalytic and non-catalytic reactions [127, 128]. We seek to isolate the most important parameters for boosting the reactivity of the metal oxides surfaces for methyl paraoxon decomposition. In doing so, a key question is how much of a role the nature of the metal cation plays in the decomposition and kinetics. To answer this question, we focus on isovalent substitution of Ce^{4+} for Ti^{4+} into TiO_2, to show the effects of this substitution on methyl paraoxon reactivity. Throughout the rest of this chapter, we refer to such isovalent substitution as doping.

Within this work, we show that an ordered mesoporous $Ce_xTi_{1-x}O_2$ with high surface area can be synthesized using a soft templating method, while avoiding crystallographic phase separation for $x \leq 0.15$. This solid solution along with synthesized mesoporous TiO_2 [129, 130] and CeO_2 [131, 132], were fully characterized from the bulk material to the surface structure. We then reacted the MMOs with methyl paraoxon in a propanol environment to measure the decomposition kinetics

and determine the products. Pure CeO_2 is the most reactive material in our study, with a surface area normalized rate constant (k_{SA}) that is 3 to 4.6 times larger than the other MMOs studied.

3.2 Experimental Section

3.2.1 Synthesis of Mesoporous TiO_2 and Ce-doped TiO_2

Mesoporous TiO_2 was synthesized via a reported evaporation-induced self-assembly (EISA) method [129, 130]. Typically, 1.0 g of the triblock copolymer Pluronic F127 was first added into 15 mL of anhydrous ethanol, followed by the addition of 1.5 g glacial acetic acid and 1.5 g concentrated hydrochloric acid (HCl 37%). After stirring for 0.5 h at room temperature, 25 mmol ($\approx$ 8 ml) titanium isopropoxide ($Ti(OCH(CH_3)_2)_4$) was added to the solution dropwise. The solution was stirred vigorously for approximately 3 h. The resulting sol solution was then transferred into an open glass container (diameter 2 in) and heated to 40 °C for 24 h, then to 60 °C for 24 h. The evaporation of the solvent leads to the formation of a gel. Mesoporous TiO_2 powder was obtained by calcinating the gel at 350 °C for 4 h (1 °C/min ramp rate) in air. For the synthesis of the $Ce_xTi_{1-x}O_2$ series, the same procedure was used except with the appropriate stoichiometric ratios of titanium isopropoxide ($Ti(OCH(CH_3)_2)_4$) to $Ce(NO_3)_3{\cdot}6H_2O$.

3.2.2 Synthesis of Mesoporous CeO_2

Mesoporous CeO_2 was synthesized via a nanocasting method [131, 132]. The silica template KIT-6 was first prepared via a reported method [95], 85 °C was used as the aging temperature during the KIT-6 synthesis. In a typical synthesis of mesoporous CeO_2, we dispersed 0.5 g of as-prepared KIT-6 silica in 20.0 mL of 95% ethanol. Then 1.362 g of $Ce(NO_3)_3{\cdot}6H_2O$ was dissolved in the same solution. The mixture was stirred at room temperature until all the solvents evaporated and the mixture became a dry powder. The powder was later transferred to a glass vial (diameter

$\sim$5 mm) and calcinated at 560 °C for 6 h (ramp rate 1 °C/min). $Ce(NO_3)_3{\cdot}6H_2O$ decomposes to CeO_2 during the calcination step. To fully remove the silica template, the CeO_2/KIT-6 composite was soaked in 2 M NaOH solution 3 times at 80 °C for 12 h. After being washed 3 times with distilled water and twice with ethanol, the final mesoporous CeO_2 product was dried in air at 80 °C overnight and then at 150 °C for an additional day.

3.2.3 Bulk and Surface Characterization

Transmission electron microscope (TEM) images were obtained on a JOEL-2100 LaB_6 TEM with an accelerating voltage of 200 kV and a beam current of 104 μA. All samples were dispersed in ethanol and drop cast onto a lacey carbon 200-mesh copper or gold grid. Scanning electron microscope (SEM) images were obtained using a Hitachi SU-70 Field Emission SEM equipped with a Bruker energy dispersive spectroscopy (EDS) detection model: Flash 6T/60 with a silicon drift detection (no Li dopant) and solid angle of 0.189 sr.

Powder x-ray diffraction (XRD) patterns were collected using a Bruker X-ray diffractometer with a Cu Kα radiation (λ=1.5406 Å) and a LynxEye position-sensitive detector. Rietveld refinements was performed using GSAS II [133]. Small-angle x-ray scattering (SAXS) patterns were collected using a Xenocs Xeuss SAXS/WAXS/GISAXS system. Nitrogen adsorption isotherms were recorded with a Micrometrics ASAP 2020 Porosimeter. Samples were degassed in vacuum at 150 °C for 6 h prior to characterization. The surface area was determined using the Brunauer-Emmett-Teller (BET) method with a relative pressure range (*P/Po*) of 0.05-0.30. Pore size and volumes were calculated from the adsorption branch using the Barrett, Joyner, and Halenda (BJH) method. TGA measurements were performed using a Mettler Tolledo TGA/DSC 2 STAR System. Samples were placed in the TGA and degassed under argon flow for 18 h to remove anything loosely bound to the surface, then were heated to 500 °C at 5 °C/min. With pyridine adsorption, approximately 20mg of sample were placed into an open dram vial. The vials were then placed

into a sealed jar with an open vial pyridine for 1 week at room temperature. Samples were removed from the jar and placed on the lab counter to air dry for 1 hour [82, 134], and then tested using the same set up as the *ex-situ* measurements outlined in 3.2.6.

3.2.4 Methyl Paraoxon Testing Procedures

Methyl paraoxon degradation testing procedures from prior work were followed [37, 78, 135, 136], with a slight modification. Methyl paraoxon was used in excess to available surface sites to probe catalytic activity. For each test, approximately 20 mg of the metal oxide was degassed under nitrogen flow for 24 h to remove any loosely bound gases. After re-weighing, the samples were placed in a dram vial with 1 mL of 2-propanol. The samples stirred at 600 rpm for 30 min. Then, 7 μL of a 2 M solution of methyl paraoxon/acetone was added. 20 μL aliquots were taken at 1 min, 5 min, 10 min, 20 min, 40 min, 1 h, 2 h and 4 h and then dispersed in 5 mL of 0.1 M 4-ethylmorpholine (pH 10) to quench the reaction and deprotonate 4-nitrophenol, which absorbs at 402 nm and was tracked through UV/Vis. 4-ethylmorpholine solutions were chilled prior to quenching and stored in a refrigerator until testing to prevent any further reaction. A blank was run with aliquots removed at 5 min and 4 h, and used to account for any background decomposition of methyl paraoxon.

3.2.5 UV-Vis Absorption Measurements

Beer's law was used to calculate the concentration of 4-nitrophenol using a molar absorptivity ε = 18330 $M^{-1}cm^{-1}$ at 402 nm. Absorption spectra were collected on a Shimadzu UV-Visible 2401PC Spectrophotometer from 190 - 820 nm with 1 nm point spacing. To limit scattering by suspended particles during absorption measurements, the samples were centrifuged at 6000 rpm for 5 min, and the supernatant was pipetted off for testing. Absorption was collected in a 1 cm quartz cuvette. To account for solvent absorption, pure 0.1 M 4-ethylmorpholine was measured

and subtracted from all spectrums. The data was also baseline corrected by subtracting the average absorbance value from 650 nm to 640 nm, where the absorbance should be zero, from each individual absorbance value.

3.2.6 *Ex-situ* DRIFTS measurements

Samples were prepared as outlined above, but reacted for 24 h. After vacuum filtration, the samples were rinsed with excess 2-propanol to remove any loosely bound molecules. DRIFTS measurements were preformed using a Thermo Nicolet 6700 FTIR spectrometer with a Harrick Scientific Praying Mantis DRA optical accessory. Each IR spectrum has an average of 256 interferograms with a resolution of 2 cm^{-1}. The un-dosed metal oxide was scanned in the same manner and used to subtract the background from the methyl paraoxon dosed metal oxide spectra. For pyridine adsorption experiments, approximately 20 mg of sample were placed into an open dram vial. The vials were then placed into a sealed jar with an open vial of pyridine for 1 week at room temperature. Samples were removed from the jar and placed on the lab counter to air dry for 1 h [82, 134].

3.2.7 Mass Spectrometry

High resolution mass spectra were recorded on a JEOL AccuTOF ESI-MS. All sample aliquots were taken at 5 m and 4 h, then dispersed in 0.1 M 4-ethylmorpholine. Then, we introduced the samples into the MS via an HPLC line containing a H_2O/MeOH mobile phase.

3.3 Results and Discussion

3.3.1 Bulk characterization

To understand changes in methyl paraoxon's reactivity, we first characterized the structures of our MMOs. An important aspect of any metal oxide's properties is its crystal structure. To probe the crystal structure, we obtained powder XRD patterns, shown in Figure 3.2. Due to the small crystalline walls of mesoporous materials, all diffraction patterns exhibit peak broadening. The crystallite sizes were estimated through Rietveld refinements and are shown in Table 3.1. From our synthetic procedure, the mesoporous TiO_2 crystallizes in the anatase phase (tetragonal lattice) and remains anatase throughout doping, with no visible phase separation into TiO_2 and CeO_2. However, as the doping increases, the crystallinity decreases. This trend is expected, as higher doping affects the crystallization process until we reach the solubility limit for Ce in the anatase phase, which was approximately 15% from our synthesis. Lattice constants are not reported, because the decreased crystallinity reduces the value's reliability. Mesoporous CeO_2 is crystalline and adopts the fluorite (cubic)-type structure.

Table 3.1: Average crystallite size for the MMOs TiO_2, $Ce_xTi_{1-x}O_2$ and CeO_2 through Rietveld refinement using the Debye-Scherrer formula.

Material	**TiO_2**	**x=0.5%**	**x=5%**	**x=10%**	**x=15%**	**CeO_2**
Crystal Size (nm)	12	11.89	7.8	7	5.3	10.4

TiO_2 and $Ce_xTi_{1-x}O_2$ were synthesized using a soft templating. Ordered cylindrical pores are clearly seen in the TEM images, shown in Figure 3.3, for both TiO_2 and $Ce_xTi_{1-x}O_2$, which has not been reported previously at such high doping levels of Ce in the TiO_2 anatase phase. CeO_2 was not prepared with hexagonally packed pores, due to the need for a hard templating synthesis method. The TEM image shows the typical shape of samples templated with KIT-6. The samples were also analyzed using SAXS to determine whether the samples exhibit long-range order in

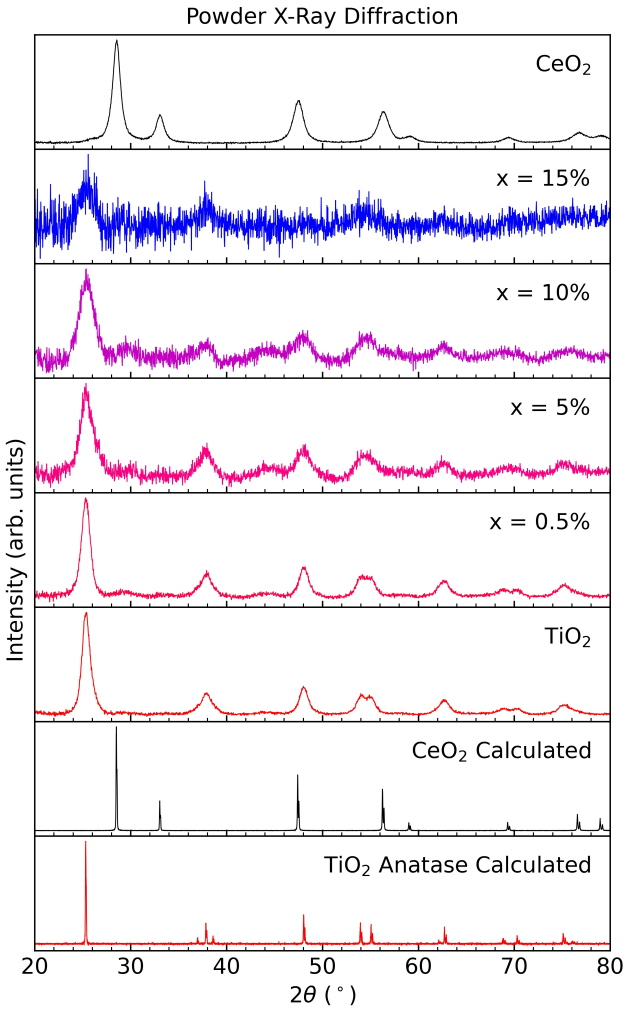


Figure 3.2: Powder X-ray diffraction patterns of MMOs, including TiO_2, the $Ce_xTi_{1-x}O_2$ series and CeO_2. The calculated patterns are shown for comparison. The $Ce_xTi_{1-x}O_2$ MMOs retain the anatase-type structure throughout doping, although crystallinity clearly decreases at higher doping concentrations.

their mesoporous structure. The SAXS patterns can be seen in Figure 3.4. Each sample exhibited a single broad peak, and without additional high angle peaks, we cannot confirm the structure from SAXS alone. However, with the TEM images, we see that TiO_2 and the $Ce_xTi_{1-x}O_2$ series have hexagonally packed (p6mm) pores, so we can assign the main peak to the (100) reflection. Because CeO_2 is KIT-6 templated ($Ia\bar{3}d$), the main peak corresponds to the (211) reflection.

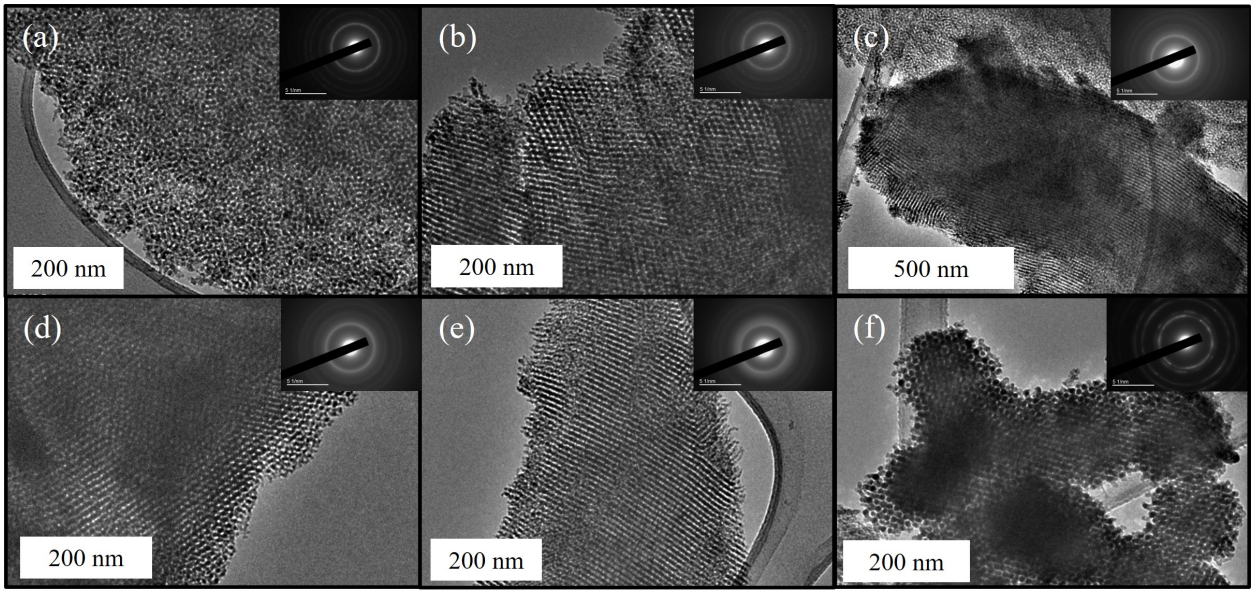


Figure 3.3: Transmission electron microscopy and diffraction patterns of MMOs in this study. The TEM images correspond to those of a) TiO_2, $Ce_xTi_{1-x}O_2$ b) x = 0.5%, c) x = 5%, d) x = 10%, e) x = 15% and f) CeO_2. TiO_2 and $Ce_xTi_{1-x}O_2$ have ordered cylindrical pores, whereas CeO_2 has the reverse structure of KIT-6.

3.3.2 Surface characterization

Nitrogen adsorption isotherms and the pore size distribution are shown in Figure 3.5 and the summarized data in Table 3.2. All the synthesized materials maintained a high specific surface area (176 to 252 m^2/g), with a peak pore size of 6.5 to 8 nm. From the N_2 isotherms, TiO_2 and $Ce_xTi_{1-x}O_2$ (x = 0.005 and 0.05) exhibited a H1 hysteresis typical of cylindrical pores. Samples $Ce_xTi_{1-x}O_2$ (x = 0.10 and 0.15) exhibit a combination of an H1 and H2 hysteresis, showing that at higher doping the pore structure is altered. Most likely, the cylindrical pores have narrowed regions ("bottle neck") causing the H2 hysteresis. CeO_2 was templated using KIT-6, and exhibited a specific surface area of 101.92 m^2/g and a peak pore size of 3.78 nm.

To understand more about the surface, and how surface changes affect reactivity with methyl paraoxon, IR absorption experiments can be employed. Specifically, for surface acidity, pyridine adsorption studies can determine whether the metal oxide has Lewis-acid species (LPy) at metal

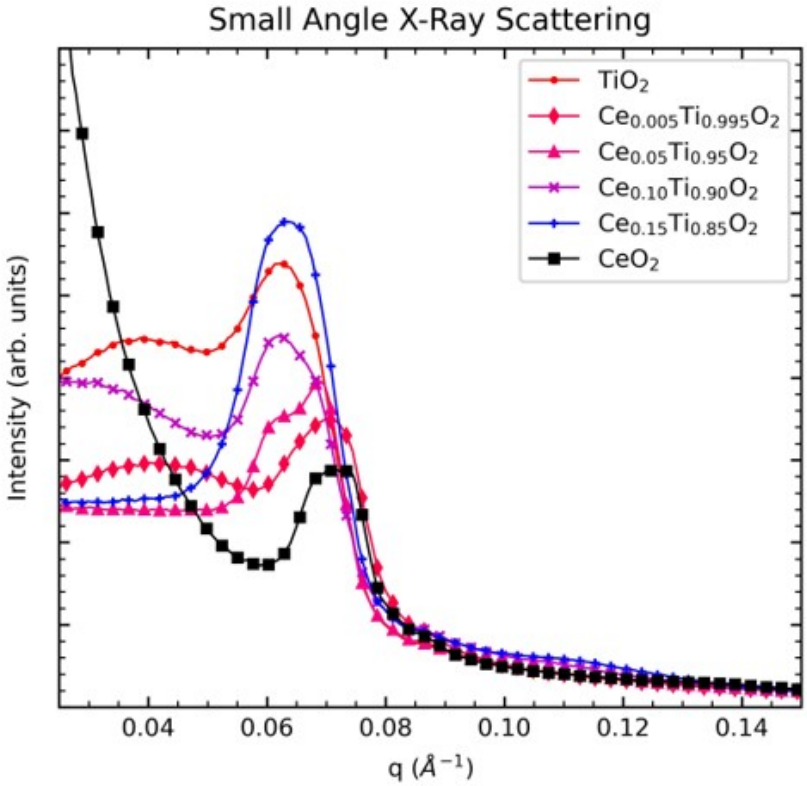


Figure 3.4: Small angle X-ray scattering (SAXS) data for TiO_2, $Ce_xTi_{1-x}O_2$ ($0.005 \leq x \leq 0.15$) and CeO_2 showing a repeating structure. Due to the single broad peak, direct structural assignments are not possible from SAXS alone. With the aid of TEM, TiO_2 and Ce-doped series has been determined to contain hexagonally packed pores making the first peak (100). CeO_2 is KIT-6 templated, making the first peak the (211).

Table 3.2: A summary of characteristics for each MMO as obtained from N2 adsorption measurements.

Material	**Surface Area (m^2/g)**	**Peak Pore Size (nm)**	**Pore Volume (cm^3/g)**
TiO_2	176.31	7.34	0.27
$Ce_{0.005}Ti_{0.995}O_2$	214.23	6.66	0.31
$Ce_{0.05}Ti_{0.95}O_2$	252.61	6.67	0.30
$Ce_{0.10}Ti_{0.90}O_2$	224.46	7.94	0.34
$Ce_{0.15}Ti_{0.85}O_2$	209.41	7.91	0.32
CeO_2	101.92	3.78	0.23

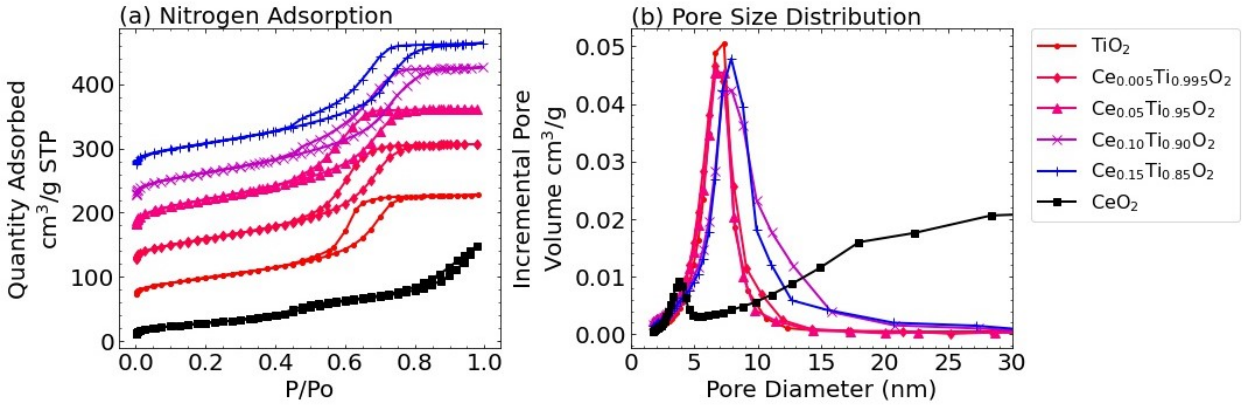


Figure 3.5: Gas adsorption measurements to obtain surface areas and porosity. In a) N2 isotherms of TiO_2, CeO_2 and $Ce_xTi_{1-x}O_2$. For clarity, the isotherms (0.5, 5, 10, and 15 %) was offset by 50, 100, 150 and 200 cm^3/g respectively. The $Ce_xTi_{1-x}O_2$ (x = 0.5%, 5%) isotherms exhibit H1-type hysteresis, whereas $Ce_xTi_{1-x}O_2$ (x = 10%, 15%) exhibits a mix of H1 and H2-type hysteresis. b) The BJH pore size distribution for the MMO samples.

center sites and Brønsted-acid species (BPy) at surface hydroxyl sites. Our pyridine studies sought to determine the relative ratio of these two types of acidic species, and therefore the concentration of active sites, via IR absorption bands, which we assigned based on previous literature [134, 137–140]. Figure 3.6 shows the difference IR spectrum for each MMO. The main LPy peaks are easily identified through the ν8a and ν19b (C-C-N) bands between 1630 and 1600 cm^{-1} and 1465 and 1445 cm^{-1}, respectively. A higher frequency corresponds to stronger Lewis acidity. The main BPy peaks are identified from their ν8a and ν19b bands at 1640 to 1630 cm^{-1} and 1540 to 1500 cm^{-1}, respectively. Other LPy and BPy vibrations are observed outside of these ranges, and will be discussed below.

Pyridine adsorbed onto TiO_2 consisted of several clear LPy species from the peaks observed at 1605, 1576 and 1445 cm^{-1}, whereas pyridine on CeO_2 consisted of only 2 LPy species at 1598 and 1443 cm^{-1}. These pyridine adsorption modes show that both surfaces have Lewis acid sites with TiO_2 having more strongly acidic sites than CeO_2. Both TiO_2 and CeO_2 exhibited a peak, at 1491 and 1485 cm^{-1}, respectively, attributed a site that exhibits both LPy and BPy characteristics. The main difference between the two MMOs is the peak at 1594 cm^{-1}, which is only seen in TiO_2

we attributed this peak to hydrogen bonded pyridine (HPy).

For the doped series $Ce_xTi_{1-x}O_2$ (x = 0.005, 0.05, 0.1, 0.15), the pyridine adsorption studies revealed spectra that combine features of those of pure TiO_2 and CeO_2. This result demonstrates that in the doped series, cerium atoms must be present on the surface to contribute to the spectra. The main vibrations on TiO_2 at 1605 and 1445 cm^{-1} (of LPy character) and at 1491 cm^{-1} (of BPy/LPy character) broaden and form a shoulder. This shoulder at lower frequency we assign to Ce sites. In addition, a peak appears at 1580 cm^{-1} which we assign to an HPy species. Based on the normalized TGA data in Figure 3.7 the doped series lost more weight upon heating above 100 °C than did pure TiO_2 did, which suggests that additional hydroxyl surface sites are formed in the doped series, resulting in the new HPy peak.

3.3.3 Methyl Paraoxon Decomposition

Decomposition experiments were performed in propanol, to be similar to previous metal oxide experiments in the literature [78, 135, 136, 141–143]. To understand the MMO surfaces under testing conditions, we stirred the samples in propanol, filtered them, and analyzed them by DRIFTS. The resultant IR spectra is shown in Figure 7.A1. All MMOs saw a decrease in the hydroxyl stretch region 3600-3700 cm^{-1}, which is consistent with previous literature [110]. The remaining peaks are associated with propanol physisorbed to the surface, so that when we compare the spectra for different MMOs, their surfaces will contain minimal hydroxyl groups.

In studying the decomposition of methyl paraoxon on these MMOs, we employ two useful metrics. The first is the percentage of methyl paraoxon decomposed, which reveals the most reactive materials by weight. The second the amount decomposed normalized by surface area, which elucidates dopant effects on decomposition. Figure 3.8a shows the decomposition of methyl paraoxon as a percentage of the simulant dosed. Each MMO was dosed with excess methyl paraoxon, but never reached 100% decomposition. With metal oxides, catalytic decomposition of CWAs is not

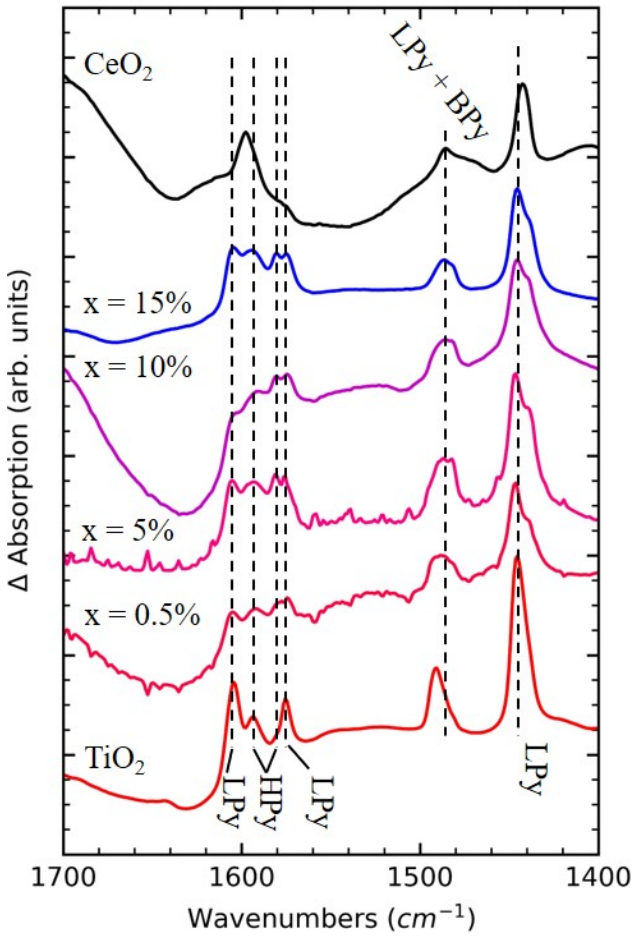


Figure 3.6: DRIFTS spectra of pyridine adsorption on MMOs. The Lewis (LPy) and Brønsted (BPy) acid sites were identified on TiO_2 $Ce_xTi_{1-x}O_2$ and CeO_2 at room temperature. $Ce_xTi_{1-x}O_2$ MMOs contained sites consistent with the presence of both titanium and cerium atoms.

common in a neutral environment; therefore, this result was expected. Spectroscopic techniques were used to determine the products remaining on the surface, as will be discussed below. Non-normalized MMOs show that as the Ce dopant concentration increases in titania, the kinetics remains similar, but the total methyl paraoxon decomposed increases. This observation suggests that the methyl paraoxon interacts with the Ti^{4+} cation first. Conversely, CeO_2 has faster kinetics, but the reactivity drops off after 1 h. $Ce_{0.15}Ti_{0.85}O_2$ is the most reactive MMO studied here, decomposing an additional 16% of methyl paraoxon compared to undoped TiO_2 and CeO_2.

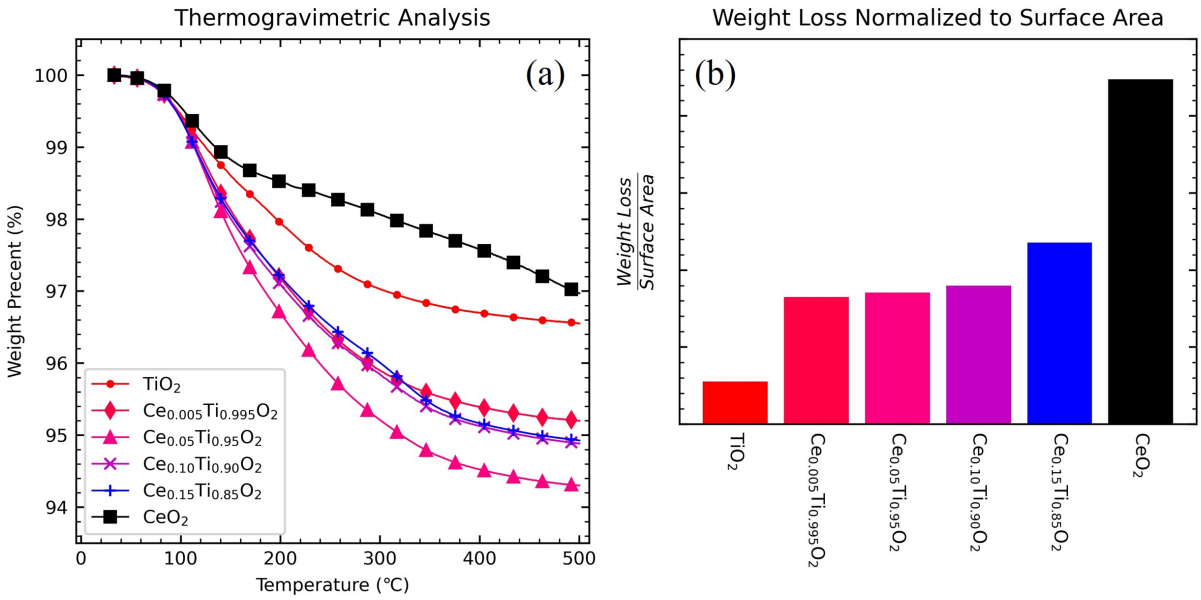


Figure 3.7: a) Thermogravimetric analysis (TGA) curve for TiO_2, $Ce_xTi_{1-x}O_2$ and CeO_2. b) Amount of weight loss divided by surface area. Normalized weight loss shows that as the material has more cerium more hydroxyl groups are created.

To understand the dopant effects from a fundamental perspective, the data is normalized to the MMO's surface areas. Because reactions only occur on the surface of these bulk MMOs, normalizing the total decomposition and reaction kinetics to their surface area allows us to assess the differences in reactivity more accurately. The amount of 4-nitrophenol decomposed from methyl paraoxon was divided by the MMO surface area. Figure 3.8b shows the normalized moles of product as a function of time. We calculated the decomposition rate constants (k_o) using pseudo-first-order kinetics for the first 10 min of reactivity. Because excess paraoxon was used in this experiment the first 10 min kept surface coverage low and within pseudo first order kinetics. Past this range, molecules bound to the surface, which will be discussed below, the concentration of the surface no longer negligible. Decomposition rates k_o were then divided by surface area to obtain the surface-area-normalized rate constant (k_{SA}). All kinetic values are consolidated in Table 3.3. Between TiO_2 and the $Ce_xTi_{1-x}O_2$ series for $x = 0.5\%$, 5%, and 10%, there is little variation in the

values for k_o, k_{SA} and total reactivity (after 4 h) as a function of dopant concentration. The outlier was the x = 15% sample, $Ce_{0.15}Ti_{0.85}O_2$, which exhibited a k_{SA} that is 1.1 to 1.6 times larger than TiO_2 and $Ce_xTi_{1-x}O_2$. The x = 15% sample also displayed an overall increase in methyl paraoxon decomposition. Finally, CeO_2 was the most reactive with a k_{SA} between 3 to 4.6 times larger than those of the titania MMOs. The lack of change in Ce-doped titanias reactivity demonstrates that factors other than doping must play a greater role in methyl paraoxon decomposition, which we discuss next.

Through our pyridine adsorption studies, we inferred that the concentration of cerium sites available on the surface of $Ce_xTi_{1-x}O_2$ will proportionally either increase or decrease surface reactivity, if the concentration is indeed metal cation dependent. Our synthetic procedures ensured an oxygen rich environment, to prevent aliovalent dopant and oxygen vacancies, and to focus on isovalent effects. However, we found little to no change between TiO_2 and $Ce_xTi_{1-x}O_2$ for $x <$ 15%, suggesting that factors other than the Ti^{4+} or Ce^{4+} cation concentration are important for methyl paraoxon decomposition. We note that because the MMOs are mostly dehydrated, only physisorbed propanol would be restricting methyl paraoxon from reacting with the surface. Therefore, an important factor to now consider is crystallographic structure. CeO_2 has the fluorite-type (cubic) structure while TiO_2 adopts the anatase-type (tetragonal) structure. Ce-doping clearly reduces long-range order and at the higher dopant levels the surface could also favor certain crystallographic planes that are more reactive for methyl paraoxon decomposition.

After 1 h of methyl paraoxon exposure, decomposition rates significantly slowed, never achieving 100% decomposition. This observation shows that the metal oxides are reactive and not catalytic. The remaining surface hydroxyls and propanol are consumed during degradation which will now be discussed and is depicted in Figure 3.10. From the mass spectrometry data in Figure 7.A3, the two main decomposition products 4-nitrophenol (m/z = 138.02 g/mol) and dimethyl phosphate (DMP) (m/z = 125.00 g/mol) are clearly observed, with more 4-nitrophenol than DMP, suggesting that either DMP or the products of its subsequent decomposition, $[MePO_4]^{2-}$, $HPO_4{}^{2-}$

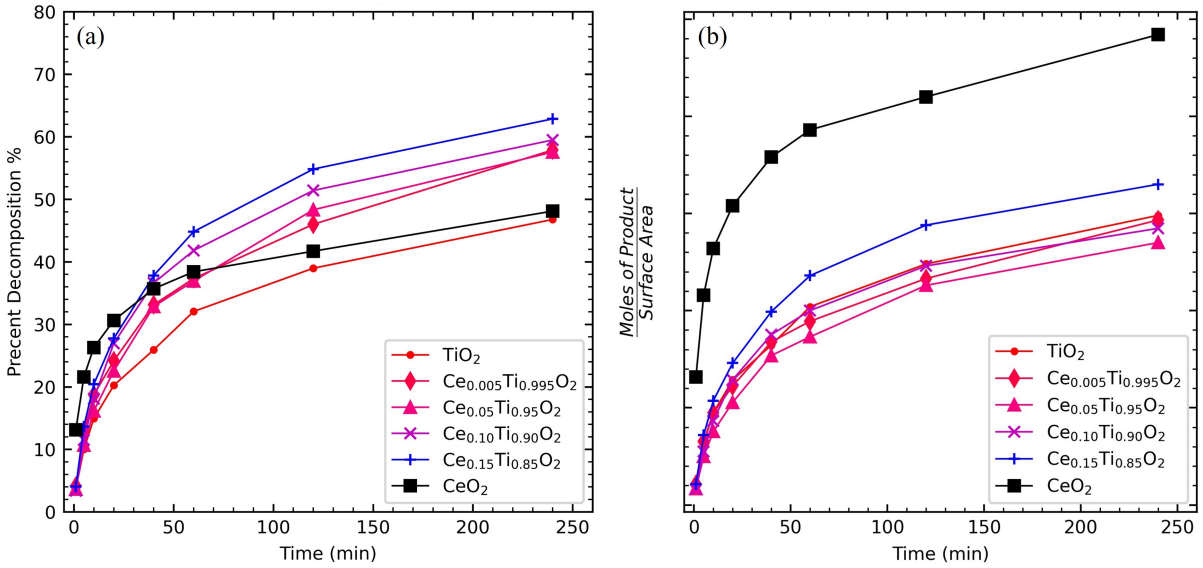


Figure 3.8: Methyl paraoxon decomposition (4-nitrophenol) as (a) total percent decomposed. As Ce-doping increases, the kinetics remains similar, but the total reactivity increases. (b) Surface normalized per surface area, over time. CeO_2 is the most reactive, whereas TiO_2 and $Ce_xTi_1 - xO_2$ (x = 0.5%, 5%, 10%) display little difference in their reactivity, unlike the x = 15% sample total decomposition is boosted.

Table 3.3: Methyl paraoxon decomposition (4-nitrophenol) as (a) total percent decomposed. As Ce-dopant increases, kinetics remains similar, but total reactivity increases with dopant. (b) Surface normalized per surface area, over time. CeO_2 is the most reactive, while TiO_2 and $Ce_xTi_{1-x}O_2$ (x = 0.5%, 5%, 10%) display little difference in their reactivity, unlike the x = 15 % sample total decomposition is boosted.

Material	**Pseudo-First Order**		k_{SA} [b] **min^{-1}/SA**	**Ranked Decomposition**	
	Rate constant (k_0)[a] min^{-1}	**r^2**		**Non-Normalized**	**SA Normalized**
TiO_2	1.73x10^{-2}	0.9871	9.81x10^{-5}	6	3
$Ce_{0.005}Ti_{0.995}O_2$	2.23x10^{-2}	0.9762	1.04x10^{-4}	3	4
$Ce_{0.05}Ti_{0.95}O_2$	1.87x10^{-2}	0.9861	7.40x10^{-5}	4	6
$Ce_{0.10}Ti_{0.90}O_2$	2.10x10^{-2}	0.9902	9.36x10^{-5}	2	5
$Ce_{0.15}Ti_{0.85}O_2$	2.43x10^{-2}	0.9813	1.16x10^{-4}	1	2
CeO_2	3.5x10^{-2}	0.9583	3.34x10^{-4}	5	1

or even propanol related products remain on the surface, deactivating reactive sites. To probe what remained on the surface, the methyl paraoxon dosed samples were centrifuged and washed with excess propanol, and the studied with DRIFTS.

Although we could not find previously published detailed IR studies of methyl paraoxon or DMP adsorption with propanol on metal oxides, we did find enough studies with other CWA simulants and phosphate molecules to assign modes to general regions of the spectrum [55, 65, 80, 110, 144]. The *ex-situ* DRIFTS results are shown in Figure 3.9, and a ATR FTIR spectrum of pure methyl paraoxon is shown in Figure 7.A2 for comparison. The IR spectrum for pure methyl paraoxon is dominated by peaks associated with 4-nitrophenol, which do not appear in any of the spectra in Figure 3.9, demonstrating that detectable amounts of methyl paraoxon or 4-nitrophenol are not present on the surface. Each sample has multiple broad peaks appearing between 1200 and 1100 cm^{-1}. This spectra region presents some ambiguity in peak assignment with DMMP and sarin due to multiple overlapping peaks from ν(O-P-O), ρ(O-CH_3) and ν(C-CH_3), coming from decomposed methyl paraoxon and propanol. Therefore, the peaks in this region can be attributed to these three modes [55, 65, 80, 110, 144]. While it cannot be directly attributed to DMP, a phosphorous-containing species remains bound to the MMOs' surface, deactivating active surface sites from further methyl paraoxon decomposition.

Other important signatures in the DRIFTS spectra provide some evidence for the identities of the potential decomposition products, and therefore decomposition pathways for methyl paraoxon. Peaks appear at 1452 and 1466 cm^{-1}, which we assign to the δ_{as}(C-CH_3) mode present in propanol. However, physisorbed propanol only exhibits 1 main peak at 1467 cm^{-1}. Previous studies with 2-propanol and sarin on Cu/TiO_2 have shown that physisorbed propanol exhibits only one main peak at a higher frequency while the sarin δ_{as}(C-CH_3) has a split peak at slightly lower wavenumbers [110]. This same trend is seen in our DRIFTS study, which suggests that a potential decomposition product is propanonated, dimethyl 2-propyl phosphate. Nevertheless, based on the peak width, there is also propanol remaining on the surfaces of MMOs. At higher wave numbers, the peaks

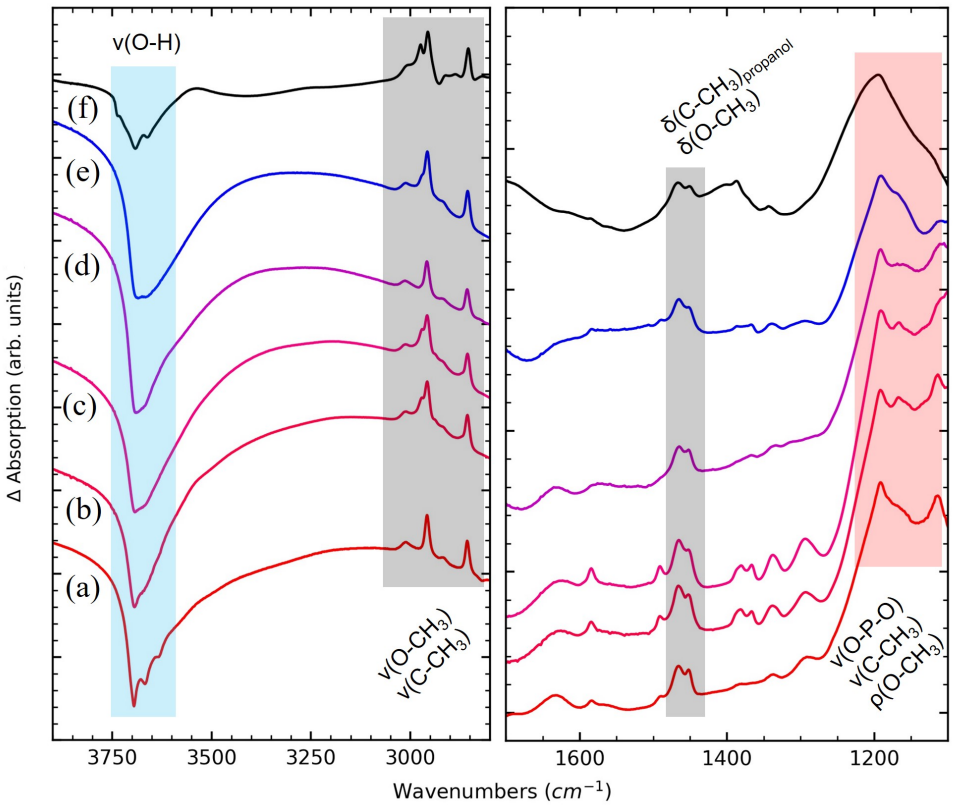


Figure 3.9: *Ex-situ* DRIFTS spectra of the metal oxides after methyl paraoxon exposure. a) TiO_2, Ce$-x$Ti$_{1-x}$O$_2$ b) x = 0.5%, c) x = 5%, d) x = 10%, e) x = 15% and f) CeO_2. All samples have methyl paraoxon bound to their surfaces, with the potential product dimethyl 2-propyl phosphate.

at 2856 and 2957 cm^{-1} are associated with ν_s and ν_{as}(O-CH$_3$), respectively. No peak appears at ~2820 cm^{-1} from a ν(M-O-CH$_3$) type of vibration. Any methanol cleaved from methyl paraoxon remains in solution.

Based on the DRIFTS results, we propose two decomposition pathways for methyl paraoxon in propanol, as depicted in Figure 3.10. We draw upon similar decomposition pathways proposed in the literature for methyl paraoxon and other CWA simulants [56, 77, 145]. As methyl paraoxon approaches the surface, it must first displace the solvent physisorbed on the surface. Once the solvent molecule is desorbed, the P=O of methyl paraoxon can interact with the metal cation. Metal sites adjacent to a bound solvent molecule can then perform a nucleophilic substitution, causing the 4-nitrophenol to be released into the solution. Alternatively, a surface hydroxyl group

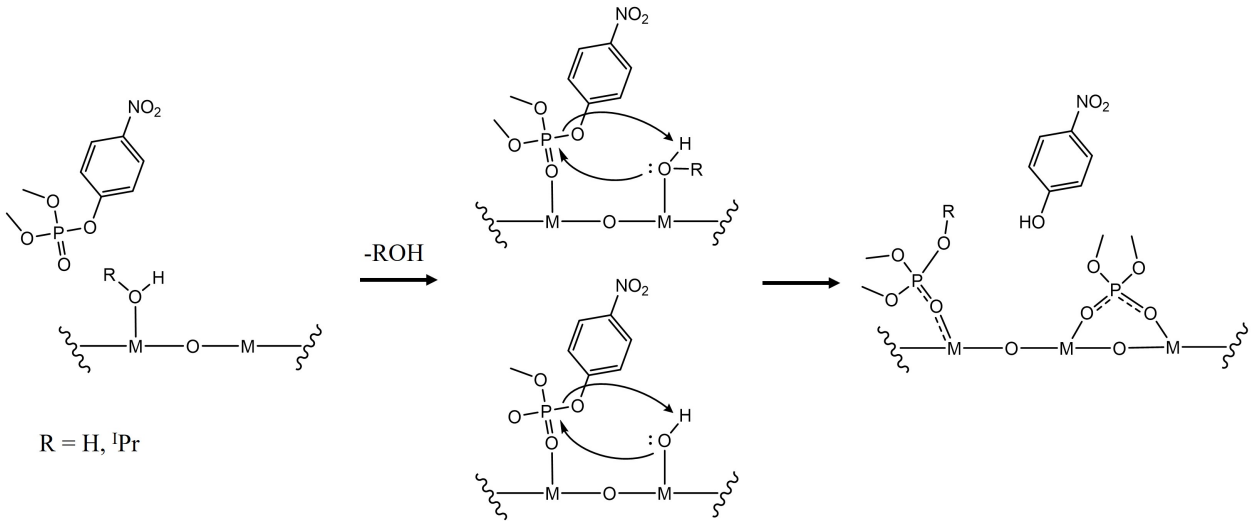


Figure 3.10: Proposed pathways for the decomposition of methyl paraoxon on the surface of our MMOs through reaction with solvent and surface hydroxyls. Methyl paraoxon must first displace the solvent to access the metal site. After interacting with neighboring solvent or surface hydroxyls, the decomposition proceeds to release 4-nitrophenol into solution.

can perform the nucleophilic substitution. The end products contain the phosphorus species bound to the surface, as evidenced by the DRIFTS measurements, with a small percentage desorbing into solution, seen in the mass spectroscopy measurements.

These results stress the importance of fundamental spectroscopic studies on mesoporous oxides for isolating the most relevant variables and factors for increasing reactivity towards CWA decomposition. By exploring different synthetic techniques for preparing mesoporous structures, one could control the type of crystallographic surface most exposed and energetically favorable to decomposition. Indeed, Trenque et al. demonstrated that the (111) facet in CeO_2 [56] is the most reactive; similar studies should follow for TiO_2. In addition, a future study could involve different solvents, such as water, or probe the photocatalytic aspect of TiO_2 and these Ce-doped materials. Ultimately, these efforts provide will better materials to protect warfighters, first responders, and civilian populations from chemical weapons.

3.4 Conclusion

Mesoporous TiO_2 and $Ce_xTi_{1-x}O_2$ (x = 0.005, 0.05, 0.1 and 0.15) were synthesized using a soft templating method, and mesoporous CeO_2 was synthesized through a hard templating method. Based on diffraction and electron microscopy, TiO_2 and $Ce_xTi_{1-x}O_2$ crystallized in the anatase-type structure, with no phase separation, while maintaining an ordered mesoporous structure. Based on nitrogen adsorption studies, we determined that TiO_2 and $Ce_xTi_{1-x}O_2$ maintain high specific surface areas (176-252 m^2/g) and display hysteresis consistent with cylindrical pores. Through pyridine adsorption experiment, we have shown that all of the materials featured Lewis and Brønsted acid sites, with pure TiO_2 having sites that are the most acidic. The $Ce_xTi_{1-x}O_2$ series exhibits Lewis and Brønsted sites assignable to Ce and Ti atoms, indicating that both metal cations are present on the surface.

By normalizing all of the decomposition calculations to the MMO surface area, we accurately assess and compare the reactivity of different materials in CWA decomposition. In this study, CeO_2 was the most reactive with a surface-normalized rate constant k_{SA} that is 3 to 4.6 times larger than those of all other MMOs. Ce-doping had little effect on reactivity and kinetics, although mostly amorphous $Ce_xTi_{1-x}O_2$ showed a slight increase in kinetics and overall reactivity. We conclude that the choice of a metal cation (Ce^{4+} or Ti^{4+}) in these MMOs is less important when it comes to the kinetics of methyl paraoxon decomposition than other factors, such as crystal structure.

Chapter 4: Experimental Study of the Adsorption and Decomposition of Sarin on Dry Copper (II) Oxide

The results presented in this chapter have been previously published in: Leonard, M. B.; Bruni, E.; Hall, M.; Li, T.; Rodriguez, E. E.; Durke, E. Experimental Study of the Adsorption and Decomposition of Sarin on Dry Copper (II) Oxide. J Phys Chem Lett 2022, 11663–11668. Matthew Leonard performed sample characterization, preparation and agent analysis. Eric Bruni and Morgan Hall handled agent dosing. Tianyu Li and Efrain Rodriguez contributed to the manuscript, and Erin Durke is the corresponding author.

4.1 Introduction

The last decade has proven chemical warfare agents (CWAs) constitute a persistent threat to homeland security that must be addressed [5, 146]. Among the most deadly of the CWAs are nerve agents, including the G-series, V-series, and novichoks agents. Of particular concern is sarin (GB), due to its high toxicity and high vapor pressure [19]. Research into the neutralization of sarin often involves the use of less toxic simulants, such as dimethyl methyl phosphonate (DMMP) and dimethyl 4-nitrophenyl phosphonate (DMNP) to estimate reactivity [21, 77]. Although important lessons can be drawn from the simulants, studies with live CWAs are necessary for accurate determination of a material's potential for gas filtration.

Lena Trotochaud et al. previously conducted a detailed study of CuO nanoparticles with DMMP using infrared (IR) spectroscopy , ambient pressure X-ray photon spectroscopy (APXPS),

and density functional theory (DFT) calculations [57]. Their studies showed that DMMP readily decomposes on CuO, which cleaves the P-OCH_3, PO-CH_3 and P-CH_3 bonds at room temperature. All decomposition species remain bound to the surface. The DFT calculations showed that oxygen vacancies have minimal effect on the decomposition capability of CuO. Trotochaud et al.'s results are encouraging and make CuO a promising material to study with sarin. Copper is a unique element, being both Earth-abundant and inexpensive while possessing a variety of interesting chemical characteristics. With a wide range of oxidation states (Cu^0, Cu^{1+}, Cu^{2+} and Cu^{3+}), copper can induce both single and double electron processes [147]. CuO specifically has shown high catalytic activity, oxidizing CO at low temperatures [148]. The monoclinic crystal structure of CuO, with a local square planar geometry, gives rise to undercoordinated metal centers, increasing the likelihood of reactivity.

In this work, we study dry CuO nanoparticles with the deadly nerve agent sarin. Dry CuO nanoparticles provide the simplest system to build on, future work will determine the effects of more complex CuO systems. Through IR spectroscopy, we can identify GB adsorbing to the surface through the P=O bond, decomposing through P-F bond cleavage producing a bridging species, isopropyl methyl phosphonic acid (IMPA). Approximately 18 h after initial dosing, the intact GB that is strongly adsorbed to the surface continues to react. The experimental results are consistent with DFT calculations that were recently reported [59].

4.2 Experimental Section

4.2.1 Material Characterization

CuO nanoparticles (< 50 nm) diameter were purchased from Sigma-Aldrich. The nanoparticles were characterized through electron microscopy, x-ray scattering and nitrogen adsorption. Powder X-ray diffraction (XRD) patterns were collected using a Bruker X-ray diffractometer with a Cu Kα radiation (λ = 1.5406 Å) and a LynxEye position-sensitive detector. Rietveld refinement was

performed using GSAS II [133]. Nitrogen isotherms were recorded with a Micrometrics ASAP 2020 Porosimeter. Samples were degassed in vacuum at 150 °C for 6 h prior to characterization. The surface area was determined using the Brunauer-Emmett-Teller (BET) method with a relative pressure range (P/P_o) of 0.05-0.30. Pore size and volume was calculated from the adsorption branch using the Barrett, Joyner, and Halenda (BJH) method.

Transmission electron microscopy (TEM) imaging was performed on a JOEL-2100 LaB_6 TEM with an accelerating voltage of 200 kV and a beam current of 104 μA. All samples were dispersed in ethanol and drop cast onto a lacey carbon 200-mesh copper or gold grid. Scanning electron microscopy (SEM) imaging was performed using a Hitachi SU-70 Field Emission SEM equipped with a Bruker energy dispersive spectroscopy (EDS) detection model: Flash 6T/60 with a silicon drift detection (no Li dopant) and solid angle of 0.189 sr.

4.2.2 Experimental IR Procedures

CAUTION! Sarin is a highly toxic acetylcholinesterase inhibitor, and should only be handled by highly trained scientists, with proper personal protection equipment (PPE) in a secure government regulated facility. The experiment was conducted in a high vacuum chamber with a base pressure of 3×10^{-9} Torr. The CuO nanoparticles were pressed into a $0.004''$ tungsten grid, with a K type thermocouple welded to the grid. The W-grid was secured to the sample manipulator by stainless steel clamps attached to copper rods. The copper rods were attached to a 50-amp power source for resistive heating up to $\sim$1000 K, with a resolution of $\sim$0.1 K. The CuO nanoparticles were placed into the chamber and backfilled with 10 Torr of O_2 and heated to 523 K for 1 h to clean the surface of contaminates such as water, hydrocarbons, and remove surface hydroxyls. The IR scans were conducted with a Thermo Nicolet 6700 FTIR Spectrometer. The spectra were recorded with a MCT A detector cooled with liquid nitrogen, 256 spectra averaged per scan, resolution of 2 cm^{-1}, aperture 50, optical velocity 1.89.

Prior to dosing, IR spectra were obtained of the clean CuO NPs, and W-grid, for use as references. Experiments were conducted via a flow through experiment, with the chamber remaining under vacuum throughout dosing. This approach causes sarin to either adsorb to the surface or be pumped away, simplifying the reaction. Sarin was introduced into the chamber at a pressure of 1 $\times 10^{-5}$ Torr, with IR spectra obtained taken approximately every 4 min. Prior to the experiment, sarin was purified through a freeze-pump-thaw process. The clean CuO spectrum were subtracted from the subsequent spectra, creating a difference spectrum. Therefore, any positive peaks indicate species adsorbing, whereas negative peaks indicate species desorbing.

4.3 Results

4.3.1 Material Characterization

The CuO nanoparticle characterization data is shown in Figure 4.1. SEM and TEM images show a dispersed shape and sized particles with a diameter generally less than 50 nm. The XRD data shows the particles are phase pure CuO. Through Rietveld refinement, we calculated the average crystallite size to be 35.9 nm. Nitrogen adsorption isotherm exhibits an H3-type hysteresis, which indicates that the sample is composed of nanoparticles. The calculated BET specific surface area is 13.27 m^2/g, and the BJH pore volume is 0.037 cm^3/g.

4.3.2 Adsorption and Decomposition of Sarin on Dry CuO Nanoparticles

Time-resolved IR scans and composite peak fit of GB exposed to dry CuO are shown in Figure 4.2. For simplicity, only the final scan of GB exposure on CuO is plotted in Figure 4.3, with GB vapor for reference. Consolidated in Table 4.1 are the vibrational modes for gas phase GB, liquid phase GB, IMPA and GB exposed to CuO nanoparticles.

Upon dosing, IR peaks appear at 1245 and 1032 cm^{-1}, corresponding to the ν(P=O) and ν(C-

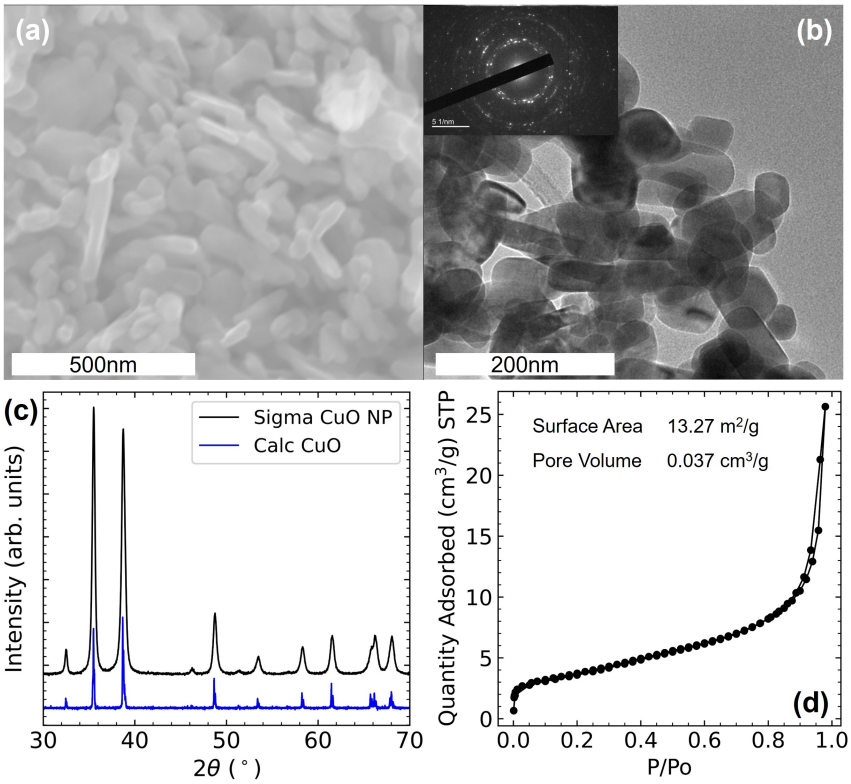


Figure 4.1: Characterization of the CuO nanoparticles. a) SEM and b) TEM images with electron diffraction pattern. c) XRD pattern showing that the particles are pure CuO and d) nitrogen adsorption isotherm, showing an H3 hysteresis which is consistent with nanoparticles.

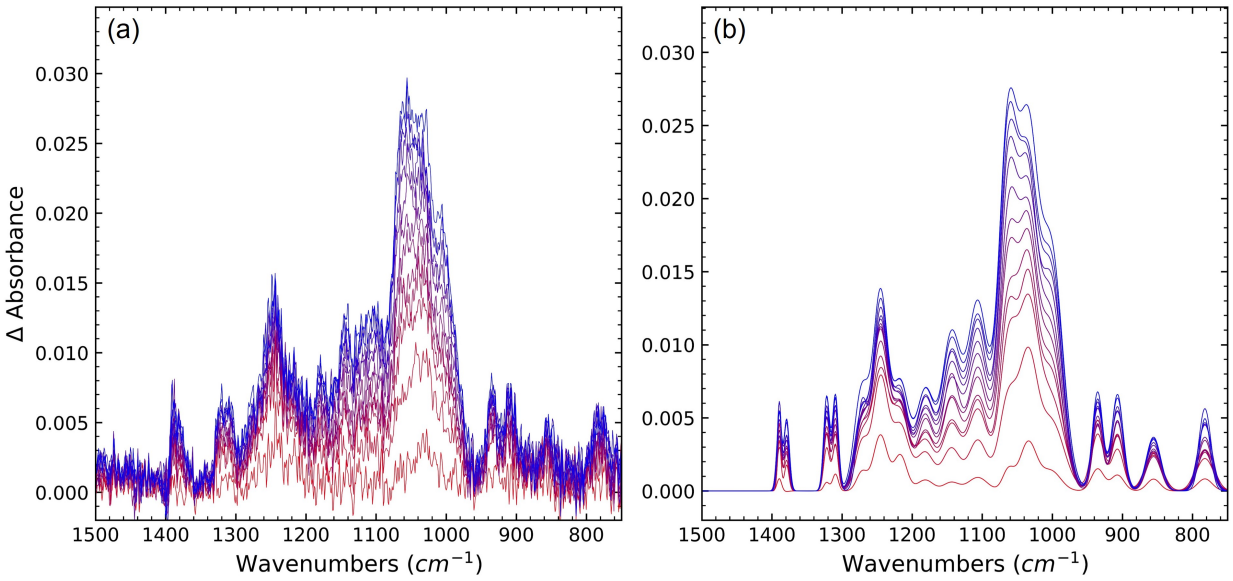


Figure 4.2: IR difference spectra of dry CuO nanoparticles exposed to GB over 1.75 h with a) raw IR spectrums and b) composite peak fitting spectrum

O-P) modes of physisorbed sarin, respectively. The ν(P=O) vibration is red shifted by 58 cm^{-1} relative to that for vapor phase sarin, indicating a strong interaction between sarin and a Lewis acid site (Cu) through the P=O bond. The ν(C-O-P) mode blue shifts 12 cm^{-1} from gas and liquid phase GB. Similar shifts have been observed experimentally and computationally with sarin on TiO_2 [80, 109]. This shift is believed to result from charge transfer during adsorption. The Lewis acid site pulls electron density away from the P=O bond, causing the phosphorus center to become slightly positive compared to the vapor phase. Therefore, strengthening the P-OC bond, results in the vibrational blue shift.

Clear signs of decomposition can be seen in the δ_s(P-CH_3) and ρ(P-CH_3) modes. Doublets appear, with the δ_s modes at 1321 and 1309 cm^{-1} and the ρ modes at 935 and 907 cm^{-1}. The P-CH_3 band is strongly affected by cleavage of the P-F bond [149, 150]. Upon replacing the highly electronegative fluorine with the less electronegative oxygen electron density moves back onto the phosphorus, weakening the surrounding bonds. Weakening of the bonds resulting the vibrations to red shift (1309 cm^{-1} and 907 cm^{-1}) indicative of P-F cleavage, producing IMPA. The shift is also

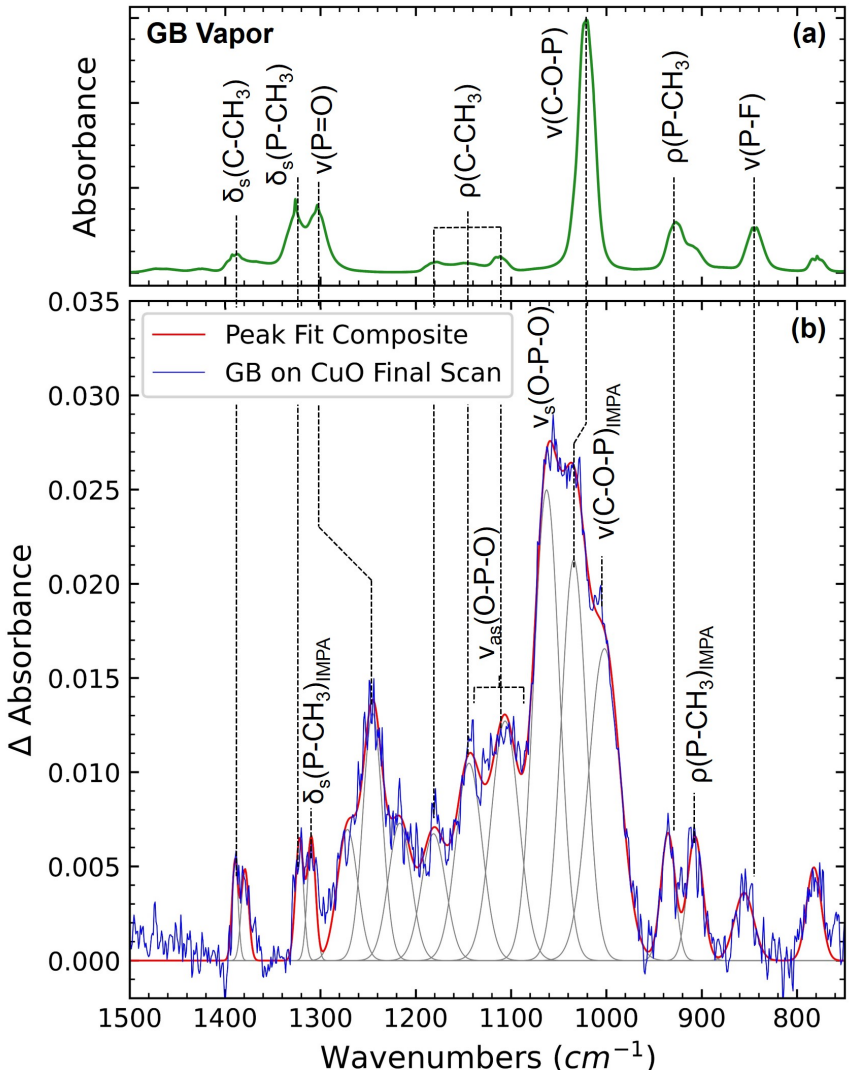


Figure 4.3: Infrared spectrum of a) GB vapor. b) Final IR scan of GB exposed to CuO nanoparticles in blue. Individual peak fitting is in grey and the resultant composite spectrum is in red. The vibrational assignments were determined based on references [80, 149].

seen in the ν(C-O-P) mode, red shifting from 1032 to 997 cm^{-1}, which manifests as a shoulder growing in. This behavior is further evidence supporting sarin is decomposing to IMPA.

After several minutes of GB vapor on the CuO nanoparticles, a shoulder grew in at 1062 cm^{-1}. The shoulder continued to grow throughout the experiment. The peak is assigned to bridging ν_s(O-P-O). Typically, bridging ν_s(O-P-O) is reported at $\sim$1180 cm^{-1} on TiO_2 [68, 80, 110], Zr

based MOFs [151], and CeO_2 [55]. As IR measures bond strength, the Lewis acid site will directly affect the O-P-O bond. One method to measure the strength of Lewis acidity, is through pyridine adsorption. Pyridine adsorbed onto Lewis acidic site, the ν(C-C-N) mode adsorbs between 1630 and 1600 cm^{-1}, with stronger sites adsorbing at higher wavenumbers. On CuO, pyridine has been shown to adsorb at 1609 cm^{-1}, plotted in Figure 4.4, whereas TiO_2, ZrO_2, and CeO_2, adsorption is observed below 1605 cm^{-1} [54, 134], indicating that they are weaker Lewis acid sites. Therefore, the CuO will pull more electron density away from the oxygens resulting in a greater red shift of the ν_s(O-P-O) mode.

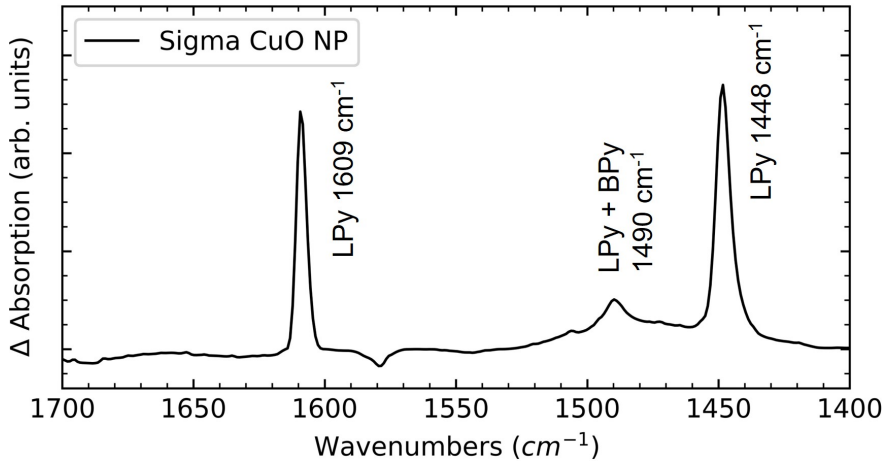


Figure 4.4: IR difference spectrum of CuO NPs exposed to pyridine showing two main Lewis acid sites (LPy) at 1609 and 1448 cm^{-1} and a site displaying characteristics of both LPy and Brønsted acid sites (BPy) at 1490 cm^{-1}. Mode assignment are derived from reference [134]

Following initial exposure, the CuO nanoparticles are decomposing sarin. However, the data also indicate the presence of intact GB. The mode at 855 cm^{-1} belongs to ν(P-F), and two modes at 1271 and 1245 cm^{-1} belonging to ν(P=O). To determine how sarin continues to interact with CuO post exposure, the chamber was brought back to base pressure (1×10^{-8} Torr) and reexamined after 18 h. This sample will be referred to as "GB on CuO post purge".

Table 4.1: Assignment of IR frequencies of vapor and liquid phase Sarin and liquid phase IMPA from references [80, 149]. Assigned vibrational modes of sarin and decomposition products on CuO nanoparticles. All frequencies are reported in wavenumbers (cm^{-1}).

IR band assignment	$Sarin_{Vapor}$	$Sarin_{Liquid}$	$IMPA_{Liquid}$	GB on CuO
ν(P-F)	845	845		855
ρ(P-CH_3)	928	917, 928	906	935, 907
ν(C-O-P)	1020	1020	1004	1032, 997
ν_s(O-P-O)				1062
ρ(C-CH_3)	1111	1106	1108	1106
ν_{as}(O-P-O)				1144-1106
ρ(C-CH_3)		1145	1143	1144
ρ(C-CH_3)	1183	1180	1179	1181
ν(P=O)	1303	1278	1203	1271, 1245, 1216
δ_s(P-CH_3)	1328	1321	1314	1322, 1309
δ_s(C-CH_3)	1390	1389, 1379	1387, 1376	1379, 1390

4.3.3 Decomposition of Sarin on Dry CuO Nanoparticles Post Purge

An important part of evaluating the performance of filter materials is determining the pathways of the CWA after exposure. Possible pathways include, 1) whether the CWA remains on the surface; 2) the CWA continues to react; or 3) the CWA desorbs. The GB exposed CuO was purged and held at 1×10^{-8} Torr for 18 h, after which the purged sample was rescanned and plotted in Figure 4.5. The final GB exposure scan is shown for reference.

After 18 h, the data suggests GB continues to react on the surface of the dry CuO. The ν(P=O)

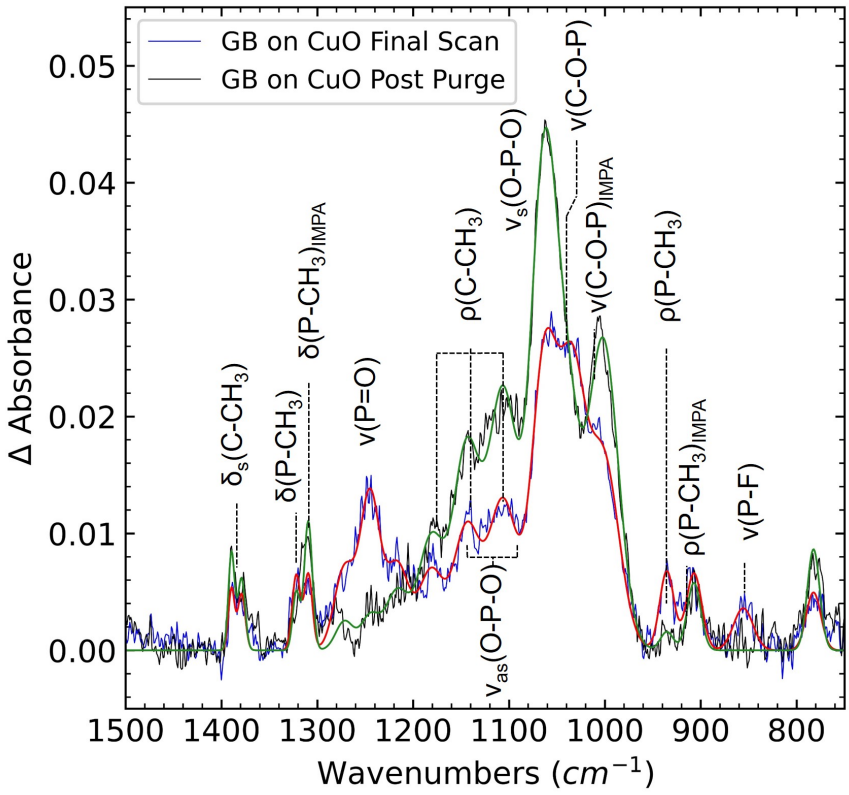


Figure 4.5: IR difference infrared spectrum of the final GB exposure on CuO nanoparticles in blue, with a composite spectrum from peak fitting in red. The spectrum of the purged sample 18 h after returning to base pressure is plotted in black, with the composite spectrum from peak fitting is plotted in green.

and ν(C-O-P) peaks decrease, and the ν(P-F) peak disappears, whereas the peaks related to IMPA continue to grow, including the ν_s(O-P-O), δ_s(P-CH$_3$)$_{IMPA}$, ν(C-O-P)$_{IMPA}$, and ρ(P-CH$_3$)$_{IMPA}$. The region between 1144 and 1106 cm^{-1} includes two ρ(C-CH$_3$) stretches but would not be affected by degradation of sarin to IMPA. However, we see this area continue to increase. The ν_{as}(O-P-O) peak has been reported between 1170 and 1135 cm^{-1} [80, 110, 150, 152]. As discussed in the previous section, the ν_s(O-P-O) peak is red shifts by $\sim$20 cm^{-1} relative to literature values, due to a strong interaction with CuO. Therefore, the shift in the ν_{as}(O-P-O) is expected, however due to the overlapping peaks we cannot directly assign this mode.

Figure 4.6 depicts the proposed decomposition pathway of sarin on dry CuO, based on our

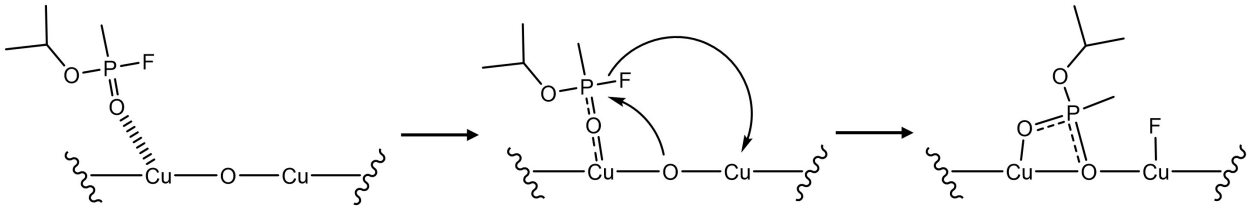


Figure 4.6: Proposed mechanism for the decomposition of sarin on dry CuO.

experimental results. Sarin adsorbs onto the surface through the P=O bond, and strongly interacts with the Lewis acid site, similar to previously reported mechanisms for CWAs and CWA simulants [55, 63, 153]. Once the sarin adsorbs, the neighboring lattice oxygen cleaves the P-F bond, creating a bridging species, as is evident from the presence of ν(O-P-O) modes. It is likely the fluorine will remain bound to a neighboring Cu atom, although this binding cannot be observed within the IR spectroscopy frequency range of the detector.

To learn more about dry CuOs reactivity and determine whether additional chemistry could occur, the sample was heated in increments of 25 K to 523 K. The corresponding IR spectra are plotted in Figure 4.7, with negative peaks indicating desorption. Unlike in previous work with TiO_2, sarin did not continue to react [80], upon heating. The decomposed product IMPA, begins desorbing at 423 K, ultimately desorbing completely. Therefore, it is likely that IMPA is tightly bound to the surface, but the activation barrier for further degradation is larger than the desorption energy. The fact that all IMPA peaks disappear at the same time suggests that the molecule remains intact. Although we were unable to retest the surface, the complete desorption of IMPA suggests that CuO could be regenerated for further use. The negative peak at $\sim$1280 cm^{-1} marked with an asterisk in Figure 4.7, is an unknown species that is generated by changes in the CuO surface or by species that did not desorb during pretreatment and not related to sarin. The difference spectrum between the starting material and post heating is plotted in Figure 7.A8, showing the peak $\sim$1280 cm^{-1} at has no relation to GB.

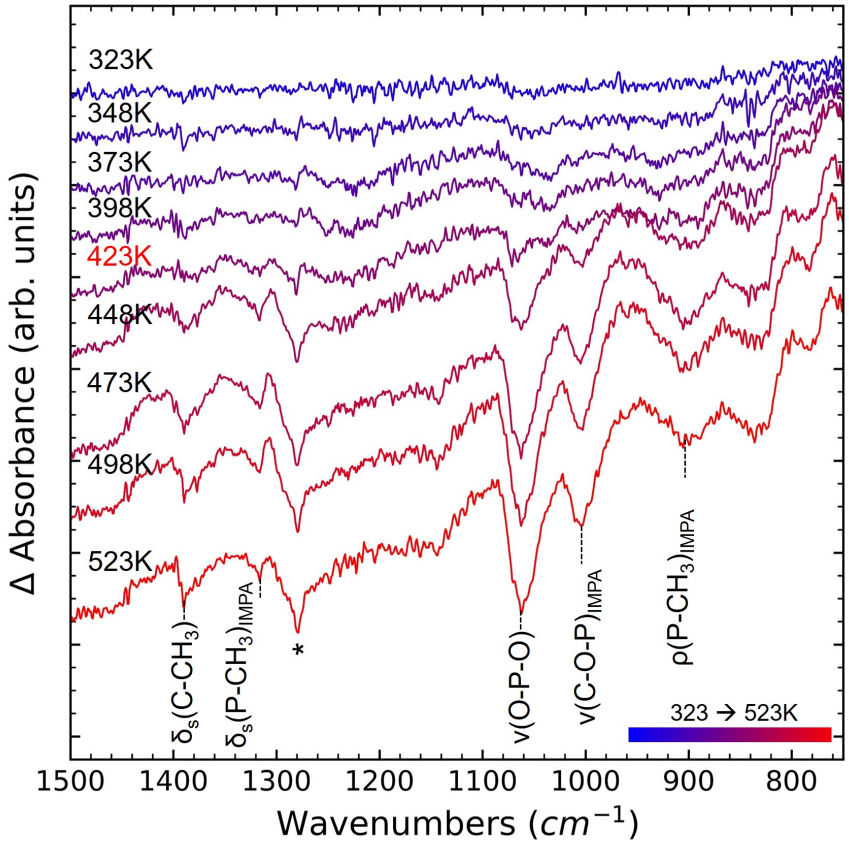


Figure 4.7: GB on CuO post purge heated to 523 K. Instead of reacting further on the surface, the peaks associated with IMPA become negative as the molecule leaves the surface. The feature at 1280 cm^{-1} is attributed to an unknown surface contamination.

4.4 Discussion

DFT calculations are a powerful tool for visualizing molecular interactions and strengthen a fundamental understanding. Ma and Cao recently published DFT calculations that model the adsorption and decomposition of sarin on wet and dry Cu_2O (111) and CuO(111) [59]. The calculations indicate that sarin strongly adsorbs to an under coordinated Cu atom through the P=O bond, with an adsorption energy between -122.7 an -139.2 kJ/mol. Our experimental data support this finding, given the large shift in the ν(P=O) mode frequency (58 cm^{-1}) from the gas phase. The strong Lewis acid site pulls electron density from the oxygen, weakening the bond and causing the red shift in the ν(P=O) mode.

The decomposition pathways calculated by Ma and Cao are shown in Figure 4.8, with three possible decomposition products, through the cleavage of the P-F, PO-C_3H_7 and P-OC_3H_7 bonds. The lowest activation energy is through the TS_S2-A pathway, cleaving the P-F bond, with an activation barrier of 106.3 kJ/mol and an overall exothermic reaction with an energy value of -51.4 kJ/mol. After adsorption, sarin reorients before cleaving the P-F bond. The phosphorus center forms a bond with the lattice oxygen, whereas fluorine bridges two copper atoms. Although cleavage of the PO-C_3H_7 and P-OC_3H_7 bonds are still exothermic, the activation barriers are higher than P-F cleavage at 111.9 and 153.4 kJ/mol respectively.

The results of from Ma and Cao calculations agree well with our experimental measurements. From Figure 4.5, the shifts in the P-CH_3 stretches and the reduction in the intensity of the higher frequency modes following chamber purge are clear indicators of the cleavage of the P-F bond producing IMPA. The accompanying features associated with the ν(O-P-O) modes indicate that decomposition of GB creates a bridging species on the surface of CuO. GB is decomposed on dry CuO through cleavage of the P-F bond. Although the IR data do not provide insight into the binding nature of the fluorine, without surface hydroxyl groups, fluorine is expected to remain bound to the surface on a metal center.

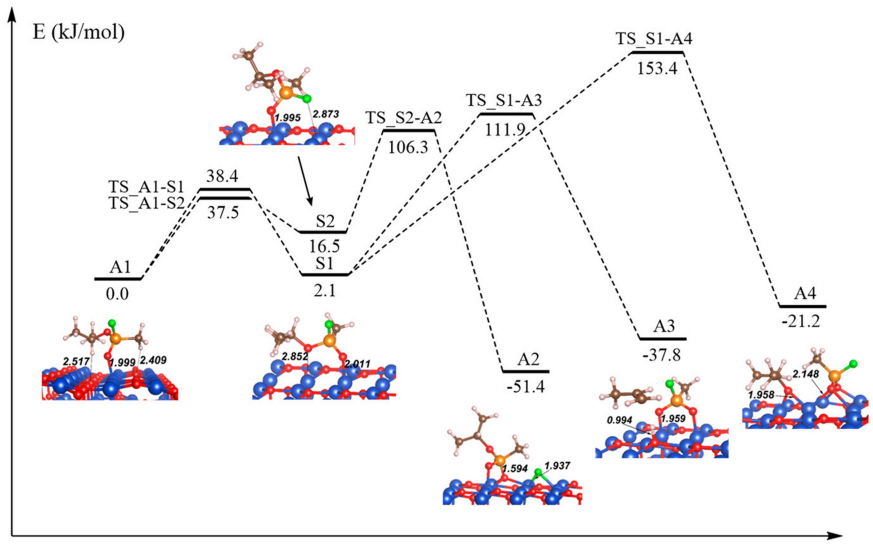


Figure 4.8: Predicted relative energy profiles associated with GB decomposition on pristine CuO (111). Reprinted with permission from reference [59]. Copyright 2021 American Chemical Society.

The other possible decomposition product, methylphosphonofluoridic acid (MPFA) is potentially remains on the surface. Although MPFA shares IR modes with intact GB with the δ_s(P-CH_3) at 1322 cm^{-1} [80]. The post purged sample lacked a strong P=O peak, but a small contribution from δ_s(P-CH_3) at 1322 cm^{-1} remained, suggesting that MPFA is present in low quantities. Calculations were only performed on CuO(111), we would expect a distribution of the facets other than the (111). The other planes could support the production of MPFA over IMPA.

Dry CuO has been shown to be reactive to GB experimentally and computationally. However, in practical applications, the surface will be hydroxylated and will contain absorbed water molecules. The calculations on wet and hydroxylated CuO (111) surface has a lower adsorption energy ranging from -51.9 to -80.9 kJ/mol [59]. However, during decomposition, the lowest calculated activation barrier is 109.5 kJ/mol. Therefore, we would expect to see a reduction in activity in a hydroxylated system. That said, the factors that affect CWA decomposition experiments with GB and hydroxylated CuO should continue to be investigated.

4.5 Conclusion

The adsorption and decomposition of sarin on dry CuO nanoparticles were studied using IR spectroscopy, and were compared to published DFT calculations. During adsorption of GB, the ν(P=O) mode red shifts by $\sim$58 cm^{-1}, based on strong interactions of the P=O group copper atoms. GB decomposes quickly, through the cleavage of the P-F bond, creating a bridging species with the help of the lattice oxygen atoms, producing IMPA. Upon heating, IMPA does not degrade further on the CuO surface, but rather desorbs intact above 423 K. The experimental results follow the lowest energy pathway in the published DFT calculations. Showing that dry CuO is a highly active material for GB decomposition. The work described here provides a baseline study using a simple system, dry CuO, to build fundamental knowledge that will be used in further explorations of more complex CuO surfaces.

Chapter 5: Low Temperature Combustion of Nerve Agent Simulant on Mesoporous Nickel Oxide and Cu-Doped Nickel Oxide

5.1 Introduction

Organophosphorus molecules, an important class of compounds, have been used as fuel additives, lubricants, plasticizers, and insecticides [16]. However nerve agents, are a subset of organophosphorus molecules that are highly toxic cholinesterase inhibitors or more broadly as chemical warfare agents (CWAs) [3]. Two of the most common nerve agents, sarin (GB) and soman (GD) shown in Figure 5.1, were developed as insecticides in 1936 and 1944 respectively, but were quickly transitioned to military purposes [2]. Sarin was employed during the Iraq-Iran wars, and has been used as recently as 2013 in Syria, killing over 1000 civilians [116]. An individual's respiratory defense against CWAs falls on standard issue military gas mask. The filter on a gas mask contains a microporous carbon with a mixture of metal impregnates [11]. Although the current filtration technology offers a broad range of protection against CWAs and toxic industrial compounds (TICs), the filter composition has not changed significantly in the last 50 years [11].

Metal organic framework (MOFs) [151, 154], zeolites [47, 155] and metal oxides have been examined for next generation filtration material, that can improve on the current filtration technology and be more adaptive to future threats. Metal oxides have been used in heterogeneous catalysis since the mid 1950s. Their robust nature, low cost, and ability to fully oxidize organic molecules make metal oxides a viable option for CWA filtration and decontamination [48]. Metal oxides that have been studied for sarin and CWA simulant decomposition include TiO_2 [54, 65, 67, 68], Al_2O_3

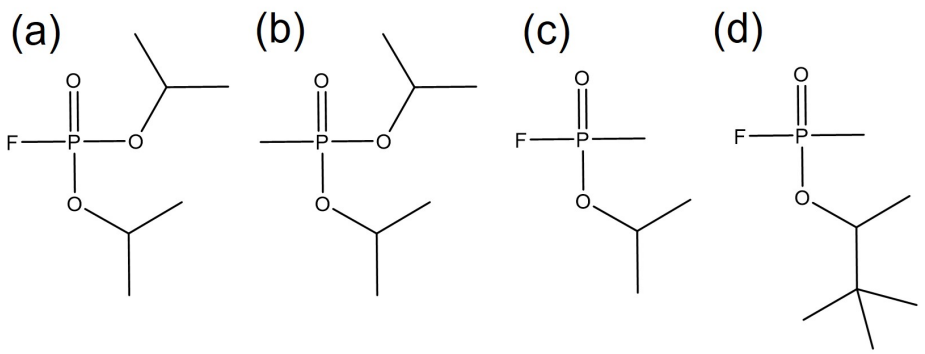


Figure 5.1: (a) CWA simulant diisopropyl fluorophosphate (DFP), (b) diisopropyl methylphosphonate (DIMP), (c) CWA sarin and (d) soman.

[50], Cu_xO [57, 60], Fe_2O_3 [156, 157], CeO_2 [55], and ZrO_2 [74].

In Chapter 4, CuO was shown to be highly active in the decomposition of sarin at room temperature. A special characteristic of Cu^{2+} is that this ion has a d^9 electron configuration, which is Jahn-Teller active when placed in an octahedral or tetrahedral geometry. With an electronic configuration of d^9, the e_g orbitals have a filled orbital and a partially filled orbital. To lower the molecule's overall energy, the e_g orbitals break the degeneracy, causing the axial bonds to lengthen or compress. Figure 5.2 shows how the elongation of the axial bonds changes the electronic state. Jahn-Teller active perovskites have been shown to be highly active in oxygen reduction reactions, as these materials balance the exchange between $O_2{}^{2-}$ and OH^- on the surface [83]. NiO adopts a rock salt crystal structure making the cation local cation geometry octahedral. Therefore, through isovalent substitution of Cu^{2+} with Ni^{2+} in NiO, we can investigate whether Cu^{2+} in Jahn-Teller active geometry shows increased activity for CWA simulant decomposition.

Surprisingly, NiO has not yet been explored for gas phase CWA decomposition. NiO has gained interest in a variety of fields, such as electrochemistry [158], gas sensing [159, 160] and catalysis [161, 162] for its chemical stability, unique chemical characteristics, and low cost. NiO is a known p-type semiconductor, naturally forming Ni^{2+} vacancies, to produce two cation holes (h^+) [49]. To charge balance the 2 h^+ the 2 neighboring Ni sites oxidize to Ni^{3+} or the surrounding oxygen

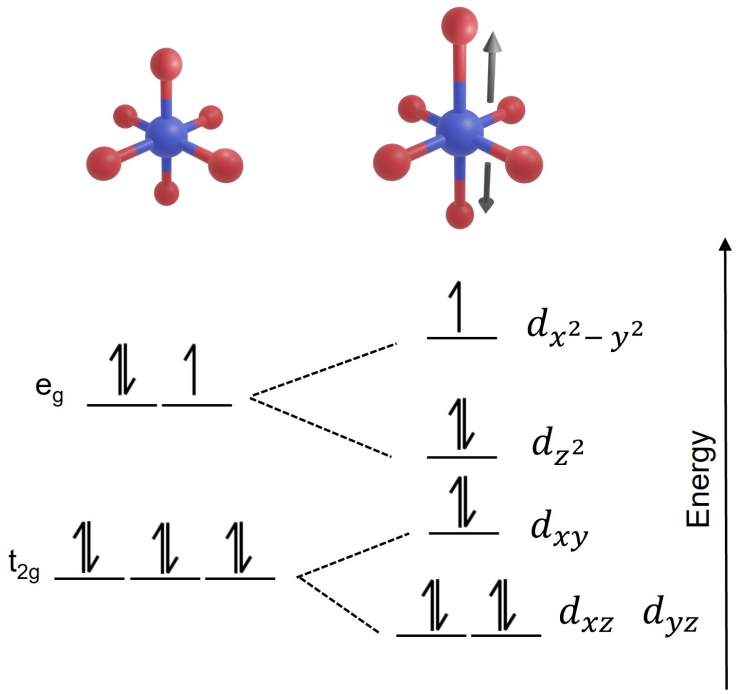


Figure 5.2: Illustration of an octahedral molecule with an electron configuration of d^9. The molecular orbitals break degeneracy, resulting in the lengthening of the axial bonds.

sites oxidize from O^{2-} to O^{-}. Both states exist under normal conditions. These defects can serve as sites for the dissociation of water or active oxygen which is linked to increased oxidation of CO and volatile organic compounds (VOCs) [49, 163]. By using NiO in the form a mesoporous metal oxide, we can maximize surface area, chemical diffusion, and reactivity. Mesoporous materials have shown superior reactivity compared to nanoparticles, making the mesoporous materials ideal for filtration technology [164].

Typically, the CWA simulant of choice for vapor phase studies is dimethyl methyl phosphonate (DMMP), which is stable and has low toxicity. However, DMMP does not accurately mimic the reactivity of sarin, due to the absence of a P-F bond. In this study, we chose to work with diisopropyl fluorophosphate (DFP) shown in Figure 5.1a, due to its molecular similarities to sarin, including a P-F bond and isopropyl functional group. Research into vapor phase decomposition of DFP has been limited [165, 166], which is likely due to DFPs high toxicity. Liquid phase studies

show similar decomposition kinetics as those of G-agents [22], but more studies are needed to understand whether DFP has surface interactions similar to those of G-agents.

In this study, we synthesized ordered mesoporous $Cu_xNi_{1-x}O$ ($x \leq 0.20$) through a hard templating method. Cu^{2+} was successfully incorporated into the NiO crystal structure while maintaining high surface area. This solid solution, along with mesoporous NiO, were exposed to DFP in an oxygen-rich environment (Zero Air (ZA)). All materials were highly active, showing room temperature decomposition producing primarily oxidation products CO, carbonyls, carbonates, and CO_2. NiO was the most reactive material studied and was further probed in an oxygen-free environment (He gas), low temperatures, and a higher pretreatment temperature. These tests revealed NiO will begin degrading DFP at temperatures as low as -50 °C. Surface oxygen was shown to be important for NiO's reactivity, and terminal hydroxyls are necessary for full oxidation to CO_2.

5.2 Experimental

5.2.1 Synthesis of Mesoporous NiO and Cu-Doped NiO

Mesoporous NiO was synthesized using a nanocasting process previously published in literature [167]. The silica template KIT-6 was first prepared via a reported method [95]. The aging temperature during the KIT-6 synthesis was 100 °C . In a typical synthesis, 4 g of $Ni(NO_3)_2 \cdot 6$ H_2O is dissolved in 15 mL of ethanol. Half of the solution (7.5 mL) is then added to 1 g of KIT-6 and stirred in a covered beaker for 1 h. The cover is removed and the solution is stirred at room temperature until dry. The dried solution is scraped, re-fluffed, dispersed in 7 mL of dry hexane and stirred uncovered till dry. This process was repeated with the remaining nitrate solution and dry hexane. The powder is scrapped from the beaker, placed into a $\sim$ 3 mL vial and heated to 500 °C at 1 °C/m for 3 h. The resultant grey powder was etched twice in 0.1 M NaOH at 90 °C for 1h, centrifuged and then washed with DI water and ethanol. The powder is dried at 100 °C overnight. For the synthesis of $Cu_xNi_{1-x}O$, the same procedure is used, with the appropriate molar ratio of

$Cu(NO_3)_2 \cdot 3\ H_2O$.

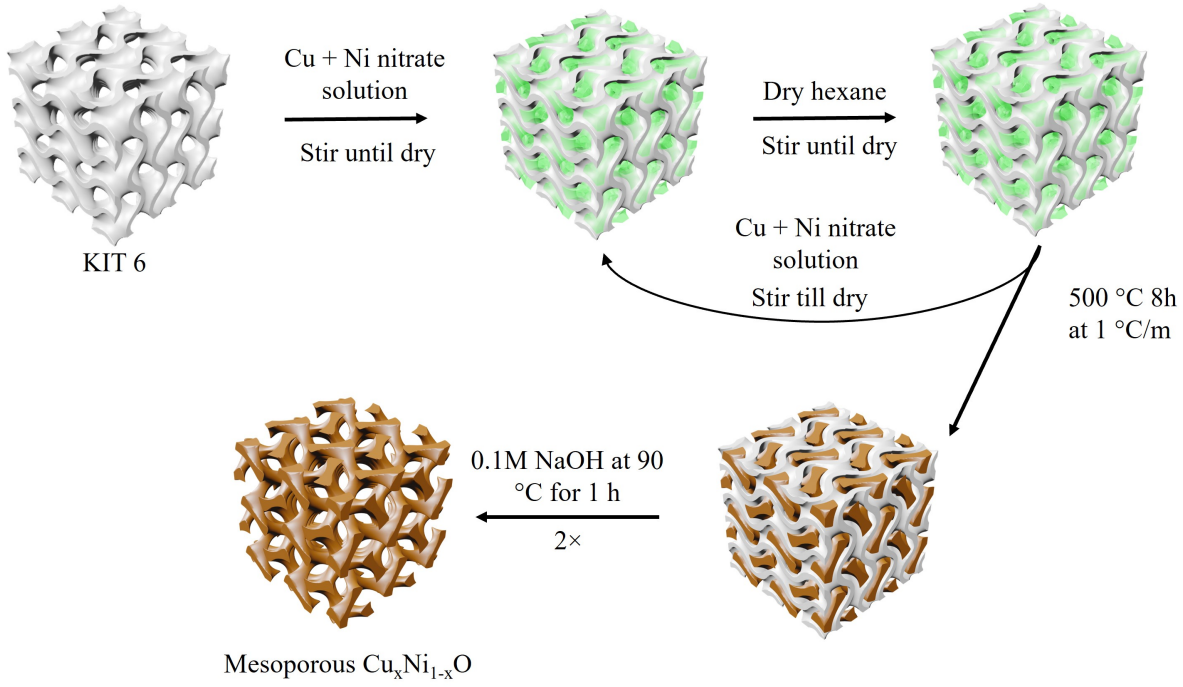


Figure 5.3: Graphical depiction of the synthesis of mesoporous $Cu_xNi_{1-x}O$.

5.2.2 DFP *in-situ* Diffuse Reflectance Infrared Fourier Transform Spectroscopy (DRIFTS) Measurements

CAUTION! DFP is an acetylcholinesterase inhibitor and should only be handled with proper safety protocols and equipment. *In-situ* DRIFTS experiments were conducted with a Thermo Nicolet iS50r FTIR Spectrometer equipped with a PIKE heat chamber DiffusIR, with the DiffusIR accessory maintained at 25 °C. The spectra was recorded with a MCT High D* detector cooled with liquid nitrogen, 128 spectra averaged per scan, resolution of 2 cm^{-1}, aperture 65, optical velocity 3.797. The DFP chemical micro saturator (Glassblowers, Inc) was submerged in a temperature-controlled water bath and maintained at 20 °C, and purged prior to each experiment. The DRIFTS cell was configured to flow, zero air (∼20% O_2, ∼80% N_2) or He from the top of the sample to

the bottom, with a flow rate of 1.5 mL/min. A schematic of the DRIFTS set up is shown in Figure 7.A9.

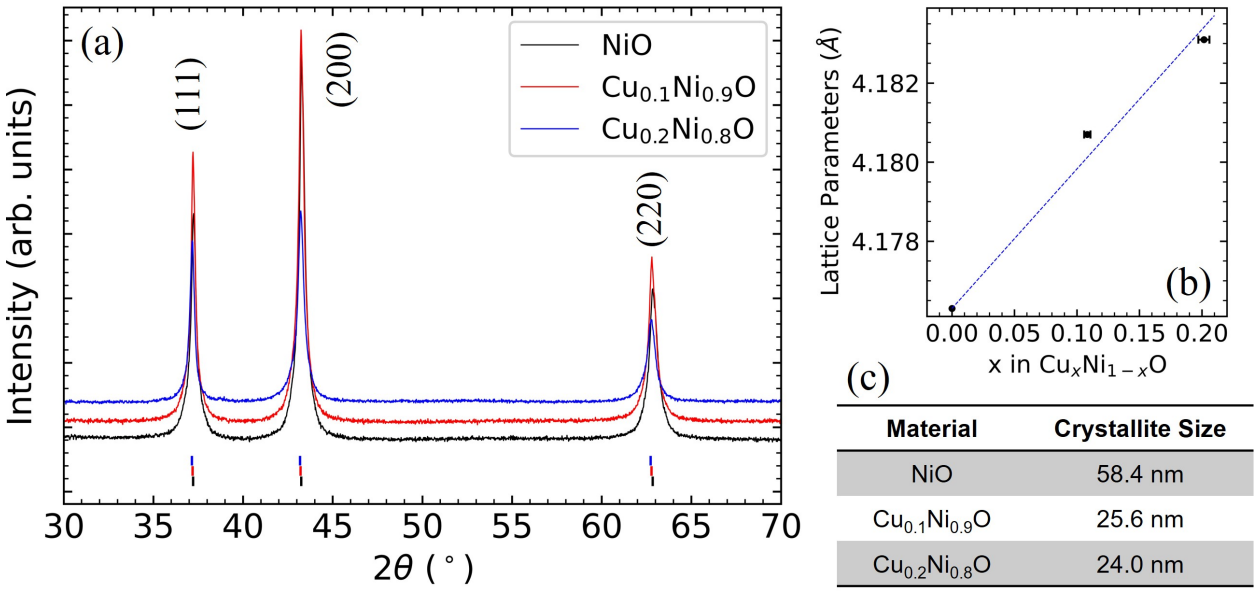
Approximately 15 mg of NiO was packed into a 6 mm diameter porous ceramic cup. Samples were heated in air at 250 °C for 2h, then degassed for 2 days under the select carrier gas (ZA or He). One sample was heated to 500 °C. Once cool enough to handle, the sample was transferred to the DRIFTS cell, warmed to 90 °C, then cooled to 25 °C once sealed to reduce atmospheric water. The samples were purged in the DRIFTS cell until the signal stabilized (2 to 3 h) showing that the sample had equilibrated with the carrier gas. After equilibrium was attained, the carrier gas was diverted through the saturator cell to begin dosing. The sample was dosed for 2 h, with scans obtained every 90 s. All dosed spectra were subtracted from the scan prior to dosing, meaning that any positive peaks occurred from new species on the surface.

5.3 Results and Discussion

5.3.1 Material Characterization

Understanding mesoporous materials requires the use of a variety of techniques that can probe both bulk and surface properties. Atomic percentages were determined through electron-dispersive X-ray spectroscopy (EDS), with values shown in Table 7.A4. Measured EDS values are similar to the desired mole ratio. Figure 5.4 shows the XRD pattern of the synthesized mesoporous metal oxides (MMOs), with the lattice parameters and crystallite size calculated from Rietveld refinement. Pure NiO is green, but the synthesized material is dark grey. XRD reveals the bulk material is NiO, this indicates the surface is non-stoichiometric due to defects [161]. $Cu_xNi_{1-x}O$ remained a solid solution up to $x \leq 20\%$, and at 25% copper begins to phase separate into CuO. Since copper is a larger cation than nickel, as Cu becomes incorporated into the material we expect to see an expansion of the lattice which is seen in the XRD pattern as the reflections shift to lower 2θ, known as Vegard's Law. Lattice expansions or contractions will be linear to the dopant levels, as

shown in Figure 5.4(b). This shows copper is incorporated within the mesoporous material. The XRD pattern exhibits peak broadening due to the small crystallite size, which is common in mesoporous metal oxides. The average crystallite size for NiO is estimated to be 58.4 nm, whereas for $Cu_xNi_{1-x}O$ the average crystallite size is ≈25 nm. With the addition of the dopant, the natural self-assembly of the NiO crystal is disrupted.



(c)

Material	Crystallite Size
NiO	58.4 nm
$Cu_{0.1}Ni_{0.9}O$	25.6 nm
$Cu_{0.2}Ni_{0.8}O$	24.0 nm

Figure 5.4: (a) Powder X-ray diffraction patterns of MMOs NiO, $Cu_{0.1}Ni_{0.9}O$ and $Cu_{0.2}Ni_{0.8}O$, showing a solid solution with no phase separation. The calculated lattice parameters (b) of the expanding crystal structure due to the larger cation, and (c) the calculated crystallite sizes from Rietveld refinements.

To determine whether the materials were successfully templated from the KIT-6 silica, electron microscopy and small angle X-ray scattering (SAXS) were used. Transmission electron microscopy (TEM) and scanning electron microscopy (SEM) images are shown in Figure 5.5. The MMOs show a porous structure that is consistent with materials templated with KIT-6. The synthesized material formed polydispersed particles that ranged from approximately 100 nm to 300 nm in diameter. Through TEM, the pore walls are approximated to be 10 nm. Through SAXS, the mesosporous structure was further confirmed and is plotted in Figure 5.6. The pattern consists of one strong peak and one weaker shoulder. Although the structure cannot be confirmed with only 2

peaks, the combination of TEM and SEM images showing the material was successfully templated with the KIT-6 silica. The material belongs to the $Ia\bar{3}d$ space group, making the corresponding reflections the (211) and (220) facets.

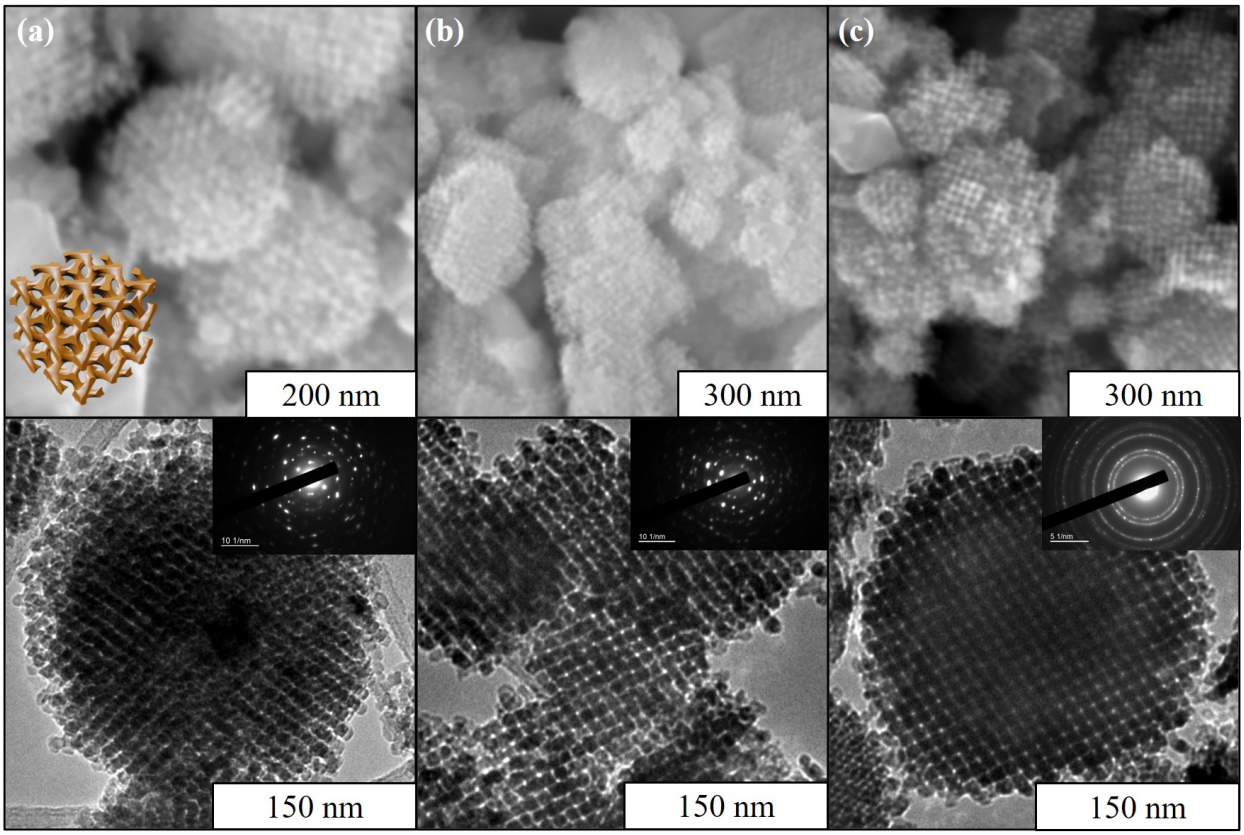


Figure 5.5: Electron microscopy and diffraction patterns of the MMOs in this study. The TEM and SEM correspond to (a) NiO, (b) $Cu_{0.1}Ni_{0.9}O$ and (c) $Cu_{0.2}Ni_{0.8}O$. All materials are crystalline and maintain the inverse structure of KIT-6.

In heterogeneous chemistry, reactions only occur on the surface of a material. Therefore, surface characterization is important. Nitrogen adsorption is used to measure a material's available surface area and pore size distribution. The adsorption data and analysis are shown in Figure 5.7, and the calculated values are summarized in Table 5.1. All MMOs have an isotherm consistent with KIT-6 templated materials and an H3-type hysteresis which indicates the material contains nanoparticles or forms in aggregates like nanoparticles. This is consistent with what was seen in

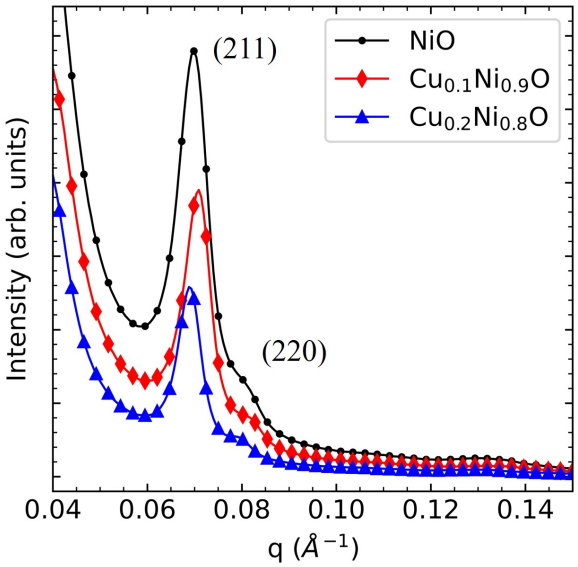


Figure 5.6: SAXS pattern of the synthesised NiO, $Cu_{0.1}Ni_{0.9}O$ and $Cu_{0.2}Ni_{0.8}O$ showing the material has a repeating structure. Since this material was tempalted with KIT-6 the first reflection is attributed to the (211) reflection

TEM and SEM images, where the mesostructure forms particles. The MMOs maintained a high surface area with values between 67.89 to 94.38 m^2/g. The pore size distribution shows a bimodal material with the main structure with a pore size at $\sim$2.4 nm and a secondary pore structure formed by the nanoparticles with a pore size of $\sim$18 nm.

Table 5.1: Consolidation of characteristics for NiO and $Cu_xNi_{1-x}O$ as obtained from nitrogen adsorption measurements.

Material	**Surface Area (m^2/g)**	**Average Pore Size (nm)**	**Pore Volume (cm^3/g)**
NiO	94.38	6.61	0.135
x = 10%	72.86	6.68	0.104
x = 20%	67.89	7.03	0.096

To learn more about the Lewis and Brønsted acidic properties of the surface, the MMOs were exposed to pyridine and examined through IR spectroscopy. Pyridine is a Lewis base that when adsorbed to the surface will result in distinct shifts in the ν8a and ν19b (C-C-N) bands. On Lewis

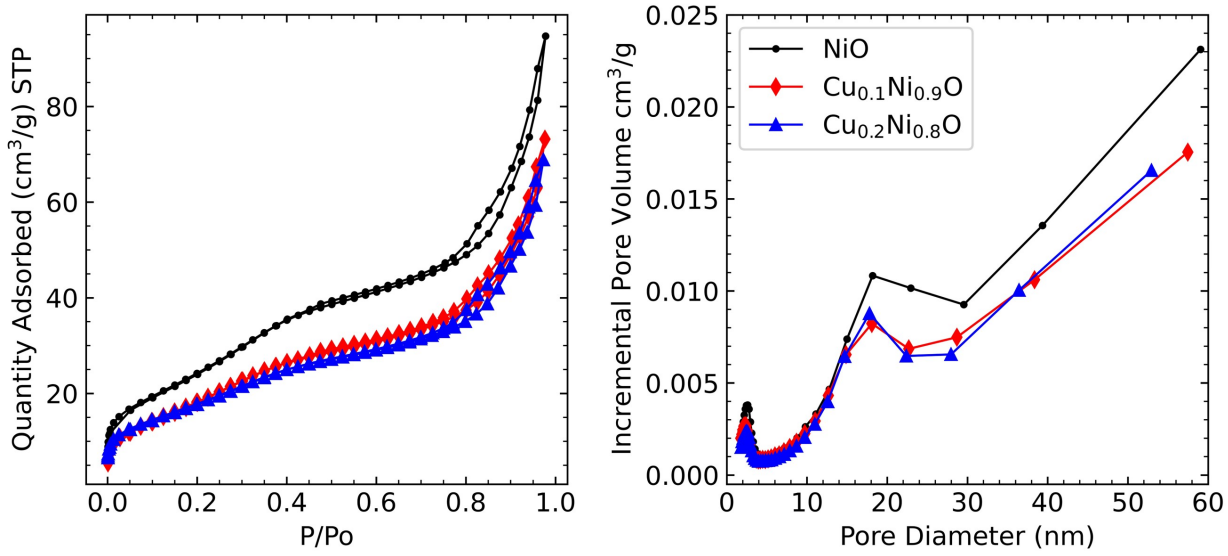


Figure 5.7: Nitrogen adsorption isotherms (left) of NiO, $Cu_{0.1}Ni_{0.9}O$ and $Cu_{0.2}Ni_{0.8}O$, showing an adsorption pattern and hysteresis consistent with KIT-6 templated materials. The pore size distribution (right), shows the main pore size is ∼2.4 nm, but is bimodal with a secondary pore size of ∼18 nm.

acid sites (LPy), the ν8a and ν19b modes adsorb between 1630 to 1600 cm^{-1} and 1465 to 1445 cm^{-1}, respectively. Stronger Lewis acid sites will result in a blue shift in the peak. Brønsted acid sites (BPy) typically adsorb between 1640 to 1630 cm^{-1} and 1540 to 1500 cm^{-1}. If pyridine hydrogen bonds (HPy) to the surface, ν8a and ν19b mode will adsorb between 1600-1580 cm^{-1} and 1447-1440 cm^{-1} [134, 137–140].

The synthesized MMOs were exposed to pyridine vapor and the examined using DRIFTS. The resultant spectra are shown in Figure 5.8, with the spectrum of pyridine adsorbed CuO nanoparticles from Chapter 4 as a reference. NiO exhibits peaks associated with LPy at 1604, 1576, and 1444 cm^{-1} and HPy at 1594 cm^{-1}. $Cu_{0.1}Ni_{0.9}O$ contains the same set of peaks, with reduced intensity for LPy sites and increased intensity for HPy sites. This observation suggests that additional hydroxyls are produced to stabilize the low-level dopant. This scenario is further confirmed by thermogravimetric analysis (TGA), upon heating $Cu_{0.1}Ni_{0.9}O$ exhibits a greater weight loss in mass than the other two MMOs, plotted in Figure 5.9. Unlike in the the doping discussed in Chap-

ter 3, the peak at 1443 cm^{-1} does not broaden for $Cu_{0.1}Ni_{0.9}O$. This fact suggests that copper is not accessible on the surface of the MMO. $Cu_{0.2}Ni_{0.8}O$ regains the LPy peak with the addition of a shoulder. Figure 5.8(b) overlays all peaks around 1443 cm^{-1}. The shoulder on $Cu_{0.2}Ni_{0.8}Os$ appears at 1449 cm^{-1}, which aligns with the LPy site of CuO. This observation suggests that Cu^{2+} is available on the surface on $Cu_{0.2}Ni_{0.8}O$.

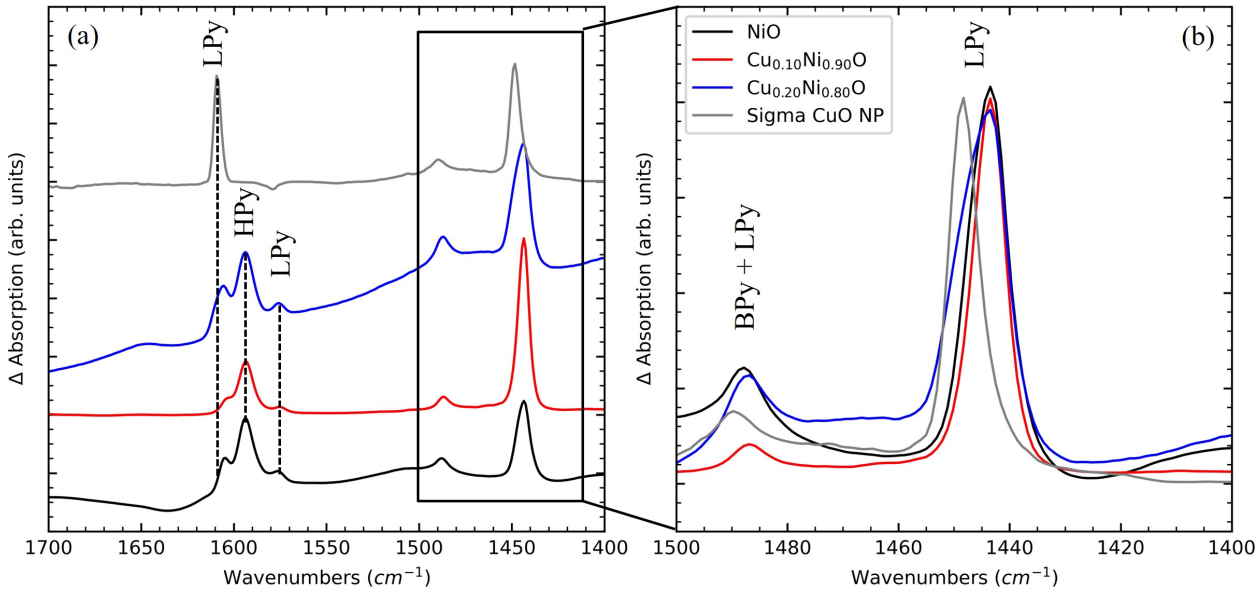


Figure 5.8: Pyridine adsorption DRIFTS difference spectrum of pyridine exposed to NiO, $Cu_{0.1}Ni_{0.9}O$, $Cu_{0.2}Ni_{0.8}O$ and Sigma CuO Nanoparticles. NiO and $Cu_xNi_{1-x}O$ contain Lewis acid sites (LPy) and hydrogen bonding sites (HPy). In the lower region (b) the LPy site for NiO and $Cu_{0.1}Ni_{0.9}O$ are identical suggesting Cu is not lie on the surface, but the bulk. At 20% doping $Cu_{0.2}Ni_{0.8}O$ contains a slight shoulder at 1449 cm^{-1} consistent with CuO. Suggesting at higher doping levels, Cu sites are available on the surface. The assigned modes were derived from literature [134, 137–140].

Cu^{2+} dopant will either replace a Ni^{2+} site or fill a Ni^{2+} vacancy. Cations such as Zn^{2+} and Cr^{3+} have been shown to occupy a nickel vacancy sites [49] reducing the concentration of Ni^{3+}. The Ni^{3+} concentration in NiO has been linked to increased oxidative capabilities. Therefore knowing what site Cu^{2+} occupies will directly affect DFP decomposition. A material's Ni^{3+}/Ni^{2+} concentration can be estimated through Raman spectroscopy [168, 169]. Ni-O has a lattice phonon mode at $\sim$520 cm^{-1}, whereas vacancy sites will have a mode around 470 cm^{-1}. The change in

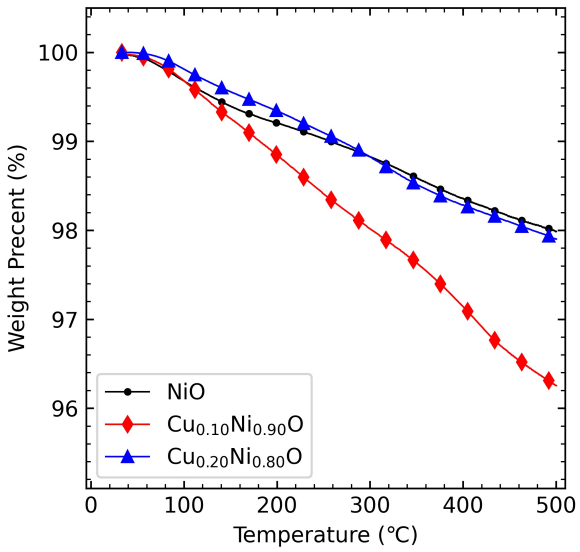


Figure 5.9: TGA curves for NiO, $Cu_{0.1}Ni_{0.9}O$ and $Cu_{0.2}Ni_{0.8}$ showing 10% dopant results in increased weight, which is likely due to additional hydroxyl groups that stabilize the surface.

these peaks will determine a general trend in Ni^{3+} states, and subsequently what sites the Cu^{2+} cations will occupy within the lattice. Figure 5.10 shows Raman spectra for the respective MMOs. Mesoporous NiO exhibits two broad peaks, one at 462 and one at 520 cm^{-1}. $Cu_xNi_{1-x}O$ has an immediate decrease in the low frequency peak, showing that Cu^{2+} decreases Ni^{2+} vacancies upon doping. The peak position and full-width half maximum (FWHM) values are given in Table 5.2.

Table 5.2: The Raman shift peaks (cm^{-1}) and the associated full-width at half maximum (FWHM) for the fitted curves. The Ni^{3+}/Ni^{2+} are approximated ratios from the calculated peak area.

Mesoporous Metal Oxide	Peak/ FWHM	Peak/ FWHM	Ni^{3+}/ Ni^{2+}
NiO	462/122	520/85	66%
$Cu_{0.1}Ni_{0.9}O$	476/115	528/85	19%
$Cu_{0.2}Ni_{0.8}O$	477/115	532/78	18%

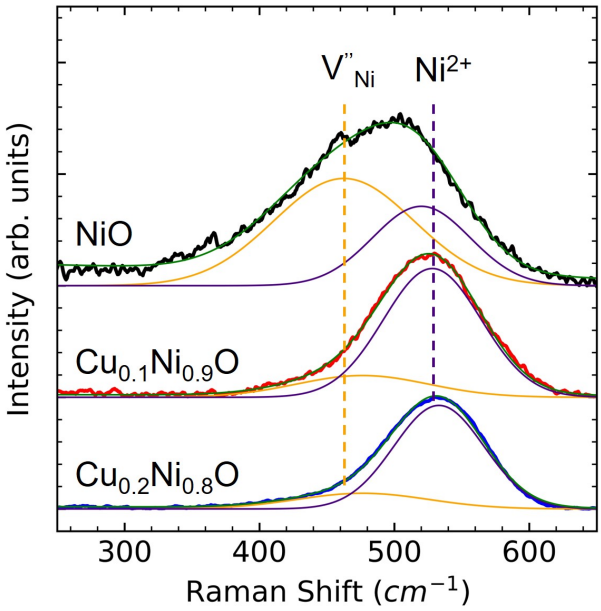


Figure 5.10: Raman spectra of NiO, $Cu_{0.1}Ni_{0.9}O$ and $Cu_{0.2}Ni_{0.8}O$. Upon doping the mode at 460 cm^{-1} significantly decreases, showing Cu^{2+} will fill the Ni^{2+} vacancies.

5.3.2 Adsorption and Decomposition of DFP On NiO in O_2-Rich and O_2-Free atmospheres.

Before diving into the reactivity of DFP with the Cu-doped NiO, we will focus on NiO, as its activity has not yet been explored. Shown in Figure 5.11 are DRIFTS spectra for NiO pretreated at 250 °C, which will be referred to as NiO-250. When exposed to DFP in an O_2-rich environment, we label as NiO-250 ZA and in an O_2-free environment, NiO-250 He. DFP was dosed over 2 h and the assigned vibrational modes were assigned from values in the literature and consolidated in Table 5.3. Spectra for the first 30 min of DFP exposure are plotted in Figure 7.A10. Samples were given adequate time to equilibrate with the carrier gas prior to dosing. However, every experiment resulted in a drift of the spectral background. We attribute the signal drift to the packed bed shifting, which is commonly experienced in DRIFTS experiments.

In the O_2-rich environment, the dominant products for NiO-250 ZA dosed with DFP in the

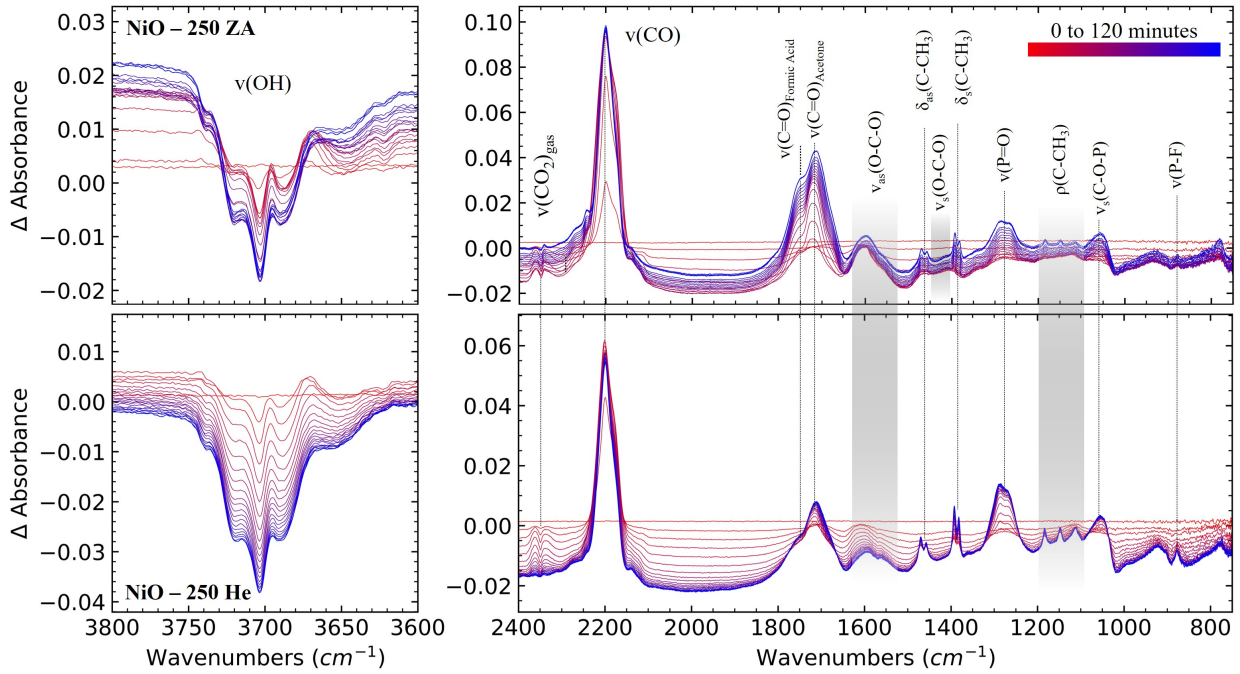


Figure 5.11: DRIFTS difference spectrum of mesoporous NiO heated to 250 °C (NiO-250) exposed to DFP for 2 hours in a O_2 -rich environment (NiO-250 ZA) (Top) and in an O_2 -free environment (NiO-250 He) (bottom) with the assigned modes from literature.

early stages of the reaction are oxidative products CO, CO_2, acetone, formic acid, and carbonates. The first peak appears in 4.5 min at 2200 cm^{-1}, with shoulders at 2214 and 2180 cm^{-1} that are attributed to carbon monoxide ν(CO). The different peaks are attributed to different binding energies on different crystallographic planes. This mode grows rapidly and hits its maximum at 22 min, then slowly decreases throughout the experiment. Although CO is toxic, it is 5000 times less lethal than sarin [77]. To determine where CO adsorbs on clean NiO-250, CO was introduced to NiO-250 at -176 °C. CO adsorbed to NiO displays peaks at 2166 and 2152 cm^{-1} which is consistent with a NiO surface. At temperatures above ∼-150 °C, the CO oxidized.

The CO adsorbed to DFP exposed NiO-250 ZA is stable at room temperature. The temperature stability and blue shift indicate a change in the chemical environment. CO could be coordinated to Ni^{3+} or partially oxidized $Ni^{(2+\delta)+}$ sites. Studies reporting CO adsorption on Ni^{3+} were not available. However, nickel aluminosilicates used for ethylene oligomerization were exposed to CO post-reaction. This study concluded that CO adsorbs on Ni^{2+} ion sites, with spectra features at 2214, 2206, and 2196 cm^{-1} [170]. The CO peak locations, suggest that during DFP decomposition, an intermediate Ni^{2+} ion site is produced and is stabilized through CO adsorption.

The next identifiable mode appears at ∼8 min after DFP dosing, with spectral features at 2361 and 2342 cm^{-1} that are attributed to gas phase carbon dioxide $\nu(CO_2)$gas. These peaks are persistent throughout the experiment. In literature, only a few materials have shown full oxidation of organophosphorus molecules at room temperature. Typically, these reactions require external excitation (UV/Vis light) or noble metals (Au, Pt, Rh) [69, 76, 110, 166, 171]. Within the present study the sample was only exposed to general laboratory light, and full oxidation was observed. Calculations on the decomposition of sarin on other metal oxides show the elimination of propylene is more favorable than the cleavage of the P-F bond [62, 80]. Propylene is highly volatile, and would not be observed by DRIFTS at room temperature. VOCs such as ethylene and toluene have been studied on NiO, and have been shown to oxidize fully to CO_2 [163, 169]. Propylene elimination is likely the most favorable reaction pathway, followed by oxidation to CO and CO_2.

After approximately 12 min of dosing, the next oxidation product appears as a spectral feature at 1713 cm^{-1}, with a shoulder at 1749 cm^{-1}. This region is generally associated with ν(C=O) vibrations, so we assign the peaks to acetone and formic acid, respectively. The peak at 1598 cm^{-1} and shoulder at 1560 cm^{-1} are consistent with the ν_{as}(O-C-O) stretches of formate and carbonate [110, 166]. Carbonates and formates are also seen when pristine NiO-250 was exposed to acetone shown in Figure 7.A11. In prior work, Kiselev et al. proposed a reaction mechanism in which acetone further reacts to form carbonates, which undergoes full oxidation to CO_2 [166]. The same pathway could explain the production of CO_2 on NiO.

In typical experiments using DMMP or sarin, the first modes to appear involve ν(P=O) or, in cases of highly reactive materials, the bridging species ν(O-P-O) [55, 67, 110]. However, with NiO-250 ZA, the reaction occurs so quickly that there are no signs of phosphorous vibrations until intact DFP begins physisorbing to the surface after $\sim$40 min of exposure. Before DFP begins physisorbing, there are weak broad peaks where ν(P=O) and $\nu_{as,s}$(O-P-O) are expected, $\sim$1300 and 1200 to 1060 cm^{-1} respectively. Due to the low intensities of these peaks, we are unable to determine how the phosphorus molecules are sitting on NiO-250 surface through DRIFTS. Once physisorbed, ν(P=O) exhibits peaks at 1286 and 1268 cm^{-1}. In gas phase DFP ν(P=O) appears at 1313 cm^{-1}. This red shift indicates that there are two interaction sites [172]. The sites may indicate different binding strength on different crystallographic surfaces, or the difference between the P=O adsorbing to a hydroxyl versus a Lewis acid site.

To determine the effects of removing oxygen on reactivity and the reaction mechanisms, helium was used as the carrier gas for DFP dosing to produce an O_2-free environment. This experiment is referred to as NiO-250 He (O_2-Free), shown in Figure 5.11. NiO-250 He exposed to DFP forms the same products as NiO-250 ZA (O_2-Rich): CO, CO_2, acetone, formic acid and carbonates. However, the relative amounts of these products decreased significantly for NiO-250 He. This effect is clearly seen in the area and clarity of the peaks for the ν(P=O) and δ_s(C-CH_3) modes compared to the $\nu(C{=}O)_{Acetone}$. This change shows a clear link that surface oxygen plays a role in

driving the decomposition. The reaction likely proceeds with the active oxygen still present on the surface, until the oxygen is fully consumed, after which DFP physisorbs to the surface of NiO-250 He.

To highlight the subtle differences between the two environments, the peaks for the major decomposition products ν(CO) (2200 cm^{-1}), ν(C=O)$_{Acetone}$ (1713 cm^{-1}) and ν_{as}(O-C-O) (1598 cm^{-1}) were normalized to the final absorption intensity of ν(CO) in the respective ZA and He experiments. Due to the shift in the background, the absorption value at 2000 cm^{-1} was used as a "zero point", and subtracted from each peak, which are plotted in Figure 5.12.

Beginning with the carbon monoxide peak, NiO-250 He ν(CO) has three clear phases: 1) initial reaction, 2) rate-limiting step and 3) steady state. The limited surface oxygen is quickly consumed in an O_2-free environment. Therefore, when the reaction moves past the initial exposure, DFP decomposition is rate limited, when compared to the O_2-rich environment. If no surface oxygen is available DFP will physisorb to the surface. NiO-250 ZA ν(CO) moves directly from the initial reaction to steady state, there is no intermediate decrease in reactivity as seen in the O_2-free environment. In an O_2-rich environment, oxygen is always being replenished to the surface, and is readily available to decompose DFP. After $\sim$70 min, both O_2-rich and O_2-free ν(CO) normalized intensity overlap and decrease at the same rate. Once the surface is saturated, regardless of oxygen content, DFP decomposition proceeds at the same rate on mesoporous NiO.

The carbonate peak ν_{as}(O-C-O) in both environments follows the same relative intensity behaviors as the ν(CO) peak, just at a lower intensity. This observation suggests that the formation of CO and carbonate are linked. Kiselev et al., when studying DFP decomposition on TiO_2 under UV illumination, proposed that CO_2 is produced by the oxidation of acetone to various carbonates, followed by further oxidation to CO_2 [166]. Based on NiO's ability to decompose acetone to carbonates, in addition to the clear link between ν(CO) and ν_{as}(O-C-O) following the same intensity profile, we propose that CO can oxidize to CO_2 through a carbonate mediated oxidation pathway.

The main difference between the two test conditions is in the production of acetone ν(C=O)$_{Acetone}$.

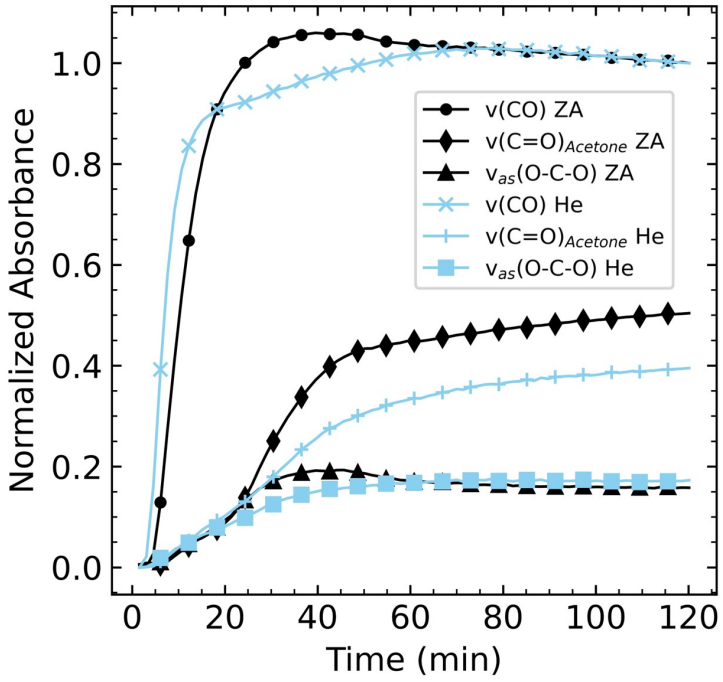


Figure 5.12: Intensity of the main decomposition product peaks of ν(CO) (2200 cm^{-1}), ν(C=O)$_{Acetone}$ (1713 cm^{-1}) and ν_{as}(O-C-O) (1598 cm^{-1}) normalized to the final intensity of the ν(CO) mode. Black corresponds to ZA (O_2-rich) data, and blue corresponds to He (O_2fFree) data.

At the beginning of the experiment, acetone production increased at the same rate in the two different environments, until ∼22 min. As CO production begins to slow, the rate of acetone production in the O_2-rich environment increases, surpassing the normalized acetone produced in the O_2-free environment. Given that different crystallographic facets favor different decomposition products [55, 80], once the lowest energy site/pathway is exhausted, DFP will begin reacting at the remaining sites which favor acetone production. Replenishing surface oxygen increases the regeneration of these facets. As in the case for the ν(CO) peak once the main reaction is complete, the ν(C=O)$_{Acetone}$ peak changes at the same rate regardless of oxygen content.

Table 5.3: Infrared mode assignments (cm^{-1}) of DFP dosed on NiO-250 and NiO-500. Assigned frequencies were derived from *ex-situ* adsorption on NiO-250 shown in supplemental and references [165, 166, 173, 174].

Vibrational Modes	DFP Dosed NiO-250	DFP Dosed NiO-500
v(Ni-F)		819
v(P-F)	878	878
ν_s(C-O-P)	1060	1063
ρ(C-CH_3)	1115, 1148, 1183	1114, 1148, 1183
v(P=O)	1268, 1286	1290
δ_s(C-CH_3)	1382, 1393	1382, 1394
ν_s(O-C-O)	1407	1409, 1426
δ_{as}(C-CH_3)	1457, 1470	1456, 1469
ν_{as}(O-C-O)	1560, 1598	1566, 1593
v(C=O)$_{Acetone}$	1713	1709
v(C=O)$_{Formic\ Acid}$	1749	
v(CO)	2180, 2200, 2214	2176, 2198, 2214
v(CO_2)$_{gas}$	2342	
ν_s(CH)	2881	2888
ν_s(C-CH_3)	2946	2946
ν_{as}(C-CH_3)	2989	2990
v(OH)	3650, 3689, 3704, 3720	3622, 3648, 3885, 3694, 3704

5.3.3 Adsorption and Decomposition of DFP on NiO-250 and $Cu_xNi_{1-x}O$-250 (x = 0.1, 0.2) in an O_2-Rich atmosphere.

Similar to mesoporous NiO, the Cu-doped NiO samples were pretreated at 250 °C in air then placed into zero air to equilibrate. DFP exposed to $Cu_xNi_{1-x}O$-250 ZA (x = 0.1, 0.2), behaves similarily to DFP on NiO-250 ZA, producing similar oxidation products with reduced reactivity. The DRIFTS difference spectra are shown in Figure 5.13. The first ∼20 minutes of DFP exposure on $Cu_xNi_{1-x}O$-250 ZA (x = 0.1, 0.2) are dominated by partial oxidation, with CO peaks appearing at 2198 and 2196 cm^{-1} respectively. Oxidative products, carbonyls and carbonates are also present.

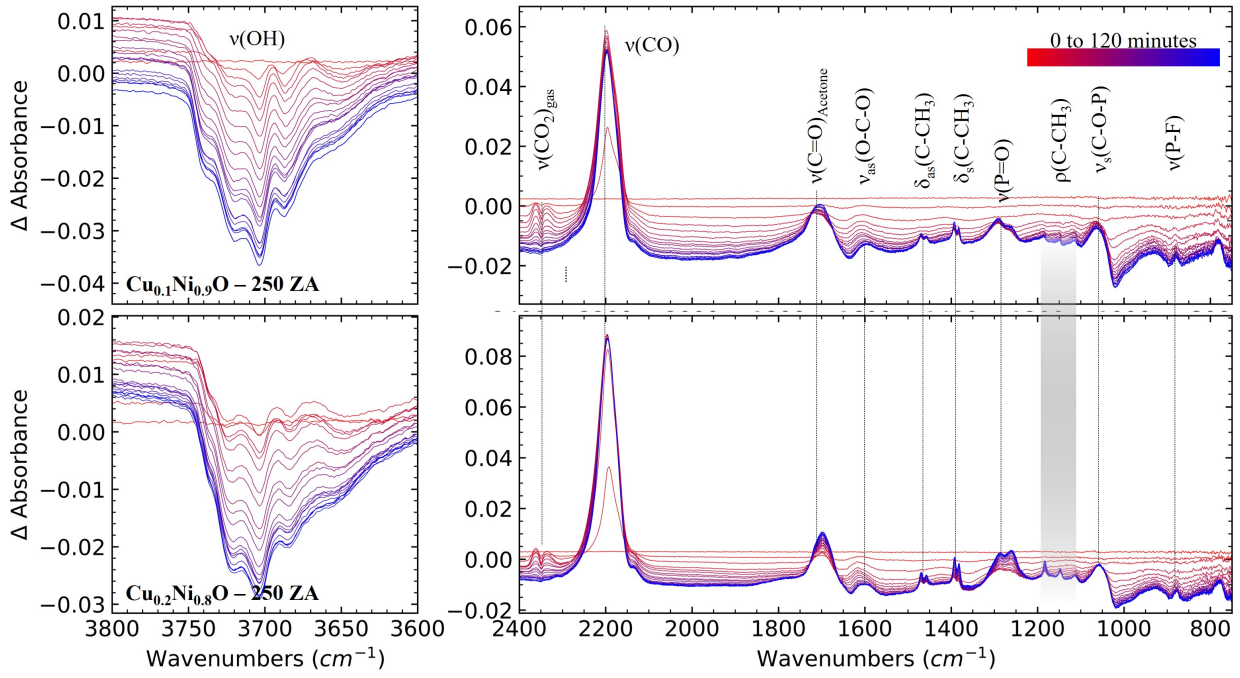


Figure 5.13: DRIFTS difference spectrum of $Cu_{0.1}Ni_{0.9}O$ (top) and $Cu_{0.2}Ni_{0.8}O$ (bottom) heated to 250 °C (MMO-250) and exposed to DFP for 2 h in a O_2-rich environment (MMO-250 ZA) with the assigned modes from literature.

These decomposition products then fully oxidize to produce gas phase CO_2. The main difference lies in the decreased intensity of the carbonyl and carbonate peaks. The intensities of ν(CO), ν(C=O) and ν_{as}(O-C-O) peaks are normalized to the final intensity of CO are plotted in Figure 5.14. Both the ν(C=O) and ν_{as}(O-C-O) peaks increase with exposure, but not at the same rate as NiO-250 ZA. Raman spectroscopy revealed doping with Cu^{2+} fill the Ni^{2+} vacancies, which results in a decrease in the number of Ni^{3+} sites. With fewer Ni^{3+} states, there will be a reduction in active oxygen species. As active oxygen species are a driving factor for DFP decomposition on mesoporous NiO, a reduction in the MMO's ability to produce active oxygen will directly affect DFP decomposition. Based on the decreased activity, the rest of this chapter will be focused on further probing of mesoporous NiO to learn more about its high activity.

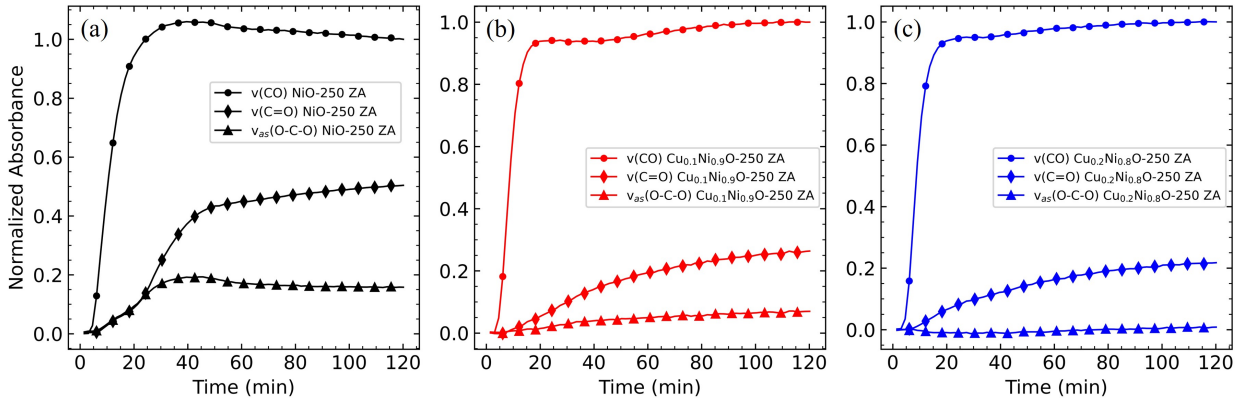


Figure 5.14: Intensity of the main decomposition peaks of ν(CO) and ν(C=O) normalized to the final intensity of the respective experiment ν(CO) mode. (a) Peak tracking for NiO-250 ZA, (b) $Cu_{0.1}Ni_{0.9}O$-250 ZA and (c) $Cu_{0.2}Ni_{0.8}O$-250 ZA.

5.3.4 Low Temperature Dosing

To slow the reaction and potentially learn more about the reaction pathways, we chilled NiO-250 ZA to -50 °C and dosed the sample with DFP. The exposure to DFP lasted for 30 min. The DFP exposed sample was slowly warmed to room temperature in increments of 10 °C, with DRIFTS spectra collected at each step. Although the sample was held at low temperatures, the DRIFTS cell was maintained at 25 °C to minimize DFP physisorption to the cell. At -50 °C, decomposition had already begun, resulting in peaks for CO, carbonyls and carbonates. The ν(CO) mode has two clear peaks at 2196 and 2175 cm^{-1}, corresponding to CO coordinating to Ni^{3+} sites, partially oxidized $Ni^{(2+\delta)+}$ sites or Ni^{2+} ion sites on different crystallographic planes. As the sample was warmed to room temperature, the ν(CO) peak continued to grow. CO_2 production began at 0 °C. There were no prominent ν(P=O) or ν(O-P-O) peaks visible to help us understand how the phosphorus molecule interacts with NiO-250. We further see NiO-250 is highly reactive, decomposing DFP at temperatures as low as -50 °C.

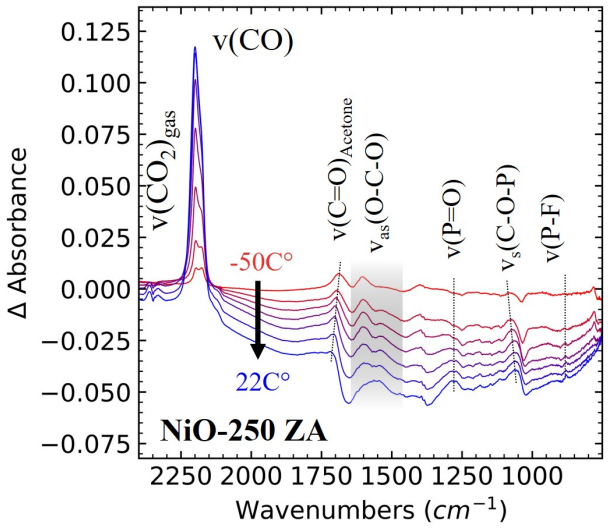


Figure 5.15: DRIFTS difference spectrum of NiO-250 cooled to -50 °C and dosed for 30 min with DFP. The sample was then warmed in increments of 10 °C to room temperature.

5.3.5 Effects of the Pretreatment Temperature

Ren et al. studied KIT-6 templated NiO for CO, oxidation and found that a pretreatment temperature of 400 °C resulting in a more active material, with a T_{50} (temperature to degrade 50% of CO) of 39 °C, NiO pretreated at 200 °C resulted in a T_{50} of 181 °C [164]. To explore the effects of the pretreatment temperature, NiO was heated to 500 °C for 2 h, which will be referred to as NiO-500. To characterize the changes in the surface from the pretreatment temperatures DRIFTS spectra of the material, CO adsorption spectra, and pyridine adsorption spectra were all utilized (Figure 5.16).

Through DRIFTS, the most noticeable change between NiO-250 and NiO-500 is in the hydroxyl region. Hydroxyl groups can be determined to levels of coordination based on their adsorption frequency. NiO's terminal hydroxyl groups absorb around 3735 cm^{-1}, whereas penta coordinated hydroxyl groups absorb around 3630 cm^{-1} [175]. Heating results in a clear loss of low coordinated hydroxyls at 3720 and 3739 cm^{-1}. Pretreatment resulted in no changes in pyridine

adsorption to the Lewis acid sites (LPy) with peaks at 1606 and 1577 cm^{-1} [134]. The peak associated with hydrogen bonded pyridine (HPy) at 1594 cm^{-1} decreased in area upon pretreatment, which is consistent with the loss of hydroxyl groups seen in the DRIFTS data. In CO adsorption, both materials exhibit one peak at 2166 cm^{-1} and a shoulder at 2152 cm^{-1}. The peak at 2152 cm^{-1} can be loosely attributed to the (111) facet [176], however with such a small change in area, we do not consider the minor change in surface structure a driving factor for changes in reactivity. The increased pretreatment temperature causes the surface to have fewer low coordinated hydroxyl groups/ terminal hydroxyl groups. Consequently, there is less physisorbed water and fewer contaminants.

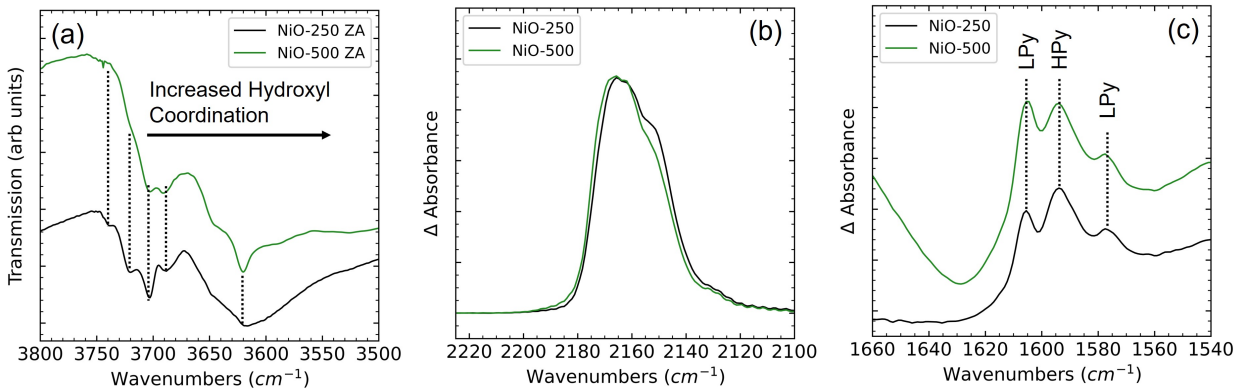


Figure 5.16: Surface characterization of NiO pretreated at 250 and 500 °C. (a) DRIFTS spectra of the hydroxyl region, show that increased heating reduces lower coordinated hydroxyl groups and increases higher coordinated hydroxyl groups. (b) CO adsorption with one peak at 2166 cm^{-1} and a shoulder at 2152 cm^{-1}, showing minimal change between pretreatment temperature. (c) *Ex-situ* pyridine adsorption with three peaks associated with a Lewis acid site (LPy) and hydrogen bonded pyridine (HPy). There is no shift in Lewis acid sites, but there is a decrease in hydrogen bonded pyridine on NiO-500.

DRIFTS difference spectra of NiO-500 ZA dosed with DFP are shown in Figure 5.17. The initial vibrational modes are similar to those on NiO-250, with decomposition products including CO, acetone, and carbonates. Similar to NiO-250 ZA, the peak at 2198 cm^{-1} corresponds to CO that is coordinated to Ni^{3+} sites, partially oxidized $Ni^{(2+\delta)+}$ sites or Ni^{2+} ion site. The peak at 1708 cm^{-1} corresponds to ν(C=O)$_{acetone}$. The carbonate peaks ν(O-C-O) grow in at 1600 and

1426 cm^{-1} then red shift to 1593 and 1409 cm^{-1}. We attribute this shift to conversion of different forms of carbonates on the surface. The three main differences between pretreating at 500 and 250 °C are: 1) the rate at which the products form, 2) the formation of the Ni-F bond, and 3) the lack of formation of CO_2 and formic acid. The main decomposition peaks of NiO-500 ZA and NiO-250 ZA were again normalized to the final intensity of ν(CO) and plotted in Figure 7.A13.

Based on the absorption intensity of the ν(CO) and $\nu(C{=}O)_{Acetone}$ peaks, the DFP decomposition on NiO-500 proceeds more slowly than that of NiO-250. However, the reaction is more sustained over two hours of DFP exposure, as compared to NiO-250. At the early stages of dosing on NiO-500, acetone is the major product. After 40 min of DFP exposure, the rate of CO production out paces that of acetone. These observations are in contrast to NiO-250, where CO is formed rapidly but plateaus quickly and then decreases. Without the terminal hydroxyl groups and water, the initial DFP adsorption interactions are altered.

The second difference involves the peak that appears at 819 cm^{-1}. This peak is attributed to the ν(Ni-F) mode. NiO exposed to HF vapor also forms a new vibration at 819 cm^{-1} which supports this peak assignment. NiO-500 contains undercoordinated Ni sites, which allows for the adsorption of fluorine onto which suggests fluorine leaves as HF on NiO-250.

Last, NiO-500 did not produce formic acid, which can be attributed to the lack of terminal hydroxyl groups on this material. Without terminal hydroxyl groups, decomposition products were unable to form formic acid. The lack of observed CO_2 is surprising, based on the CO oxidation experiment by Ren et al. [164]. Dosing with DFP will form different species on the surface than does CO dosing. The Ni-F bonds could block active sites that are important for oxidation.

5.3.6 Proposed Decomposition Pathway

Figure 5.19 shows the decomposition products and the proposed/decomposition pathways of DFP on mesoporous NiO. Numbers were added to different pathways to simplify discussion. Since

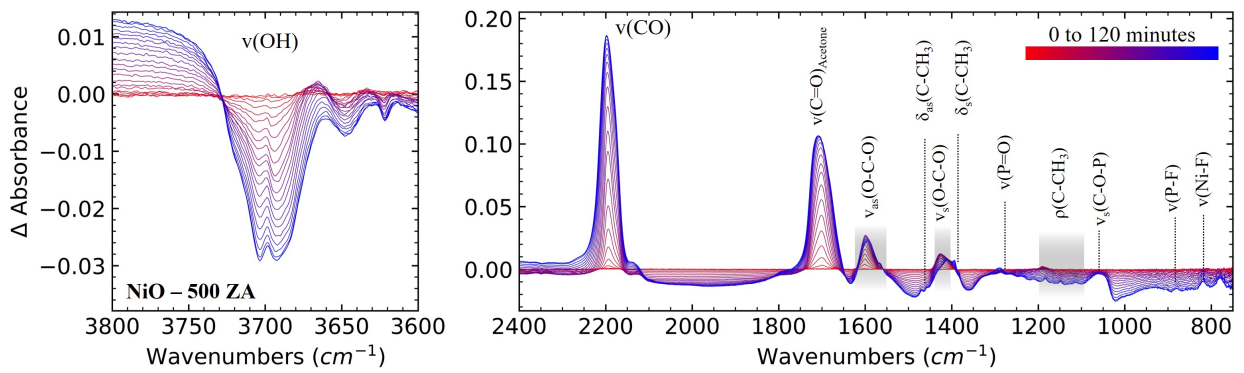


Figure 5.17: DRIFTS difference spectra of NiO pretreated at 500 °C (NiO-500) exposed to DFP in ZA over 2 hours.

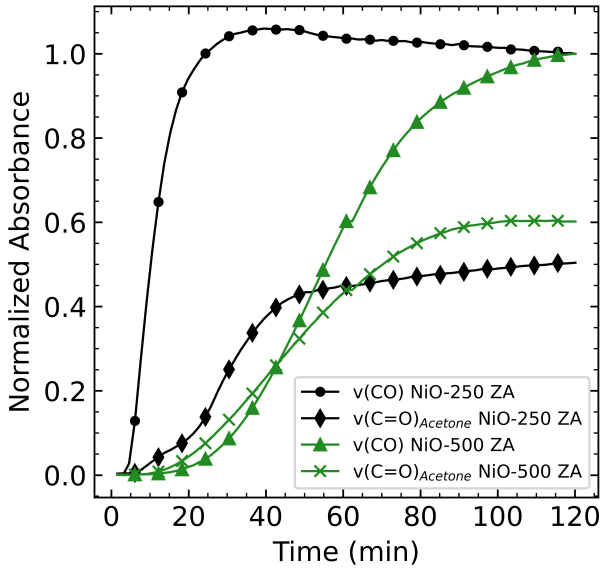


Figure 5.18: Intensity of the main decomposition peaks of ν(CO) and $\nu(C{=}O)_{Acetone}$ normalized to the final intensity of the respective experiment v(CO) mode. Black corresponds to NiO-250 ZA data, while green corresponds to NiO-500 ZA data.

the reaction occurs so quickly, there is little evidence regarding how DFP interacts with the surface and what the remaining phosphorus molecule looks like after the reaction. However, organophosphorus molecules typically interact with the metal center through the P=O bond or interactions between surface hydroxyl groups and the phosphorus [77]. For the reaction to occur, active oxygen must be present, as shown through the reduction in reactivity with NiO-250 He. If active

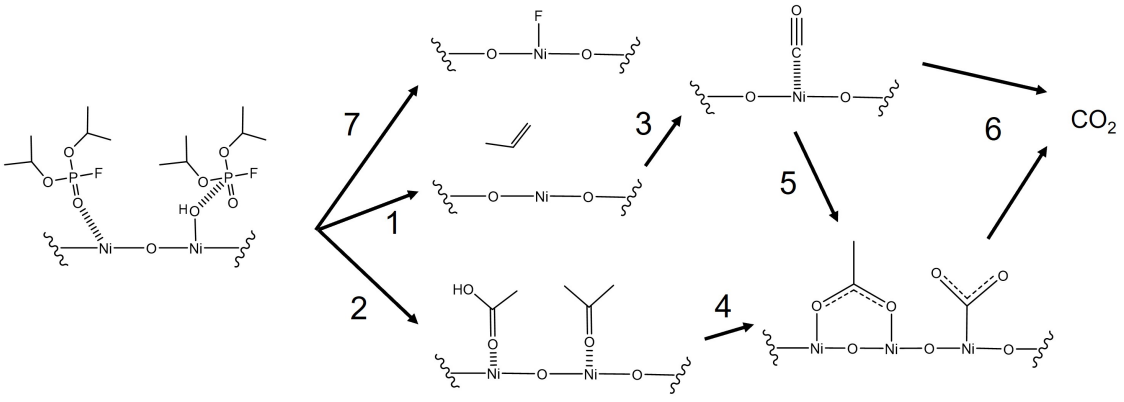


Figure 5.19: Proposed decomposition pathway of DFP on mesoporous NiO.

oxygen is not present, DFP physisorbs to the surface.

In the first mechanistic pathway 1-3-6, as numbered in Figure 5.19, DFP interacts with a facet that favors isopropyl elimination over breaking the P-F, bond producing gas phase propylene [80]. The NiO surface can then oxidize propylene to CO, which is coordinated to Ni^{3+} sites, partially oxidized $Ni^{(2+\delta)+}$ sites or Ni^{2+} ion sites. CO is then further oxidized to CO_2 with the assistance of terminal hydroxyl groups or water [163, 169]. Figure 5.12 shows the intensity of the major decomposition peaks revealing that the ν(CO) and ν_{as}(O-C-O) peak, follow the same behavior. This observation suggests that CO goes through a carbonate mediated step before being released as CO_2, through pathway 5-6.

The next major pathway 2-4-6 shows the decomposition of DFP to carbonyl products to CO_2 through a carbonate mediated step. If terminal hydroxyl groups are available, formic acid and acetone may be produced; if not, then only acetone is produced. The role of terminal hydroxyl groups in formic acid production is made clear through the difference in the DFP decomposition of NiO-500 ZA and NiO-250 ZA, where NiO-500 ZA only produces acetone. From the carbonyls to carbonates and formates, as observed through acetone adsorption shown in Figure 7.A11. Finally, pathway 7 produces the Ni-F bond which is only seen in NiO-500, due to under coordinated Ni sites.

5.3.7 Soman Decomposition

To determine whether DFP reactivity is correlated with CWA decomposition, $\sim$3 μL of the nerve agent soman was sealed in a vial with mesoporous NiO for 24 h. Afterward, the sample was dispersed in solvent, extracted, and examined using mass spectrometry. After 24 h, 81% of the exposed soman was decomposed. Assuming that the surfaces contain the most stable surfaces (111), (110), and (100), the range of possible sites per area can be calculated. Because we did not synthetically control the surface there is a distribution of all the possible facets. Based on the material's weight and surface area, approximately 30-48% of possible sites were consumed. This result is consistent with the spectroscopic data, once the initial reaction occurs, the surface becomes deactivated from byproducts remaining on the surface. The soman decomposition also shows NiO is reactive with both DFP and the live agent soman.

5.4 Conclusion

Mesoporous NiO and $Cu_xNi_{1-x}O$ (x = 0.1 and 0.2) were successfully synthesized and characterized using different bulk and surface sensitive techniques. Based on X-ray diffraction, the Cu^{2+} cation was successfully incorporated into the NiO lattice while retaining crystallinity. Electron microscopy and nitrogen isotherms demonstrate that the MMOs were mesoporous, with large specific surface areas (67.89 to 94.38 m^2/g). Raman spectroscopy revealed that Cu^{2+} reduces Ni^{2+} vacancy sites, which in turn reduces the Ni^{3+} concentration within $Cu_xNi_{1-x}O$. To stabilize the dopant, $Cu_{0.1}Ni_{0.9}O$ exhibited by increased surface hydroxyl group concentration, which blocks Lewis acid sites. At 20% dopant, pyridine adsorption revealed that Lewis acid sites attributed to copper are accessible to the surface.

Mesoporous NiO was shown to be highly active for the decomposition of the CWA simulant DFP, quickly degrading DFP to CO, carbonyls and carbonates which were fully oxidized to CO_2.

After the initial reaction the surface becomes deactivated and DFP physisorbs. Through testing NiO-250 under an oxygen-rich (ZA) and oxygen-poor (He) conditions, we showed the importance of surface oxygen in decomposing DFP. The lack of surface oxygen results in the reaction quickly becoming rate limiting and decomposing less DFP. $Cu_xNi_{1-x}O$ (x = 0.1 and 0.2) have similar decomposition products to NiO, but exhibited reduced reactivity. Placing the Cu^{2+} into a Jahn-Teller active geometry appears to have minimal to no effect compared to NiO. As active oxygen is the important factor in decomposition, Cu^{2+} reducing Ni^{2+} vacancies, the defect concentration that is important for decomposition is diminished.

NiO-250 ZA is the most oxidative material studied here. This material was cooled to -50 °C and exposed to DFP to explore the decomposition mechanism. The activation barrier for DFP decomposition on NiO-250 ZA is so low that decomposition occurred at reduced temperature. Heating NiO to 500 °C resulted in terminal hydroxyl groups being driven off the surface. The lack of terminal hydroxyl groups still resulted partial oxidation, producing CO, acetone, and carbonates. The lack of oxidation to CO_2 is likely due to sites being blocked by Ni-F bond or a secondary effect from reducing terminal hydroxyl groups and water. Mesoporous NiO appears to be one of the most oxidative materials at room temperature for CWA simulant defeat, making this a material of high interest for the filtration and decomposition of CWAs.

Chapter 6: Conclusion

In this dissertation, the goal was to develop and study high surface area metal oxides for the decomposition CWAs and CWA simulants, with a priority to understand the surface interactions that drive decomposition. Each chapter provides a small snapshot to help build the larger picture to create the design rules for effective CWA filters.

In Chapter 3, mesoporous CeO_2, TiO_2 and $Ce_xTi_{1-x}O_2$ (x = 0.005, 0.05, 0.1 and 0.15) were synthesised to probe the effects of cation selection on methyl paraoxon decomposition. Thorough characterization showed that $Ce_xTi_{1-x}O_2$ maintains the anatase crystal structure but loses long-range ordering with increasing dopant concentration. $Ce_xTi_{1-x}O_2$ formed hexagonally packed pores and maintained high specific surface areas (209.41 to 252.61 m^2/g). Pyridine adsorption revealed active Ti and Ce sites on the surface of $Ce_xTi_{1-x}O_2$. When exposed to methyl paraoxon, CeO_2 had a surface-normalized rate constant k_{SA} 3 to 4.6 times larger than those of TiO_2 and $Ce_xTi_{1-x}O_2$. There was minimal difference in the decomposition behavior of TiO_2 and $Ce_xTi_{1-x}O_2$, showing that cation selection between Ti^{4+} and Ce^{4+} is less important to methyl paraoxon decomposition than are other factors, such as crystal structure.

In Chapter 4, dried CuO NPs were exposed to sarin within a high vacuum chamber and monitored *in-situ* with infrared spectroscopy (IR) to bridge simulant work conducted by Lena Trotchaud and colleagues. Sarin initially physisorbs to the surface through the P=O but quickly begins to break down. Red shifts in the δ_s(P-CH_3) and ν(C-O-P) IR peaks indicate cleavage of the P-F bond, producing non-toxic isopropyl methyl phosphonic acid (IMPA). IMPA remains on the surface as a bridging species, as is evident through the growing ν(O-P-O) IR peaks. The data allow

us to infer a decomposition mechanism that matched sarin on dry CuO computational models. A highly reactive material is important. However, CuO NPs become even more interesting with subsequent heating. At $\sim$423 K, the peaks associated with IMPA simultaneously decrease, suggesting IMPA leaves the surface intact, versus decomposing further and poisoning the surface.

Chapter 5 looked to enhance the reactivity of CuO through isovalent substitution of Cu^{2+} into NiO to induce Jahn-Teller distortion. A mesoporous solid solution of $Cu_xNi_{1-x}O$ was successfully synthesized and characterized with bulk and surface sensitive techniques. Diffraction showed that Cu^{2+} was incorporated into the NiO lattice structure and did not phase separate until the dopant exceeded 25%. The MMOs maintained the porous structure from the KIT-6 templating, resulting in high specific surface areas (67.89 to 94.38 m^2/g). Raman spectroscopy revealed that the copper cation reduced nickel vacancies. Upon DFP exposure, the reaction with NiO was dominated by oxidation, primarily producing CO, CO_2, carbonyl, and carbonates. Active oxygen species were the driving factor for this oxidation. The $Cu_xNi_{1-x}O$ series still produced oxidative products, but with reduced activity.

Unsurprisingly, under-coordinated and defective metals are highly active in the decomposition of CWAs and CWA simulants. What is surprising though, is that in the effort to induce more defects or new chemistry through doping, reactivity was either not affected or was negatively impacted. These changes in reactivity comes down to the driving factors for decomposition. TiO_2 does not have a surface that is conducive to decomposition. Therefore, Ce^{4+} within the TiO_2 anatase phase will still comprise a non-ideal surface for methyl paraoxon decomposition. Decomposition of DFP on NiO is driven by active oxygen species, the concentration of which is directly correlated to Ni^{2+} vacancies. Therefore, Cu^{2+} reducing Ni^{2+} vacancies in the material will reduce the driving force for decomposition.

6.1 Future Work

Within this dissertation, mesoporous NiO stood out as a highly active material for CWA decomposition. However, this material is the least understood. If Ni^{3+} is a driving factor in decomposition, then the Ni oxidation can be pushed in both directions to understand the effects of this ion. NiO nanoparticles can be purchased or synthesized, and will contain fewer defects and a more stoichiometric surface. On the opposite spectrum, Ni_2O_3 nanoparticles can be purchased or synthesized, and will contain exclusively Ni^{3+}, although in a different crystal structure. In Chapter 3, we saw the importance of the crystal structure in decomposition. Therefore, Ni_2O_3's different crystal structure cannot be ignored. To maintain the rock salt crystal structure and increase Ni^{3+} concentration, there is only one way, more doping. Researchers have shown that through aliovalent substitution of Li^+ into NiO, the lithium atom will replace a nickel site and not fill the vacancies, leading to an increase in the concentration of Ni^{3+} [168].

Second, an investigation of the decomposition products based on crystallographic planes should be performed. As demonstrated on CeO_2, the (111) facet was the most active for methyl paraoxon and DMMP decomposition [55, 56]. Through synthetically controlling the surface, the most active plane can be identified. Susman et al. developed a method to synthetically control the exposed facet of NiO particles synthetically including the (111), (100), (611) and (311) planes [84]. Through synthesis of these particles and exposure to DFP, the particular planes that drive decomposition may be identified.

CWA simulants are useful tool to learn about a materials potential, without the risks of chemical agent. However, there is always debate on the similarities of simulants to CWAs. There are few studies that discuss the gas-surface interactions of DFP, or its similarities and differences with sarin. It is assumed DFP is similar to sarin, but this issues has not been studied extensively. Within this program several materials have been used to study the gas-surface interactions with sarin, using DRIFTS and transmission IR spectroscopy. These materials include mesoporous CeO_2,

$Y_{0.1}Ce_{0.9}O_2$, $Gd_{0.1}Ce_{0.9}O_2$, TiO_2 and nanoparticles P25 TiO_2 and CuO. As a start, to begin building the library of DFP decomposition knowledge these materials can be examined under identical conditions, which will help reveal the similarities and differences between DFP and sarin.

6.2 Moving Forward

Moving past lessons directly learned from this project, my thoughts on the process have evolved. Conducting fundamental research in this area requires a clear understanding of the material and complete control of the system to isolate all the variables. The necessity for keeping systems simple has led to a majority of studies being conducted in inert atmospheres under basic conditions. Although such studies are essential and should continue to be conducted, more realistic conditions should be included. Such as the effects of oxygen and water on surface interactions. For example had we used an oxygen-free NiO surface initially, little to no reaction would occur, and so the oxidative nature would not have been discovered. Materials that have been deemed unreactive may be active in the presence of oxygen and/or water.

The ideal material for CWA gas filtration is one that is catalytic at room temperature. This task has proven difficult for gas phase CWAs, as most materials remain less than stoichiometric. However, catalysis may be possible with some expectation management. Realistically, water and oxygen will be available to regenerate the surface. Water will favor the production of hydrolysis products, whereas active oxygen species will favor oxidation. Sarin's first and second hydrolysis products are isopropyl methyl phosphonic acid (IMPA) and methyl phosphonic acid (MPA). At 25 °C, the vapor pressures for these compounds are 1.85×10^{-3} and 2×10^{-6} Torr respectively [177], making sarin's decomposition product's vapor pressures 1340 and 1.24 million times less than sarin. Therefore, the only hope for surface regeneration would be a composite material consisting of a weakly adsorbing base and an active material that favors water adsorption over sarin, but that can induce the single hydrolysis product. This approach could avoid bridging species, which would

allow the slow desorption of the decomposition products.

Continued fundamental studies into the surface interactions of CWAs and CWA simulants for advanced filtration materials are necessary to ensure that if the ”bridge” does ever get attacked, we will be prepared.

Bibliography

[1] Johnston, H. *A Bridge Not Attacked Chemical Warfare Civilian Research During World War II*; World Scientific Publishing Company, 2004.

[2] Richardt, D. A.; PhD, D. B. H.; Niemeyer, P. D. B.; Sabath, D. F. CBRN Protection. **2013**,

[3] Sidell, F. R.; Takafuji, E. T.; Franz, D. R. *Medical Aspects of Chemical and Biological Warfare*; 1997.

[4] Johnson, N. H.; Larsen, J. C.; Meek, E. C. Handbook of Toxicology of Chemical Warfare Agents. **2020**, 17–26.

[5] Franca, T. C. C.; Kitagawa, D. A. S.; Cavalcante, S. F. d. A.; Silva, J. A. V. d.; Nepovimova, E.; Kuca, K. Novichoks: The Dangerous Fourth Generation of Chemical Weapons. *International Journal of Molecular Sciences* **2019**, *20*, 1222.

[6] Smart, J. K. History of the Army Protective Mask. **1999**,

[7] Dewey, B. Production of Gas Defense Equipment For the Army. *The Journal of Industrial and Engineering Chemistry* **1919**, *48*, 363–364.

[8] Lodewyckx, P. *Chapter 10 Adsorption of chemical warfare agents*; Interface Science and Technology; 2006; Vol. 7.

[9] Giannakoudakis, D. A.; Bandosz, T. J. Detoxification of Chemical Warfare Agents, From WWI to Multifunctional Nanocomposite Approaches. **2018**,

[10] Suzin, Y.; Buettner, L.; LeDuc, C. Behavior of impregnated activated carbons heated to the point of oxidation. *Carbon* **1998**, *36*, 1557–1566.

[11] Morrison, R. W. Overview of Current Collective Protection Filtration Technology. *U.S. Army Soldier and Biological Chemical Command* **2003**,

[12] Gas Mask and Respirator Wiki. `https://gasmaskandrespirator.fandom.com/wiki/Wiki`.

[13] Small box respirator. https://en.wikipedia.org/wiki/Small_box_respirator#/media/File:British_soldier_in_a_Small_Box_respirator.jpg.

[14] Rossin, J.; Petersen, E.; Tevault, D.; Lamontagne, R.; Isaacson, L. Effects of environmental weathering on the properties of ASC-whetlerite. *Carbon* **1991**, *29*, 197–205.

[15] Holdren, S. Understanding The Surface Chemistry of Gas Phase Organophosphorus Chemical Warefare Agents With Sorbent Materials. 2019.

[16] Richardson, R.; Makhaeva, G. Encyclopedia of Toxicology (Third Edition). *Article Titles: O* **2014**, 714–719.

[17] Su, G.; Letcher, R. J.; Yu, H. Organophosphate Flame Retardants and Plasticizers in Aqueous Solution: pH-Dependent Hydrolysis, Kinetics, and Pathways. *Environmental Science & Technology* **2016**, *50*, 8103–8111.

[18] Lum, K. T.; Huebner, H. J.; Li, Y.; Phillips, T. D.; Raushel, F. M. Organophosphate Nerve Agent Toxicity in Hydra attenuata. *Chemical Research in Toxicology* **2003**, *16*, 953–957.

[19] *Potential Military Chemical/Biological Agents and Compounds FM 3-11.9*; 2005.

[20] Abou-Donia, M. B.; Siracuse, B.; Gupta, N.; Sokol, A. S. Sarin (GB, O-isopropyl methylphosphonofluoridate) neurotoxicity: critical review. *Critical Reviews in Toxicology* **2016**, *46*, 1–31.

[21] Agrawal, M.; Gallis, D. F. S.; Greathouse, J. A.; Sholl, D. S. How Useful Are Common Simulants of Chemical Warfare Agents at Predicting Adsorption Behavior? *The Journal of Physical Chemistry C* **2018**, *122*, 26061–26069.

[22] Ploskonka, A. M.; DeCoste, J. B. Insight into Organophosphate Chemical Warfare Agent Simulant Hydrolysis in Metal-Organic Frameworks. *Journal of Hazardous Materials* **2019**, *375*, 191–197.

[23] Picard, B.; Chataigner, I.; Maddaluno, J.; Legros, J. Introduction to chemical warfare agents, relevant simulants and modern neutralisation methods. *Organic & Biomolecular Chemistry* **2019**, *17*, 6528–6537.

[24] Kumar, P.; Anand, B.; Tsang, Y. F.; Kim, K.-H.; Khullar, S.; Wang, B. Regeneration, degradation, and toxicity effect of MOFs: Opportunities and challenges. *Environmental Research* **2019**, *176*, 108488.

[25] Alezi, D.; Belmabkhout, Y.; Suyetin, M.; Bhatt, P. M.; Weselinski, J.; Solovyeva, V.; Adil, K.; Spanopoulos, I.; Trikalitis, P. N.; Emwas, A.-H.; Eddaoudi, M. MOF Crystal Chemistry Paving the Way to Gas Storage Needs: Aluminum-Based soc-MOF for CH4, O2, and CO2 Storage. *Journal of the American Chemical Society* **2015**, *137*, 13308–13318.

[26] Chen, Z.; Mian, M. R.; Lee, S.-J.; Chen, H.; Zhang, X.; Kirlikovali, K. O.; Shulda, S.; Melix, P.; Rosen, A. S.; Parilla, P. A.; Gennett, T.; Snurr, R. Q.; Islamoglu, T.; Yildirim, T.; Farha, O. K. Fine-Tuning a Robust Metal–Organic Framework toward Enhanced Clean Energy Gas Storage. *Journal of the American Chemical Society* **2021**, *143*, 18838–18843.

[27] Qian, Q.; Asinger, P. A.; Lee, M. J.; Han, G.; Rodriguez, K. M.; Lin, S.; Benedetti, F. M.; Wu, A. X.; Chi, W. S.; Smith, Z. P. MOF-Based Membranes for Gas Separations. *Chemical Reviews* **2020**, *120*, 8161–8266.

[28] Hiraide, S.; Sakanaka, Y.; Kajiro, H.; Kawaguchi, S.; Miyahara, M. T.; Tanaka, H. High-throughput gas separation by flexible metal–organic frameworks with fast gating and thermal management capabilities. *Nature Communications* **2020**, *11*, 3867.

[29] Pascanu, V.; Miera, G. G.; Inge, A. K.; Martin-Matute, B. Metal–Organic Frameworks as Catalysts for Organic Synthesis: A Critical Perspective. *Journal of the American Chemical Society* **2019**, *141*, 7223–7234.

[30] Yang, D.; Gates, B. C. Catalysis by Metal Organic Frameworks: Perspective and Suggestions for Future Research. *ACS Catalysis* **2019**, *9*, 1779–1798.

[31] Safaei, M.; Foroughi, M. M.; Ebrahimpoor, N.; Jahani, S.; Omidi, A.; Khatami, M. A review on metal-organic frameworks: Synthesis and Applications. *TrAC Trends in Analytical Chemistry* **2019**, *118*, 401–425.

[32] Zhou, H.-C.; Long, J. R.; Yaghi, O. M. Introduction to Metal–Organic Frameworks. *Chemical Reviews* **2012**, *112*, 673–674.

[33] DeCoste, J. B.; Peterson, G. W. Metal–Organic Frameworks for Air Purification of Toxic Chemicals. *Chemical Reviews* **2014**, *114*, 5695–5727.

[34] Moon, S.; Liu, Y.; Hupp, J. T.; Farha, O. K. Instantaneous Hydrolysis of Nerve-Agent Simulants with a Six-Connected Zirconium-Based Metal–Organic Framework. *Angewandte Chemie International Edition* **2015**, *54*, 6795–6799.

[35] Chen, Z.; Ma, K.; Mahle, J. J.; Wang, H.; Syed, Z. H.; Atilgan, A.; Chen, Y.; Xin, J. H.; Islamoglu, T.; Peterson, G. W.; Farha, O. K. Integration of Metal–Organic Frameworks on Protective Layers for Destruction of Nerve Agents under Relevant Conditions. *Journal of the American Chemical Society* **2019**, *141*, 20016–20021.

[36] Chen, Z.; Islamoglu, T.; Farha, O. K. Toward Base Heterogenization: A Zirconium Metal–Organic Framework/Dendrimer or Polymer Mixture for Rapid Hydrolysis of a Nerve-Agent Simulant. *ACS Applied Nano Materials* **2019**, *2*, 1005–1008.

[37] Zhao, J.; Lee, D. T.; Yaga, R. W.; Hall, M. G.; Barton, H. F.; Woodward, I. R.; Oldham, C. J.; Walls, H. J.; Peterson, G. W.; Parsons, G. N. Ultra-Fast Degradation of Chemical Warfare Agents Using MOF–Nanofiber Kebabs. *Angewandte Chemie* **2016**, *128*, 13418–13422.

[38] Couzon, N.; Dhainaut, J.; Campagne, C.; Royer, S.; Loiseau, T.; Volkringer, C. Porous textile composites (PTCs) for the removal and the decomposition of chemical warfare agents (CWAs) – A review. *Coordination Chemistry Reviews* **2022**, *467*, 214598.

[39] Zheng, H.-Q.; Zeng, Y.-N.; Chen, J.; Lin, R.-G.; Zhuang, W.-E.; Cao, R.; Lin, Z.-J. Zr-Based Metal–Organic Frameworks with Intrinsic Peroxidase-Like Activity for Ultradeep Oxidative Desulfurization: Mechanism of H2O2 Decomposition. *Inorganic Chemistry* **2019**, *58*, 6983–6992.

[40] Opanasenko, M. V.; Roth, W. J.; Čejka, J. Two-dimensional zeolites in catalysis: current status and perspectives. *Catalysis Science & Technology* **2015**, *6*, 2467–2484.

[41] Hendriks, F. C.; Valencia, D.; Bruijnincx, P. C. A.; Weckhuysen, B. M. Zeolite molecular accessibility and host–guest interactions studied by adsorption of organic probes of tunable size. *Physical Chemistry Chemical Physics* **2016**, *19*, 1857–1867.

[42] Li, Y.; Yu, J. Emerging applications of zeolites in catalysis, separation and host–guest assembly. *Nature Reviews Materials* **2021**, *6*, 1156–1174.

[43] Bellamy, A. J. Reaction of gaseous sulfur mustard with zeolite 13X. *Journal of the Chemical Society, Perkin Transactions 2* **1994**, *0*, 2325–2328.

[44] Wagner, G. W.; Bartram, P. W. Reactions of VX, HD, and Their Simulants with NaY and AgY Zeolites. Desulfurization of VX on AgY. *Langmuir* **1999**, *15*, 8113–8118.

[45] Singh, V. V.; Jurado-Sánchez, B.; Sattayasamitsathit, S.; Orozco, J.; Li, J.; Galarnyk, M.; Fedorak, Y.; Wang, J. Multifunctional Silver-Exchanged Zeolite Micromotors for Catalytic Detoxification of Chemical and Biological Threats. *Advanced Functional Materials* **2015**, *25*, 2147–2155.

[46] Ji, X.; Yao, W.; Peng, J.; Ren, N.; Zhou, J.; Huang, Y. Evaluation of Cu-ZSM-5 zeolites as QCM sensor coatings for DMMP detection. *Sensors and Actuators B: Chemical* **2012**, *166*, 50–55.

[47] Meenu, K.; Kumar, N.; Tiwari, K. R.; Yadav, T.; Tomar, R.; Gupta, A. K. Synthesis and characterization of zeolite Linde Type W and its metal oxide composite Ag-O-LTW used for the decontamination of chemical warfare agent simulant. *Phosphorus, Sulfur, and Silicon and the Related Elements* **2020**, *195*, 1–8.

[48] Védrine, J. C. Metal Oxides in Heterogeneous Oxidation Catalysis: State of the Art and Challenges for a More Sustainable World. *ChemSusChem* **2019**, *12*, 577–588.

[49] Xu, X.; Zhang, H.; Tong, Y.; Sun, Y.; Fang, X.; Xu, J.; Wang, X. Tuning Ni3+ quantity of NiO via doping of cations with varied valence states: The key role of Ni3+ on the reactivity. *Applied Surface Science* **2021**, *550*, 149316.

[50] Wagner, G. W.; Procell, L. R.; O'Connor, R. J.; Munavalli, S.; Carnes, C. L.; Kapoor, P. N.; Klabunde, K. J. Reactions of VX, GB, GD, and HD with Nanosize Al 2 O 3 . Formation of Aluminophosphonates. *Journal of the American Chemical Society* **2001**, *123*, 1636–1644.

[51] Templeton, M. K.; Weinberg, W. H. Adsorption and decomposition of dimethyl methylphosphonate on an aluminum oxide surface. *Journal of the American Chemical Society* **1985**, *107*, 97–108.

[52] Sheinker, V. N.; Mitchell, M. B. Quantitative Study of the Decomposition of Dimethyl Methylphosphonate (DMMP) on Metal Oxides at Room Temperature and Above. *Chemistry of Materials* **2002**, *14*, 1257–1268.

[53] Mitchell, M. B.; Sheinker, V. N.; Mintz, E. A. Adsorption and Decomposition of Dimethyl Methylphosphonate on Metal Oxides. *The Journal of Physical Chemistry B* **1997**, *101*, 11192–11203.

[54] Leonard, M. B.; Li, T.; Kramer, M. J.; McDonnell, S. M.; Vedernikov, A. N.; Rodriguez, E. E. Spectroscopic Studies of Methyl Paraoxon Decomposition over Mesoporous Ce-doped Titanias for Toxic Chemical Filtration. *Journal of Hazardous Materials* **2022**, *438*, 129536.

[55] Li, T.; Tsyshevsky, R.; Algrim, L.; McEntee, M.; Durke, E. M.; Eichhorn, B.; Karwacki, C.; Zachariah, M. R.; Kuklja, M. M.; Rodriguez, E. E. Understanding Dimethyl Methylphosphonate Adsorption and Decomposition on Mesoporous CeO2. *ACS Applied Materials & Interfaces* **2021**, *13*, 54597–54609.

[56] Trenque, I.; Magnano, G. C.; Bolzinger, M. A.; Roiban, L.; Chaput, F.; Pitault, I.; Briançon, S.; Devers, T.; Masenelli-Varlot, K.; Bugnet, M.; Amans, D. Shape-selective synthesis of nanoceria for degradation of paraoxon as a chemical warfare simulant. *Physical Chemistry Chemical Physics* **2019**, *21*, 5455–5465.

[57] Trotochaud, L.; Tsyshevsky, R.; Holdren, S.; Fears, K.; Head, A. R.; Yu, Y.; Karslıoğlu, O.; Pletincx, S.; Eichhorn, B.; Owrutsky, J.; Long, J.; Zachariah, M.; Kuklja, M. M.; Bluhm, H. Spectroscopic and Computational Investigation of Room-Temperature Decomposition of a Chemical Warfare Agent Simulant on Polycrystalline Cupric Oxide. *Chemistry of Materials* **2017**, *29*, 7483–7496.

[58] Mahato, T.; Singh, B.; Srivastava, A.; Prasad, G.; Srivastava, A.; Ganesan, K.; Vijayaraghavan, R. Effect of calcinations temperature of CuO nanoparticle on the kinetics of decontamination and decontamination products of sulphur mustard. *Journal of Hazardous Materials* **2011**, *192*, 1890–1895.

[59] Ma, D.; Cao, Z. Adsorption and Decomposition of Sarin on Dry and Wet Cu2O(111) and CuO(111) Surfaces: Insight from First-Principles Calculations. *The Journal of Physical Chemistry C* **2021**, *125*, 24396–24405.

[60] Trotochaud, L.; Head, A. R.; Büchner, C.; Yu, Y.; Karslıoğlu, O.; Tsyshevsky, R.; Holdren, S.; Eichhorn, B.; Kuklja, M. M.; Bluhm, H. Room temperature decomposition of dimethyl methylphosphonate on cuprous oxide yields atomic phosphorus. *Surface Science* **2019**, *680*, 75–87.

[61] Wagner, G. W.; Bartram, P. W.; Koper, O.; Klabunde, K. J. Reactions of VX, GD, and HD with Nanosize MgO. *The Journal of Physical Chemistry B* **1999**, *103*, 3225–3228.

[62] Tsyshevsky, R.; Head, A. R.; Trotochaud, L.; Bluhm, H.; Kuklja, M. M. Mechanisms of Degradation of Toxic Nerve Agents: Quantum-chemical Insight into Interactions of Sarin and Soman with Molybdenum Dioxide. *Surface Science* **2020**, *700*, 121639.

[63] Head, A. R.; Tsyshevsky, R.; Trotochaud, L.; Yu, Y.; Karslıoğlu, O.; Eichhorn, B.; Kuklja, M. M.; Bluhm, H. Dimethyl methylphosphonate adsorption and decomposition on MoO2 as studied by ambient pressure x-ray photoelectron spectroscopy and DFT calculations. *Journal of Physics: Condensed Matter* **2018**, *30*, 134005.

[64] Head, A. R.; Tsyshevsky, R.; Trotochaud, L.; Yu, Y.; Kyhl, L.; Karslıoğlu, O.; Kuklja, M. M.; Bluhm, H. Adsorption of Dimethyl Methylphosphonate on MoO 3 : The Role of Oxygen Vacancies. *The Journal of Physical Chemistry C* **2016**, *120*, 29077–29088.

[65] McEntee, M.; Gordon, W. O.; Balboa, A.; Delia, D. J.; Pitman, C. L.; Pennington, A. M.; Rolison, D. R.; Pietron, J. J.; DeSario, P. A. Mesoporous Copper Nanoparticle/TiO 2 Aerogels for Room-Temperature Hydrolytic Decomposition of the Chemical Warfare Simulant Dimethyl Methylphosphonate. *ACS Applied Nano Materials* **2020**, *3*, 3503–3512.

[66] Rusu, C. N.; Yates, J. T. Adsorption and Decomposition of Dimethyl Methylphosphonate on TiO2. *The Journal of Physical Chemistry B* **2000**, *104*, 12292–12298.

[67] Panayotov, D. A.; Morris, J. R. Thermal Decomposition of a Chemical Warfare Agent Simulant (DMMP) on TiO2: Adsorbate Reactions with Lattice Oxygen as Studied by Infrared Spectroscopy. *The Journal of Physical Chemistry C* **2009**, *113*, 15684–15691.

[68] Li, T.; Tsyshevsky, R.; McEntee, M.; Durke, E. M.; Karwacki, C.; Rodriguez, E. E.; Kuklja, M. M. Titania Nanomaterials for Sarin Decomposition: Understanding Fundamentals. *ACS Applied Nano Materials* **2022**,

[69] Panayotov, D. A.; Morris, J. R. Catalytic Degradation of a Chemical Warfare Agent Simulant: Reaction Mechanisms on TiO2-Supported Au Nanoparticles. *The Journal of Physical Chemistry C* **2008**, *112*, 7496–7502.

[70] Tang, X.; Hicks, Z.; Ganteför, G.; Eichhorn, B. W.; Bowen, K. H. Adsorption and Decomposition of DMMP on Size-Selected (WO3)3 Clusters. *ChemistrySelect* **2018**, *3*, 3718–3721.

[71] Gordon, W. O.; Tissue, B. M.; Morris, J. R. Adsorption and Decomposition of Dimethyl Methylphosphonate on Y2O3 Nanoparticles. *The Journal of Physical Chemistry C* **2007**, *111*, 3233–3240.

[72] Holdren, S.; Tsyshevsky, R.; Fears, K.; Owrutsky, J.; Wu, T.; Wang, X.; Eichhorn, B. W.; Kuklja, M. M.; Zachariah, M. R. Adsorption and Destruction of the G-Series Nerve Agent Simulant Dimethyl Methylphosphonate on Zinc Oxide. *ACS Catalysis* **2018**, *9*, 902–911.

[73] Tsyshevsky, R.; Holdren, S.; Eichhorn, B. W.; Zachariah, M. R.; Kuklja, M. M. Sarin Decomposition on Pristine and Hydroxylated ZnO: Quantum-Chemical Modeling. *The Journal of Physical Chemistry C* **2019**, *123*, 26432–26441.

[74] Denchy, M. A.; Wang, L.; Blando, N.; Hansen, L.; Bilik, B. R.; Tang, X.; Hicks, Z.; Gantefoer, G.; Bowen, K. H. Adsorption and Decomposition of Dimethyl Methylphosphonate on Size-Selected Zirconium Oxide Trimer Clusters. *The Journal of Physical Chemistry C* **2021**, *125*, 23688–23698.

[75] Adamson, R. H. The acute lethal dose 50 (LD50) of caffeine in albino rats. *Regulatory Toxicology and Pharmacology* **2016**, *80*, 274–276.

[76] Ekerdt, J. G.; Klabunde, K. J.; Shapley, J. R.; White, J. M.; Yates, J. T. Surface chemistry of organophosphorus compounds. *The Journal of Physical Chemistry* **1988**, *92*, 6182–6188.

[77] Mukhopadhyay, S.; Schoenitz, M.; Dreizin, E. L. Vapor-phase decomposition of dimethyl methylphosphonate (DMMP), a sarin surrogate, in presence of metal oxides. *Defence Technology* **2020**, *17*, 1095–1114.

[78] Denet, E.; Espina-Benitez, M. B.; Pitault, I.; Pollet, T.; Blaha, D.; Bolzinger, M.-A.; Rodriguez-Nava, V.; Briançon, S. Metal oxide nanoparticles for the decontamination of toxic chemical and biological compounds. *International Journal of Pharmaceutics* **2020**, *583*, 119373.

[79] Kuiper, A.; Bokhoven, J. v.; Medema, J. The role of heterogeneity in the kinetics of a surface reaction I. Infrared characterization of the adsorption structures of organophosphonates and their decomposition. *Journal of Catalysis* **1976**, *43*, 154–167.

[80] Tsyshevsky, R.; McEntee, M.; Durke, E. M.; Karwacki, C.; Kuklja, M. M. Degradation of Fatal Toxic Nerve Agents on Dry TiO2. *ACS Applied Materials & Interfaces* **2021**, *13*, 696–705.

[81] National Center for Biotechnology Information (2022). PubChem Compound Summary for CID 196996, Methylphosphonfluoridate. `https://pubchem.ncbi.nlm.nih.gov/compound/Methylphosphonfluoridate`.

[82] Ederer, J.; Janoš, P.; Šťastný, M.; Henych, J.; Ederer, K.; Slušná, M. ; Tolasz, J. Nanocrystalline cerium oxide for catalytic degradation of paraoxon methyl: Influence of CeO2 surface properties. *Journal of Environmental Chemical Engineering* **2021**, *9*, 106229.

[83] Suntivich, J.; Gasteiger, H. A.; Yabuuchi, N.; Nakanishi, H.; Goodenough, J. B.; Shao-Horn, Y. Design principles for oxygen-reduction activity on perovskite oxide catalysts for fuel cells and metal–air batteries. *Nature Chemistry* **2011**, *3*, 546–550.

[84] Susman, M. D.; Pham, H. N.; Zhao, X.; West, D. H.; Chinta, S.; Bollini, P.; Datye, A. K.; Rimer, J. D. Synthesis of NiO Crystals Exposing Stable High-Index Facets. *Angewandte Chemie International Edition* **2020**, *59*, 15119–15123.

[85] Dey, S.; Mehta, N. Oxidation of Carbon monoxide over various nickel oxide catalysts in different conditions: A Review. *Chemical Engineering Journal Advances* **2020**, *1*, 100008.

[86] Gawande, M. B.; Pandey, R. K.; Jayaram, R. V. Role of mixed metal oxides in catalysis science—versatile applications in organic synthesis. *Catalysis Science & Technology* **2012**, *2*, 1113–1125.

[87] Cuenya, B. R. Synthesis and catalytic properties of metal nanoparticles: Size, shape, support, composition, and oxidation state effects. *Thin Solid Films* **2010**, *518*, 3127–3150.

[88] Zarschler, K.; Rocks, L.; Licciardello, N.; Boselli, L.; Polo, E.; Garcia, K. P.; Cola, L. D.; Stephan, H.; Dawson, K. A. Ultrasmall inorganic nanoparticles: State-of-the-art and perspectives for biomedical applications. *Nanomedicine: Nanotechnology, Biology and Medicine* **2016**, *12*, 1663–1701.

[89] Chen, Q.-S.; Vidal-Iglesias, F. J.; Solla-Gullón, J.; Sun, S.-G.; Feliu, J. M. Role of surface defect sites: from Pt model surfaces to shape-controlled nanoparticles. *Chemical Science* **2011**, *3*, 136–147.

[90] Wong, M. Nanoparticles and Catalysis. Edited by Didier Astruc. *Angewandte Chemie International Edition* **2008**, *47*, 7795–7795.

[91] Zhao, D.; Wan, Y.; Zhou, Y. *Ordered Mesoporous Materials*; Wiley-VCH, 2013.

[92] Page, M. L.; Beau, R.; MassyDuchene,; Duchene, J.; Maison-Alfort, Porous Silica Particles Containing a Crystallized Phase and Method. 1967.

[93] Kresge, C. T.; Leonowicz, M. E.; Roth, W. J.; Vartuli, J. C.; Beck, J. S. Ordered mesoporous molecular sieves synthesized by a liquid-crystal template mechanism. *Nature* **1992**, *359*, 710–712.

[94] Carreon, M. A.; Guliants, V. V. Ordered Porous Solids. *Section II: Bi- and Three-dimensional Organised Porous Constructs* **2009**, 413–439.

[95] Kim, T.-W.; Kleitz, F.; Paul, B.; Ryoo, R. MCM-48-like Large Mesoporous Silicas with Tailored Pore Structure: Facile Synthesis Domain in a Ternary Triblock CopolymerButanolWater System. *Journal of the American Chemical Society* **2005**, *127*, 7601–7610.

[96] Meng, Y.; Gu, D.; Zhang, F.; Shi, Y.; Cheng, L.; Feng, D.; Wu, Z.; Chen, Z.; Wan, Y.; Stein, A.; Zhao, D. A Family of Highly Ordered Mesoporous Polymer Resin and Carbon Structures from OrganicOrganic Self-Assembly. *Chemistry of Materials* **2006**, *18*, 4447–4464.

[97] Yue,; Zhou, Synthesis of Porous Single Crystals of Metal Oxides via a SolidLiquid Route. *Chemistry of Materials* **2007**, *19*, 2359–2363.

[98] Gu, D.; Schüth, F. Synthesis of non-siliceous mesoporous oxides. *Chemical Society Reviews* **2013**, *43*, 313–344.

[99] Lowell, S.; Shields, J. E.; Thomas, M. A.; Thommes, M. Characterization of Porous Solids and Powders: Surface Area, Pore Size and Density. **2004**,

[100] Sing, K. S. W. Reporting physisorption data for gas/solid systems with special reference to the determination of surface area and porosity (Recommendations 1984). *Pure and Applied Chemistry* **1985**, *57*, 603–619.

[101] Barrett, E. P.; Joyner, L. G.; Halenda, P. P. The Determination of Pore Volume and Area Distributions in Porous Substances. I. Computations from Nitrogen Isotherms. *Journal of the American Chemical Society* **1951**, *73*, 373–380.

[102] Pecharsky, V. K.; Zavalij, P. Y. Fundamentals of Powder Diffraction and Structural Characterization of Materials. **2009**,

[103] Goodhew, P. J.; Humphreys, J. *Electron Microscopy and Analysis*; CRC Press: Boca Raton, 2017; Vol. Third edition; Accession Number: 153992; OCLC: 1035158181; Language: English.

[104] Robinson, J.; Frame, E.; Frame, G. *Undergraduate Instrumental Analysis, Sixth Edition*; Taylor & Francis.

[105] Harris, D. C.; Bertolucci, M. D. *Symmetry and spectroscopy: an introduction to vibrational and electronic spectroscopy*; Courier Corporation.

[106] Hadjivanov, K. I.; Vayssilov, G. N. Characterization of Oxide Surfaces and Zeolites by Carbon Monoxide as an IR Probe Molecule. *ChemInform* **2003**, *34*.

[107] Maynes, A. J.; Driscoll, D. M.; DeSario, P. A.; Pietron, J. J.; Pennington, A. M.; Rolison, D. R.; Morris, J. R. Electronic Metal–Support Interactions in the Activation of CO Oxidation over a Cu/TiO2 Aerogel Catalyst. *The Journal of Physical Chemistry C* **2020**, *124*, 21491–21501.

[108] Wang, Y.; Wöll, C. IR spectroscopic investigations of chemical and photochemical reactions on metal oxides: bridging the materials gap. *Chemical Society Reviews* **2017**, *46*, 1875–1932.

[109] Le, N. Q.; Bazargan, G.; Schweigert, I. V.; Gunlycke, D. Vibrational Signatures of Sarin Adsorption on Anatase Surfaces. *Surface Science* **2021**, *705*, 121765.

[110] DeSario, P. A.; Gordon, W. O.; Balboa, A.; Pennington, A. M.; Pitman, C. L.; McEntee, M.; Pietron, J. J. Photoenhanced Degradation of Sarin at Cu/TiO 2 Composite Aerogels: Roles of Bandgap Excitation and Surface Plasmon Excitation. *ACS Applied Materials & Interfaces* **2021**,

[111] Petit, T.; Puskar, L. FTIR spectroscopy of nanodiamonds: Methods and interpretation. *Diamond and Related Materials* **2018**, *89*, 52–66.

[112] Stuart, B. H. Infrared Spectroscopy: Fundamentals and Applications. *Analytical Techniques in the Sciences* **2018**,

[113] Mitchell, M. B. In *Structure Properties Relations in Polymers*; Urban, M. W., Craver, C. D., Eds.; 1993; Vol. 236.

[114] Armaroli, T.; Bécue, T.; Gautier, S. Diffuse Reflection Infrared Spectroscopy (Drifts): Application to the in Situ Analysis of Catalysts. *Oil & Gas Science and Technology* **2004**, *59*, 215–237.

[115] Morris, J. R. Development of Instrumental Methods for Particulate and Aerosol Surface Science. *Defense Technical Information Center* **2018**,

[116] Jacoby, M. Air Filters For the Face. *C & EN Chicago* **2014**, 34–38.

[117] Stone, R. Chemical martyrs. *Science* **2018**, *359*, 20–25.

[118] Wagner, G. W.; Koper, O. B.; Lucas, E.; Decker, S.; Klabunde, K. J. Reactions of VX, GD, and HD with Nanosize CaO: Autocatalytic Dehydrohalogenation of HD. *The Journal of Physical Chemistry B* **2000**, *104*, 5118–5123.

[119] Štengl, V.; Bakardjieva, S.; Maříková, M.; Šubrt, J.; Opluštil, F.; Olšanská, M. Aerogel nanoscale magnesium oxides as a destructive sorbent for toxic chemical agents. *Open Chemistry* **2004**, *2*, 16–33.

[120] Zhou, J.; Ma, S.; Kang, Y. C.; Chen, D. A. Dimethyl Methylphosphonate Decomposition on Titania-Supported Ni Clusters and Films: A Comparison of Chemical Activity on Different Ni Surfaces. *The Journal of Physical Chemistry B* **2004**, *108*, 11633–11644.

[121] Mitchell, M. B.; Sheinker, V. N.; Cox, W. W.; Gatimu, E. N.; Tesfamichael, A. B. The Room Temperature Decomposition Mechanism of Dimethyl Methylphosphonate (DMMP) on Alumina-Supported Cerium Oxide Participation of Nano-Sized Cerium Oxide Domains. *The Journal of Physical Chemistry B* **2004**, *108*, 1634–1645.

[122] Ren, Y.; Ma, Z.; Bruce, P. G. Ordered mesoporous metal oxides : synthesis and applications. *Chemical Society Reviews* **2012**, *41*, 4909–4927.

[123] Janos, P.; Kuran, P.; Kormunda, M.; Stengl, V.; Grygar, T. M.; Dosek, M.; Stastny, M.; Ederer, J.; Pilarova, V.; Vrtoch, L. Cerium dioxide as a new reactive sorbent for fast degradation of parathion methyl and some other organophosphates. *Journal of Rare Earths* **2014**, *32*, 360–370.

[124] Hassan, M. H.; Andreescu, D.; Andreescu, S. Cerium Oxide Nanoparticles Stabilized within Metal–Organic Frameworks for the Degradation of Nerve Agents. *ACS Applied Nano Materials* **2020**, *3*, 3288–3294.

[125] Sellik, A.; Pollet, T.; Ouvry, L.; Briançon, S.; Fessi, H.; Hartmann, D.; Renaud, F. Degradation of paraoxon (VX chemical agent simulant) and bacteria by magnesium oxide depends on the crystalline structure of magnesium oxide. *Chemico-Biological Interactions* **2017**, *267*, 67–73.

[126] Liu, S.; Wei, X.; Lin, S.; Guo, M. Preparation of aerogel Mg(OH)2 nanosheets by a combined sol–gel-hydrothermal process and its calcined MgO towards enhanced degradation of paraoxon pollutants. *Journal of Sol-Gel Science and Technology* **2021**, *99*, 122–131.

[127] Zeng, Y.; Haw, K.; Wang, Y.; Zhang, S.; Wang, Z.; Zhong, Q.; Kawi, S. Recent Progress of CeO2TiO2 Based Catalysts for Selective Catalytic Reduction of NOx by NH3. *ChemCatChem* **2021**, *13*, 491–505.

[128] Mosrati, J.; Abdel-Mageed, A. M.; Vuong, T. H.; Grauke, R.; Bartling, S.; Rockstroh, N.; Atia, H.; Armbruster, U.; Wohlrab, S.; Rabeah, J.; Bruckner, A. Tiny Species with Big Impact: High Activity of Cu Single Atoms on CeO2–TiO2 Deciphered by Operando Spectroscopy. *ACS Catalysis* **2021**, *11*, 10933–10949.

[129] Li, W.; Wu, Z.; Wang, J.; Elzatahry, A. A.; Zhao, D. A Perspective on Mesoporous TiO2 Materials. *Chemistry of Materials* **2014**, *26*, 287–298.

[130] Robben, L.; Ismail, A. A.; Lohmeier, S. J.; Feldhoff, A.; Bahnemann, D. W.; Buhl, J.-C. Facile Synthesis of Highly Ordered Mesoporous and Well Crystalline TiO2: Impact of Different Gas Atmosphere and Calcination Temperatures on Structural Properties. *Chemistry of Materials* **2012**, *24*, 1268–1275.

[131] Ji, P.; Zhang, J.; Chen, F.; Anpo, M. Ordered Mesoporous CeO2 Synthesized by Nanocasting from Cubic Ia3d Mesoporous MCM-48 Silica: Formation, Characterization and Photocatalytic Activity. *The Journal of Physical Chemistry C* **2008**, *112*, 17809–17813.

[132] Laha, S. C.; Ryoo, R. Synthesis of thermally stable mesoporous cerium oxide with nanocrystalline frameworks using mesoporous silica templates. *Chemical Communications* **2003**, *0*, 2138–2139.

[133] Toby, B.; Dreele, R. V. GSAS-II: the genesis of a modern open-source all purpose crystallography software package. *Journal of Applied Crystallography* **2013**, *46*, 544–549.

[134] Zaki, M. I.; Hasan, M. A.; Al-Sagheer, F. A.; Pasupulety, L. In situ FTIR spectra of pyridine adsorbed on SiO2–Al2O3, TiO2, ZrO2 and CeO2: general considerations for the identification of acid sites on surfaces of finely divided metal oxides. *Colloids and Surfaces A: Physicochemical and Engineering Aspects* **2001**, *190*, 261–274.

[135] Almerindo, G. I.; Bueno, P.; Nicolazi, L. M.; Wanderlind, E. H.; Sangaletti, P.; Landi, S. M.; Sena, L. A.; Archanjo, B. S.; Achete, C. A.; Fiedler, H. D.; Nome, F. Propanolysis of Methyl Paraoxon in the Presence of Aluminum-Titanate-Supported Erbium Oxide. *The Journal of Physical Chemistry C* **2016**, *120*, 22323–22329.

[136] Zimmermann, L. M.; Almerindo, G. I.; Mora, J. R.; Bechtold, I. H.; Fiedler, H. D.; Nome, F. Degradation of Methyl Paraoxon in the Presence of Mg 2+ -Al 3+ Mixed Oxides. *The Journal of Physical Chemistry C* **2013**, *117*, 26097–26105.

[137] Tamura, M.; Shimizu, K.-i.; Satsuma, A. Comprehensive IR study on acid/base properties of metal oxides. *Applied Catalysis A: General* **2012**, *433*, 135–145.

[138] Wu, Y.; Gao, F.; Wang, H.; Kovarik, L.; Sudduth, B.; Wang, Y. Probing Acid–Base Properties of Anatase TiO2 Nanoparticles with Dominant {001} and {101} Facets Using Methanol Chemisorption and Surface Reactions. *The Journal of Physical Chemistry C* **2021**, *125*, 3988–4000.

[139] Bezrodna, T.; Puchkovska, G.; Shimanovska, V.; Chashechnikova, I.; Khalyavka, T.; Baran, J. Pyridine-TiO2 surface interaction as a probe for surface active centers analysis. *Applied Surface Science* **2003**, *214*, 222–231.

[140] Wu, Z.; Mann, A. K. P.; Li, M.; Overbury, S. H. Spectroscopic Investigation of Surface-Dependent Acid–Base Property of Ceria Nanoshapes. *The Journal of Physical Chemistry C* **2015**, *119*, 7340–7350.

[141] Zimmermann, L. M.; Almerindo, G. I.; Medeiros, M.; Affeldt, R. F.; Wanderlind, E. H.; Gerola, A. P.; Nome, R. A.; Tumelero, M. A.; Faccio, R.; Pasa, A. A.; Fiedler, H. D.; Nome, F. Toward Heterogeneously Catalyzed Detoxification of Phosphotriesters: Insights from Kinetics and Theoretical Calculations. *The Journal of Physical Chemistry C* **2018**, *122*, 25530–25538.

[142] Hemmer, J. V.; Wanderlind, E. H.; Bazani, H. A. G.; Campos, C. E. M.; Wagner, T. M.; Emmerich, A. K.; Adão, J. R. U.; Almerindo, G. I. Simple and highly active strontium-based catalyst for detoxification of an organophosphorus chemical warfare agent simulant. *Brazilian Journal of Chemical Engineering* **2020**, *37*, 533–541.

[143] Almerindo, G. I.; Buratto, S. C.; Wanderlind, E. H.; Nicolazi, L. M.; Sangaletti, P.; Medeiros, M.; Schneider, F. S. S.; Caramori, G. F.; Parreira, R. L. T.; Micke, G. A.; Fiedler, H. D.; Nome, F. Kinetics and adsorption calculations: insights into the MgO-catalyzed detoxification of simulants of organophosphorus biocides. *Journal of Materials Chemistry A* **2020**, *8*, 19011–19021.

[144] Socrates, G. *Infrared and Raman Characteristic Group Frequencies: Tables and Charts*; John Wiley & Sons Ltd, 2004.

[145] Wong, K.-Y.; Gao, J. The Reaction Mechanism of Paraoxon Hydrolysis by Phosphotriesterase from Combined QM/MM Simulations †. *Biochemistry* **2007**, *46*, 13352–13369.

[146] Amarasingam, A. A History of Sarin as a Weapon. `https://www.theatlantic.com/international/archive/2017/04/sarin-syria-assad-chemical-nazi/522039/`.

[147] Allen, S. E.; Walvoord, R. R.; Padilla-Salinas, R.; Kozlowski, M. C. Aerobic Copper-Catalyzed Organic Reactions. *Chemical Reviews* **2013**, *113*, 6234–6458.

[148] Zedan, A. F.; Mohamed, A. T.; El-Shall, M. S.; AlQaradawi, S. Y.; AlJaber, A. S. Tailoring the reducibility and catalytic activity of CuO nanoparticles for low temperature CO oxidation. *RSC Advances* **2018**, *8*, 19499–19511.

[149] Pffath, R. J. Infrared Spectroscopic Observations on the Fate of Organophosphorus Compounds Exposed to Atmospheric Moisture. Part I. G-Agents and Related Compounds. *Defense Technical Information Center* **2003**,

[150] Hirakawa, T.; Sato, K.; Komano, A.; Kishi, S.; Nishimoto, C. K.; Mera, N.; Kugishima, M.; Sano, T.; Ichinose, H.; Negishi, N.; Seto, Y.; Takeuchi, K. Experimental Study on Adsorption and Photocatalytic Decomposition of Isopropyl Methylphosphonofluoridate at Surface of TiO2 Photocatalyst. *The Journal of Physical Chemistry C* **2010**, *114*, 2305–2314.

[151] Plonka, A. M.; Wang, Q.; Gordon, W. O.; Balboa, A.; Troya, D.; Guo, W.; Sharp, C. H.; Senanayake, S. D.; Morris, J. R.; Hill, C. L.; Frenkel, A. I. In Situ Probes of Capture and Decomposition of Chemical Warfare Agent Simulants by Zr-Based Metal Organic Frameworks. *Journal of the American Chemical Society* **2017**, *139*, 599–602.

[152] Balow, R. B.; McEntee, M.; Schweigert, I. V.; Jeon, S.; Peterson, G. W.; Pehrsson, P. Battling Chemical Weapons with Zirconium Hydroxide Nanoparticle Sorbent: Impact of Environmental Contaminants on Sarin Sequestration and Decomposition. *Langmuir* **2021**, *37*, 6923–6934.

[153] Harvey, J. A.; McEntee, M. L.; Garibay, S. J.; Durke, E. M.; DeCoste, J. B.; Greathouse, J. A.; Gallis, D. F. S. Spectroscopically Resolved Binding Sites for the Adsorption of Sarin Gas in a Metal–Organic Framework: Insights beyond Lewis Acidity. *The Journal of Physical Chemistry Letters* **2019**, *10*, 5142–5147.

[154] Plonka, A. M.; Grissom, T. G.; Musaev, D. G.; Balboa, A.; Gordon, W. O.; Collins-Wildman, D. L.; Ghose, S. K.; Tian, Y.; Ebrahim, A. M.; Mitchell, M. B.; Hill, C. L.; Morris, J. R.; Frenkel, A. I. Effect of Carbon Dioxide on the Degradation of Chemical Warfare Agent Simulant in the Presence of Zr Metal Organic Framework MOF-808. *Chemistry of Materials* **2019**, *31*, 9904–9914.

[155] Sadeghi, M.; Yekta, S.; Mirzaei, D. A novel CuO NPs/AgZSM-5 zeolite composite adsorbent: Synthesis, identification and its application for the removal of sulfur mustard agent simulant. *Journal of Alloys and Compounds* **2018**, *748*, 995–1005.

[156] Mitchell, M. B.; Sheinker, V. N.; Cox, W. W. Room Temperature Reaction of Ozone and Dimethyl Methylphosphonate (DMMP) on Alumina-Supported Iron Oxide. *The Journal of Physical Chemistry C* **2007**, *111*, 9417–9426.

[157] Tesfai, T. M.; Sheinker, V. N.; Mitchell, M. B. Decomposition of Dimethyl Methylphosphonate (DMMP) on Alumina-Supported Iron Oxide. *The Journal of Physical Chemistry B* **1998**, *102*, 7299–7302.

[158] Mishra, S.; Fontanesi, C. Combined effect of organic-inorganic heterostructure to enhance electrochemical capacitance. *Materials Chemistry and Physics* **2019**, *238*, 121943.

[159] Hermawan, A.; Hanindriyo, A. T.; Hongo, K.; Maezono, R.; Yin, S. Impact of Surface Faceting on Gas Sensing Selectivity of NiO: Revealing the Adsorption Sites of Organic Vapors on the $\{111\}$ Facet. *The Journal of Physical Chemistry C* **2022**, *126*, 8037–8046.

[160] Drozdowska, K.; Welearegay, T.; Österlund, L.; Smulko, J. Combined chemoresistive and in situ FTIR spectroscopy study of nanoporous NiO films for light-activated nitrogen dioxide and acetone gas sensing. *Sensors and Actuators B: Chemical* **2022**, *353*, 131125.

[161] Yu, T.; Li, Z.; Zheng, H.; Chen, L.; Song, W.; Zhao, Z.; Li, J.; Liu, J. The nature of Ni-O pairs for ethane activation on NiO(100) and NiO(110) surfaces. *Molecular Catalysis* **2019**, *474*, 110417.

[162] Delgado, D.; Solsona, B.; Ykrelef, A.; Rodríguez-Gómez, A.; Caballero, A.; Rodríguez-Aguado, E.; Rodríguez-Castellón, E.; Nieto, J. M. L. Redox and Catalytic Properties of Promoted NiO Catalysts for the Oxidative Dehydrogenation of Ethane. *The Journal of Physical Chemistry C* **2017**, *121*, 25132–25142.

[163] Jeong, M.-G.; Park, E. J.; Jeong, B.; Kim, D. H.; Kim, Y. D. Toluene combustion over NiO nanoparticles on mesoporous SiO2 prepared by atomic layer deposition. *Chemical Engineering Journal* **2014**, *237*, 62–69.

[164] Ren, Y.; Ma, Z.; Qian, L.; Dai, S.; He, H.; Bruce, P. G. Ordered Crystalline Mesoporous Oxides as Catalysts for CO Oxidation. *Catalysis Letters* **2009**, *131*, 146–154.

[165] Kiselev, A.; Mattson, A.; Andersson, M.; Palmqvist, A.; Österlund, L. Adsorption and photocatalytic degradation of diisopropyl fluorophosphate and dimethyl methylphosphonate over dry and wet rutile TiO2. *Journal of Photochemistry and Photobiology A: Chemistry* **2006**, *184*, 125–134.

[166] Kiselev, A.; Andersson, M.; Mattson, A.; Shchukarev, A.; Sjöberg, S.; Palmqvist, A.; Österlund, L. Solar light decomposition of DFP on the surface of anatase and rutile TiO2 prepared by hydrothermal treatment of microemulsions. *Surface Science* **2005**, *584*, 98–105.

[167] Deng, X.; Chen, K.; Tüysüz, H. Protocol for the Nanocasting Method: Preparation of Ordered Mesoporous Metal Oxides. *Chemistry of Materials* **2016**, *29*, 40–52.

[168] Xu, X.; Li, L.; Huang, J.; Jin, H.; Fang, X.; Liu, W.; Zhang, N.; Wang, H.; Wang, X. Engineering Ni3+ Cations in NiO Lattice at the Atomic Level by Li+ Doping: The Roles of Ni3+ and Oxygen Species for CO Oxidation. *ACS Catalysis* **2018**, *8*, 8033–8045.

[169] Heracleous, E.; Lemonidou, A. Ni–Nb–O mixed oxides as highly active and selective catalysts for ethene production via ethane oxidative dehydrogenation. Part I: Characterization and catalytic performance. *Journal of Catalysis* **2006**, *237*, 162–174.

[170] Moussa, S.; Concepcion, P.; Arribas, M. A.; Martinez, A. Nature of Active Nickel Sites and Initiation Mechanism for Ethylene Oligomerization on Heterogeneous Ni-beta Catalysts. *ACS Catalysis* **2018**, *8*, 3903–3912.

[171] Hegde, R. I.; Greenlief, C. M.; White, J. M. Surface chemistry of dimethyl methylphosphonate on rhodium(100). *The Journal of Physical Chemistry* **1985**, *89*, 2886–2891.

[172] Mott, A. J.; Rez, P. Calculated infrared spectra of nerve agents and simulants. *Spectrochimica Acta Part A: Molecular and Biomolecular Spectroscopy* **2012**, *91*, 256–260.

[173] Heiss, D. R.; Zehnder, D. W.; Jett, D. A.; Platoff, G. E.; Yeung, D. T.; Brewer, B. N. Synthesis and Storage Stability of Diisopropylfluorophosphate. *Journal of Chemistry* **2016**, *2016*, 3190891.

[174] Kolodziejczyk, W.; Majumdar, D.; Roszak, S.; Leszczynski, J. Probing the role of PO stretching mode enhancement in nerve-agent sensors: Simulation of the adsorption of diisopropylfluorophosphate on the model MgO and CaO surfaces. *Chemical Physics Letters* **2007**, *450*, 138–143.

[175] Kondo, J. N.; Yuzawa, T.; Kubota, J.; Domen, K.; Hirose, C. IRAS study of hydroxyl species on NiO/Ni(110): formation and isotope exchange reaction. *Surface Science* **1995**, *343*, 71–79.

[176] Matsumoto, T.; Bandara, A.; Kubota, J.; Hirose, C.; Domen, K. Adsorption and Reaction of Formic Acid on a (2 2) NiO(111)/Ni(111) Surface. 3. IRAS Studies on the Characterization of Reaction Sites Using CO and the Behavior of Surface Hydroxyl Species. *The Journal of Physical Chemistry B* **1998**, *102*, 2979–2984.

[177] Butrow, A. B.; Buchanan, J. H.; Tevault, D. E. Vapor Pressure of Organophosphorus Nerve Agent Simulant Compounds. *Journal of Chemical & Engineering Data* **2009**, *54*, 1876–1883.

[178] Medine, G. M.; Zaikovskii, V.; Klabunde, K. J. Synthesis and adsorption properties of intimately intermingled mixed metal oxide nanoparticles. *Journal of Materials Chemistry* **2003**, *14*, 757–763, UV/Vis without buffer.

Chapter 7: Appendix: Supplemental Figures

7.1 Chapter 3

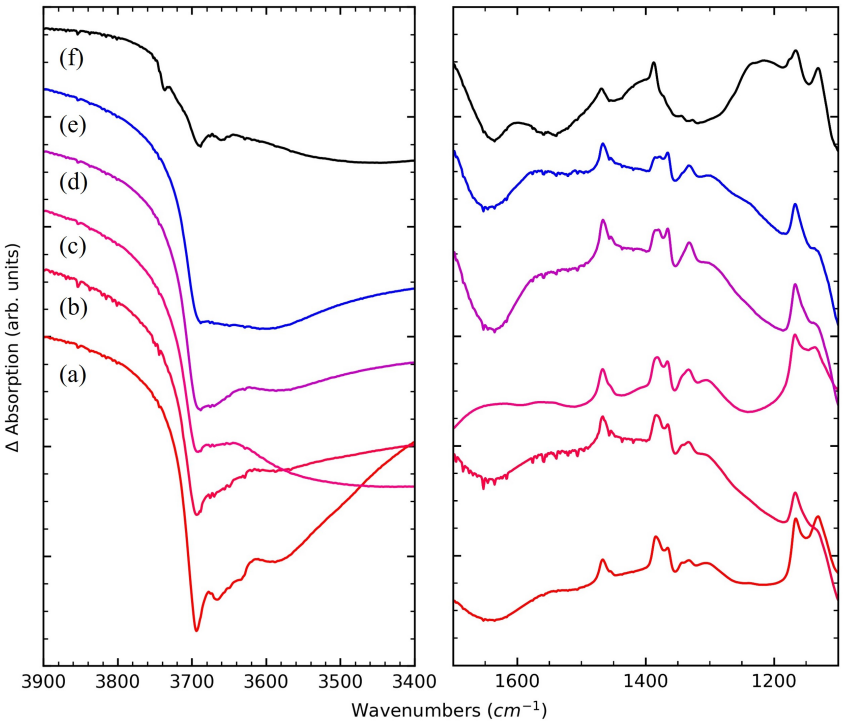


Figure 7.A1: DRIFTS spectrum after being stirred with 2-propanol, filtered, and dried in a vacuum. a) TiO_2, b) $Ce_{0.005}Ti_{0.995}O_2$, c) $Ce_{0.05}Ti_{0.95}O_2$, d) $Ce_{0.10}Ti_{0.90}O_2$, e) $Ce_{0.15}Ti_{0.85}O_2$ and f) CeO_2.

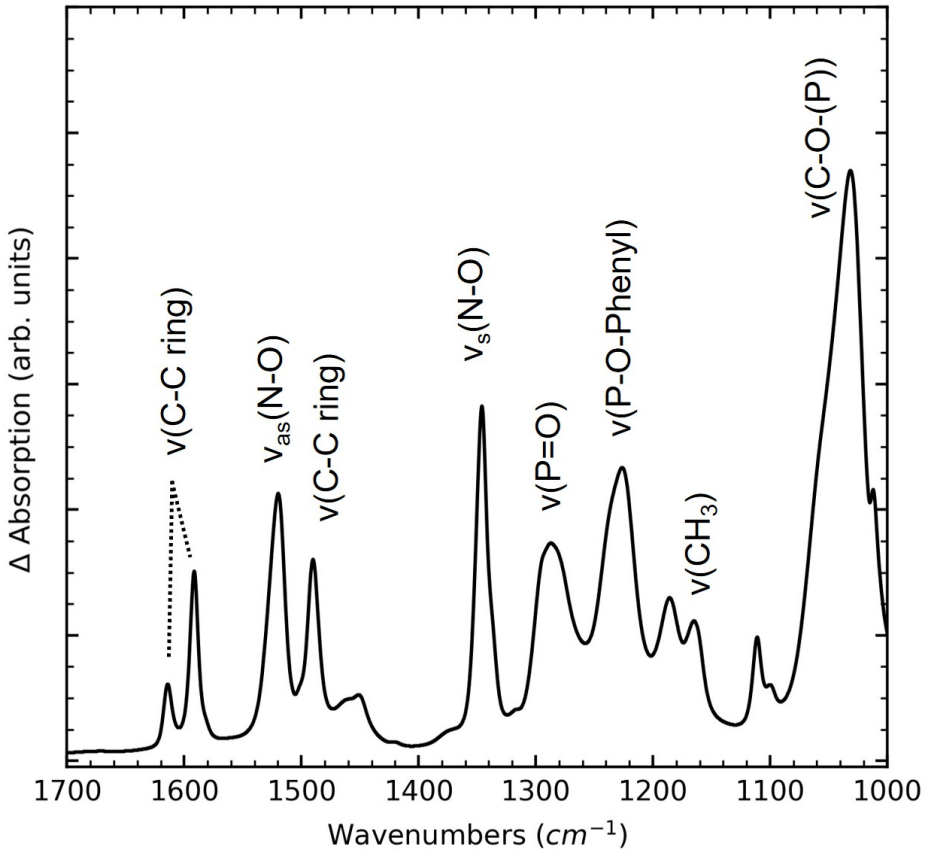


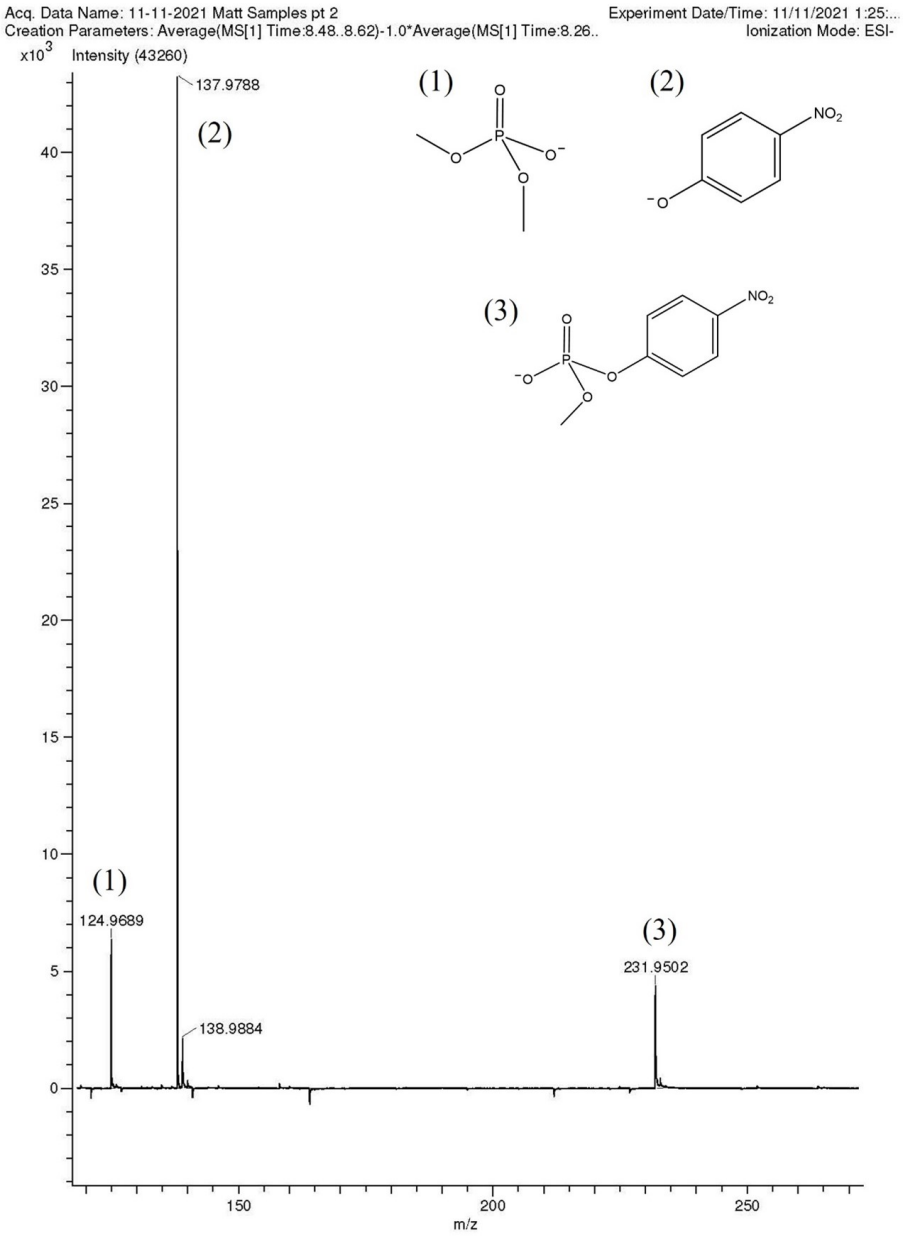
Figure 7.A2: ATR FTIR spectrum of paraoxon with peaks assigned from the literature [178]

Table 7.A1: EDS atomic percentages metal concentrations for $Ce_xTi_{1-x}O_2$.

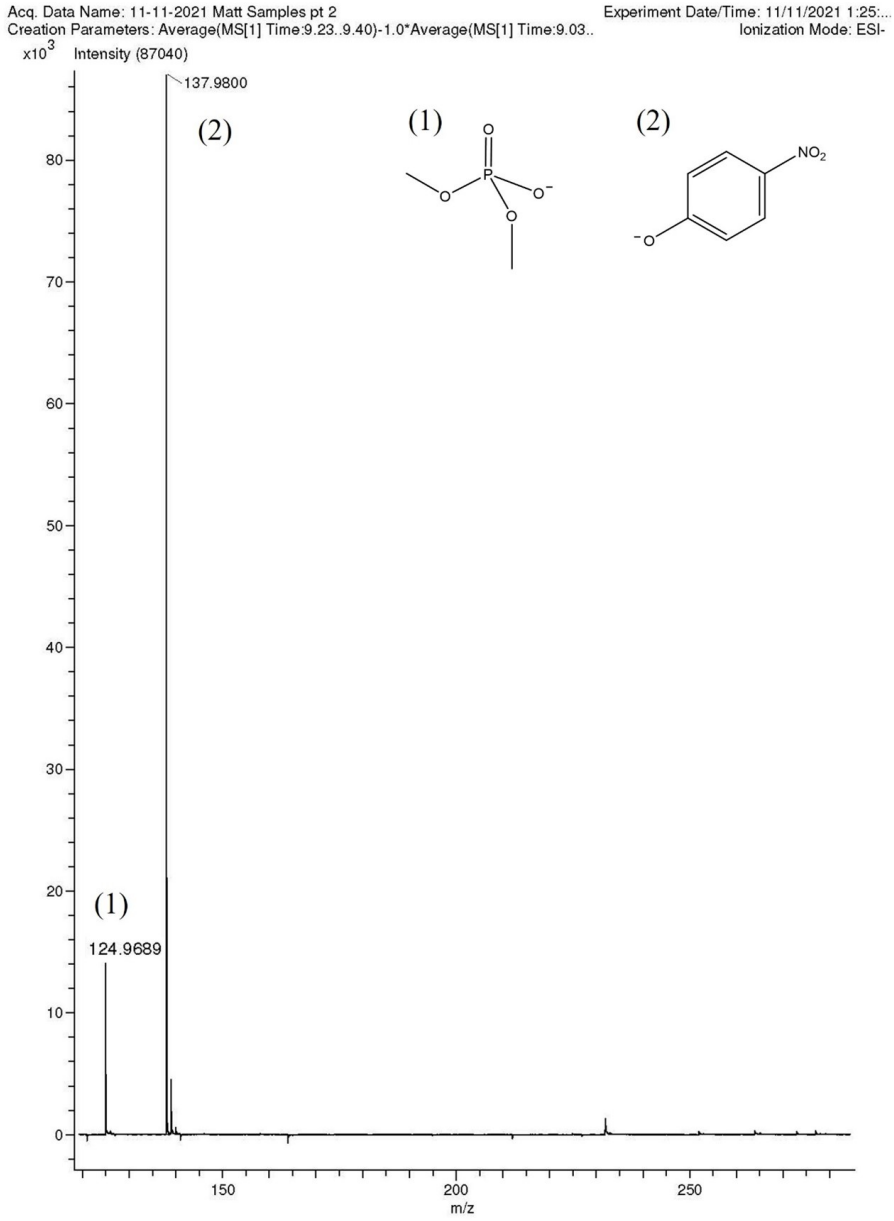
Material	**Ti**	**Ce**
$Ce_{0.005}Ti_{0.995}O_2$	99.68%	0.31%
$Ce_{0.05}Ti_{0.95}O_2$	96.24%	3.76%
$Ce_{0.10}Ti_{0.90}O_2$	91.71%	8.28%
$Ce_{0.15}Ti_{0.85}O_2$	83.45%	16.55%

ESI-MS

Since the mass spectrometry was used to qualitatively determine the product, only one data is shown since all look similar. The peak at m/z 231.9 at 5 minutes is a contaminant that is seen within the pure paraoxon.



(a) ESI-MS for $Ce_{0.15}Ti_{0.85}O_2$ after 5 minutes.



(b) ESI-MS for $Ce_{0.15}Ti_{0.85}O_2$ after 4 hours.

Figure 7.A3: ESI-MS for $Ce_{0.15}Ti_{0.85}O_2$ with paraoxon at a) 5 min and b) 4 h. Paraoxon's decomposition is further confirmed through the peak at (m/z) 138.9800 of 4-nitrophenol. The non-stoichiometric ratio between peaks 1 and 2 suggests the degraded paraoxon remains on the surface.

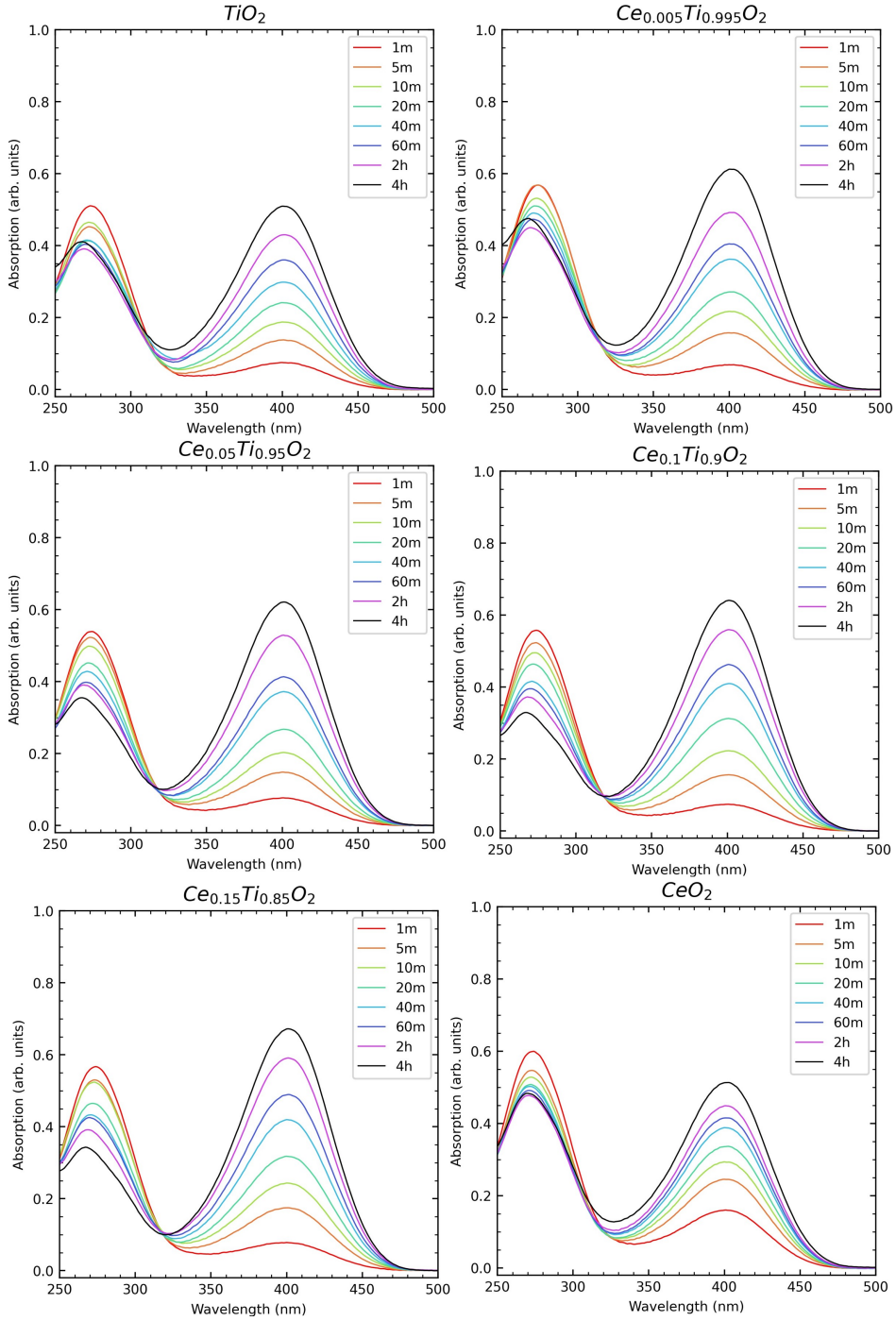


Figure 7.A4: Time dependant UV/Vis absorption spectra of TiO_2, $Ce_xTi_{1-x}O_2$ and CeO_2 as paraoxon decomposes.

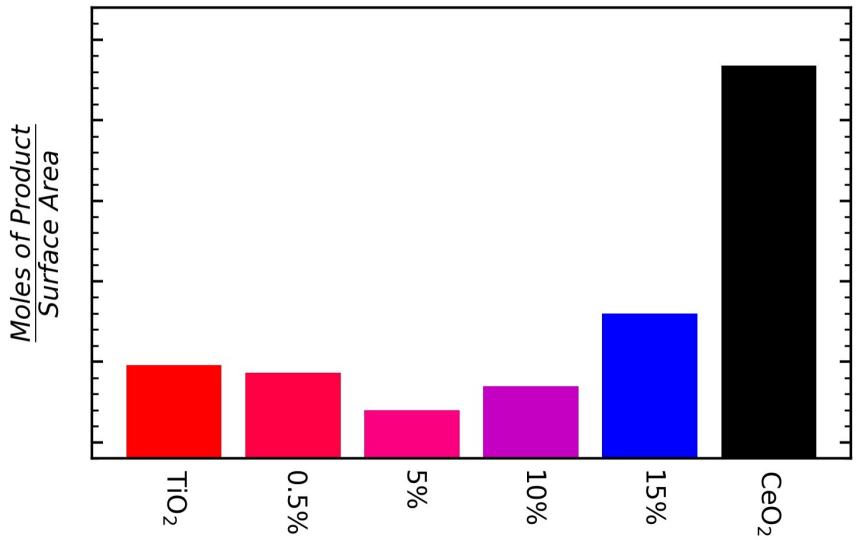


Figure 7.A5: Normalized paraoxon decomposition on TiO_2, $Ce_xTi_{1-x}O_2$, CeO_2 after 4 hours.

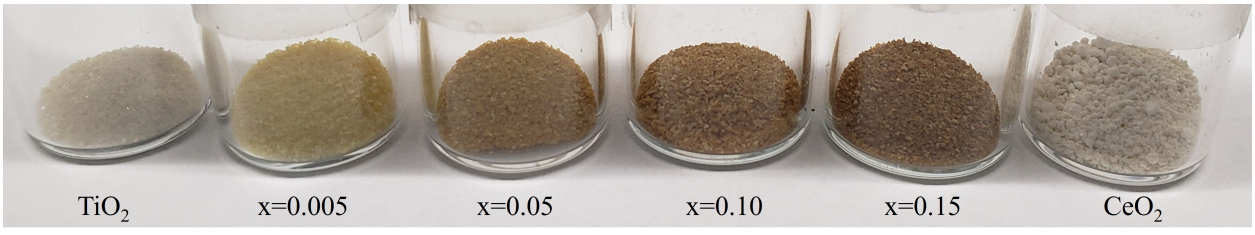


Figure 7.A6: From left to right TiO_2, $Ce_xTi_{1-x}O_2$ and CeO_2 samples. As more cerium is added the material becomes browner.

Table 7.A2: *Ex-situ* pyridine absorption peak frequencies with assigned sites.

Wavenumber (cm^{-1})	TiO_2	Wavenumber (cm^{-1})	CeO_2	Wavenumber (cm^{-1})	$Ce_xTi_{1-x}O_2$
1445	LPy	1443	LPy	1445	LPy
1491	Lpy +Bpy	1485	Lpy + Bpy	1485	Lpy +Bpy
1576	LPy	1598	LPy	1576	LPy
1594	HPy			1580	HPy
1605	LPy			1594	HPy
1640	BPy			1605	LPy

Table 7.A3: Peaks and assigned vibrations from *ex-situ* DRIFTS of each MMO with paraoxon and TiO_2 with 2-propanol in cm^{-1}.

Mode	TiO_2	x = 0.5%	x = 5%	x = 10%	x = 15%	CeO_2	2-Propanol on TiO_2
v(O-P-O) ρ(O-CH_3) v(C-CH_3)	1114, 1165, 1191	1114, 1167, 1191	1167, 1191	1105, 1167, 1191	1102, 1167, 1191	1195	1131, 1165
δ(C-CH_3)	1452, 1466	1452, 1466	1452, 1466	1452, 1465	1452, 1465	1451, 1467	1467
v(O-CH_3)	2857, 2957	2856, 2957	2856, 2957	2856, 2957	2856, 2957	2854, 2956	
v(C-CH_3)						2973	2936, 2971
v(O-H)	3635, 3668, 3695	3694	3693	3686	3685	3663, 3690, 3733	

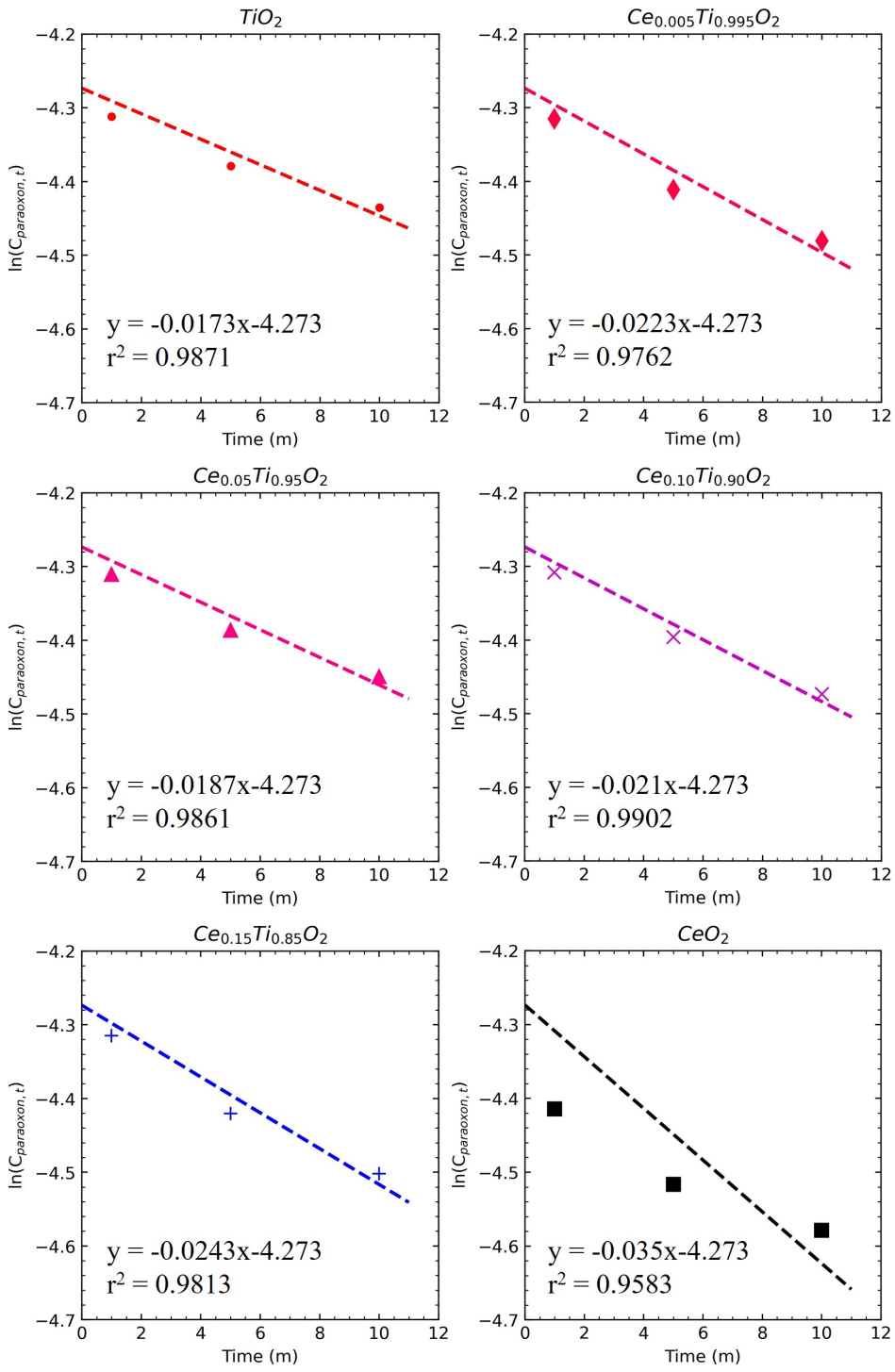


Figure 7.A7: Decomposition of paraoxon on each metal oxide with calculated decomposition.

7.2 Chapter 4

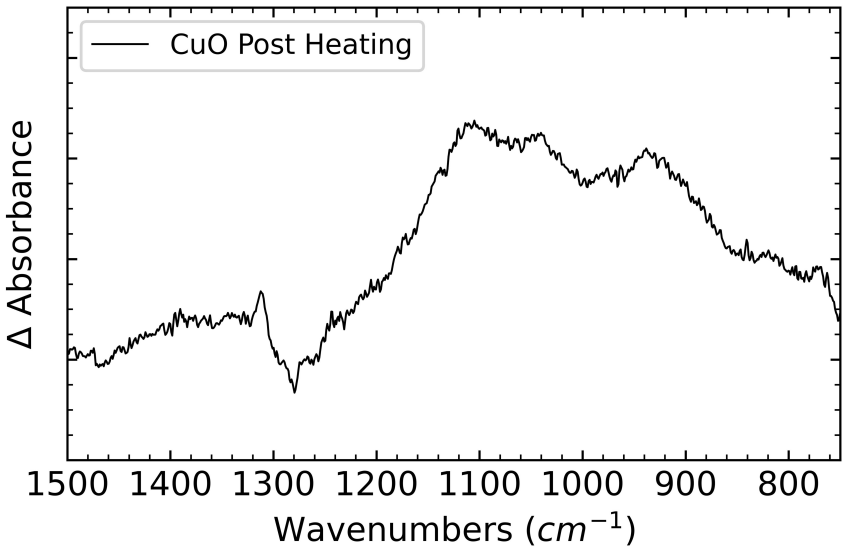


Figure 7.A8: Infrared difference spectrum of CuO NP between clean CuO and CuO post GB exposure and heating. The negative peak at 1280 cm-1 belongs to an unknown contamination that desorbed during the experiment.

7.3 Chapter 5

7.3.1 Materials

Nickel nitrate hexahydrate, copper nitrate trihydrate, P123 and DFP were purchased from Sigma-Aldrich. All chemicals were used with no further purification.

7.3.2 Bulk and Surface Characterization

Scanning electron microscope (SEM) images were taken using a Hitachi SU-70 Field Emission SEM equipped with a Bruker energy dispersive spectroscopy (EDS) detection model: Flash 6T/60 with a silicon drift detection (No Li dopant) and solid angle of 0.189 sr. Transmission electron microscope (TEM) images were taken on a JOEL-2100 LaB6 TEM with an accelerating voltage of 200 kV and a beam current of 104 μA. All samples were dispersed in ethanol and drop cast onto a lacey carbon 200-mesh copper grid.

Nitrogen isotherms were recorded with a Micrometrics ASAP 2020 Porosimeter. Samples were degassed in vacuum at 150 °C for 6 h prior to characterization. The surface area was determined using the Brunauer-Emmett-Teller (BET) method with a relative pressure range (P/P_o) of 0.05-0.30. Pore size and volume was calculated from the adsorption branch using the Barrett, Joyner, and Halenda (BJH) method. Powder x-ray diffraction (XRD) diffraction patterns were collected using a Bruker X-ray diffractometer with a Cu Kα radiation (λ=1.5406 Å) and a LynxEye position-sensitive detector. Rietveld refinements was performed using GSAS II [133]. Small-angle x-ray scattering (SAXS) patterns were collected using a Xenocs Xeuss SAXS/WAXS/GISAXS system.

Thermogravimetric analysis (TGA) measurements were run using a Mettler Tolledo TGA/DSC 2 STAR System. Samples were placed in the TGA and degassed under Argon flow for 18 h to remove anything loosely bound to the surface, then heated to 500 °C at 5 °C/min. Raman spectra were collected on a WITec alpha 300 apryon with a 523nm laser with a power of 0.5 mW.

Ex-situ experiments were conducted by packing approximately 10-15 mg of sample into a porous ceramic cup, pretreated at 250 °C. A background spectrum was recorded prior to placing into a 20mL vial with 1 to 2 drop of liquid (DIMP, HF, Acetone, Formic Acid) and capped. After 3 hours of exposure, the samples were placed in purge gas flow to remove any loosely bound species and a new spectrum was recorded. Pyridine samples were pretreated similarly but placed in a closed jar with an open bottle of pyridine for 1 week.

Table 7.A4: EDS atomic percentages metal concentrations for $Cu_xNi_{1-x}O_2$.

Mesoporous Material	Cu %	Ni %
$Cu_{0.1}Ni_{0.9}O$	10.83 (±0.25)	89.17 (±1.71)
$Cu_{0.2}Ni_{0.8}O$	20.16 (±0.44)	79.84 (±1.52)

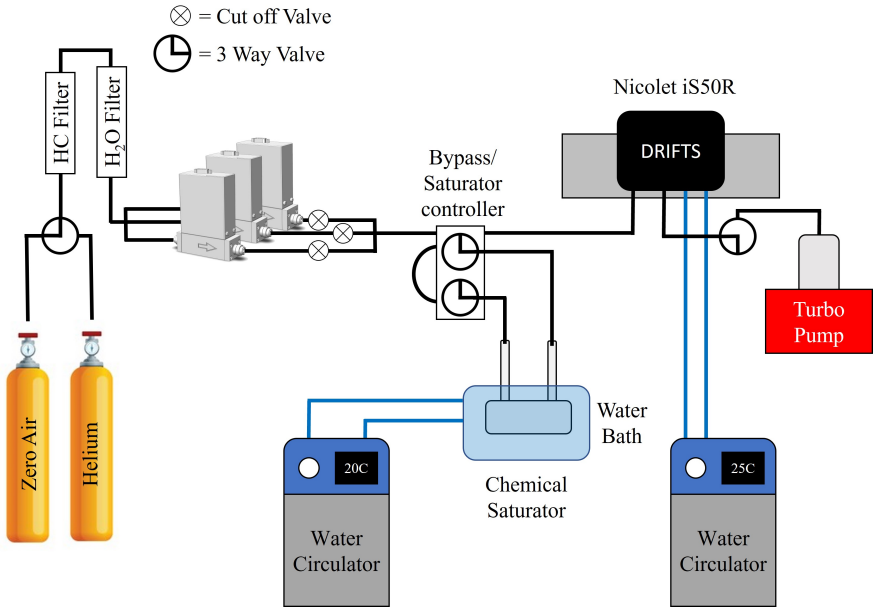


Figure 7.A9: Schematic of DRIFTS reactor.

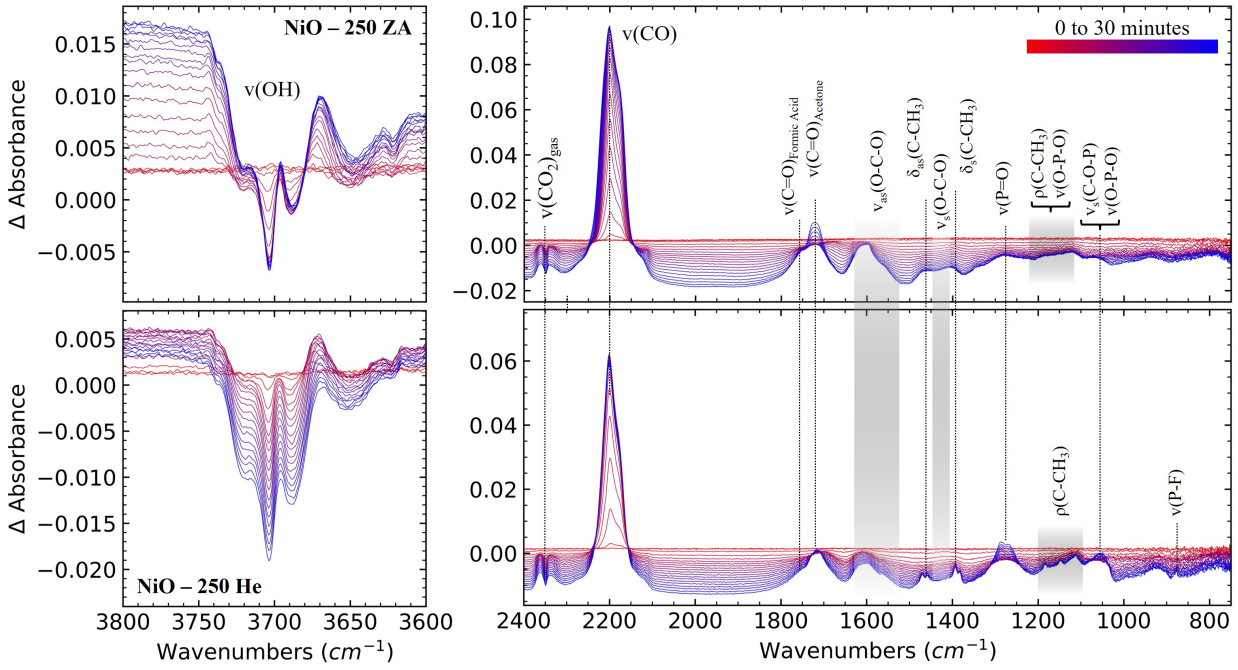


Figure 7.A10: DRIFTS difference spectrum of mesoporous NiO heated to 250 °C (NiO-250) exposed to DFP for 30 minutes in an O_2-rich environment (NiO-250 ZA) (Top) and in an O_2-free environment (NiO-250 He) (bottom) with the assigned modes from literature.

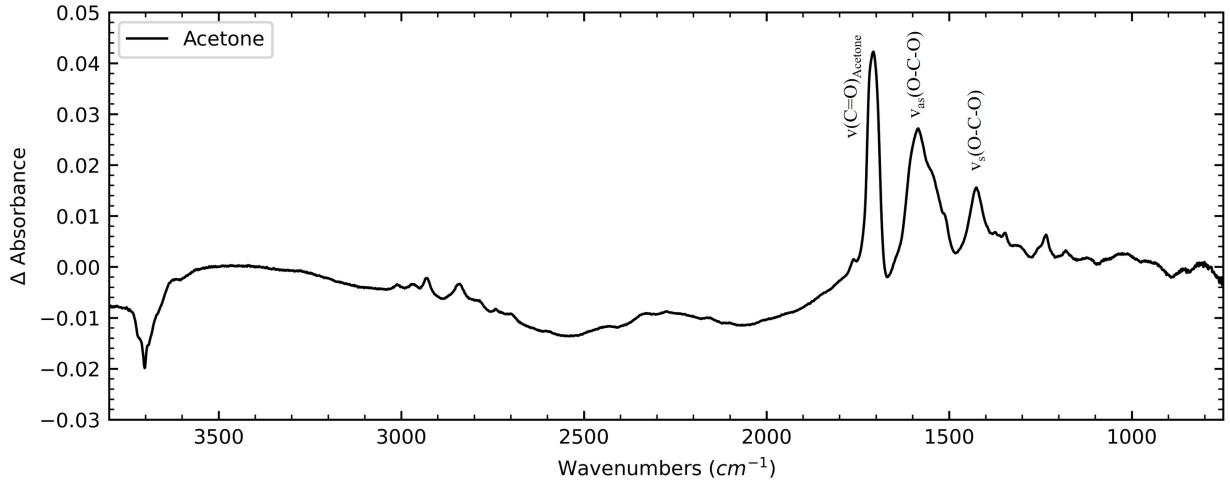


Figure 7.A11: DRIFTS difference spectrum of Acetone adsorbed on NiO-250.

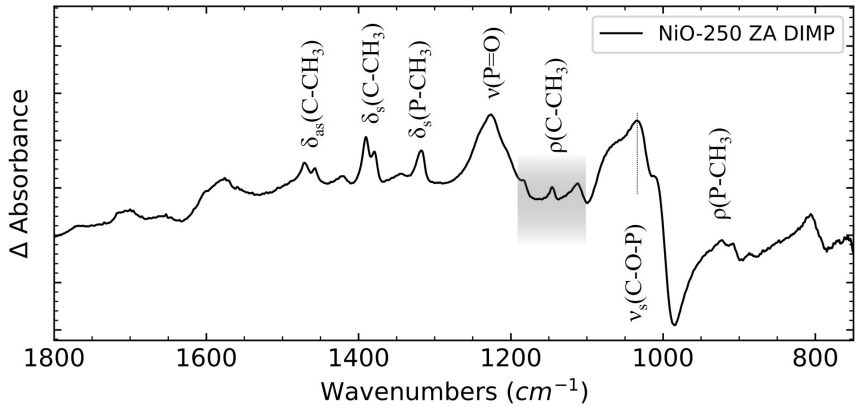


Figure 7.A12: *Ex-situ* exposure of diisopropyl methylphosphonate (DIMP) on NiO-250. DIMP physisorbs to the surface of NiO-250.

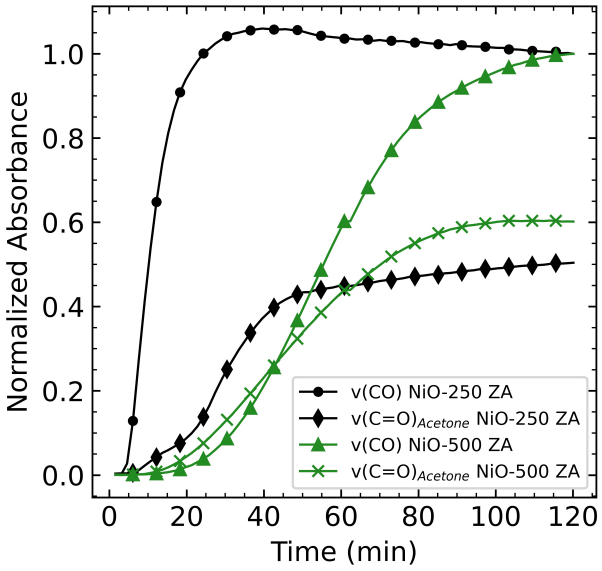


Figure 7.A13: Intensity of the main decomposition peaks of ν(CO) and ν(C=O)$_{Acetone}$ normalized to the final intensity of the respective experiment ν(CO) mode. Black corresponds to NiO-250 ZA data, while green corresponds to NiO-500 ZA data.